The Dissertation Committee for Frank Moonyoung Lee
certifies that this is the approved version of the following dissertation:

Determination of the Energy Flux of Internal Gravity Waves

Committee:

Philip J. Morrison, Supervisor

Harry L. Swinney

Richard D. Hazeltine

C. Wendell Horton

Irene M. Gamba

Determination of the Energy Flux of Internal Gravity Waves

by

Frank Moonyoung Lee

DISSERTATION

Presented to the Faculty of the Graduate School of

The University of Texas at Austin

in Partial Fulfillment

of the Requirements

for the Degree of

DOCTOR OF PHILOSOPHY

THE UNIVERSITY OF TEXAS AT AUSTIN

December 2017

Acknowledgments

We thank Bruce Rodenborn for help with the code and the GUI for the PIV method, and Likun Zhang and Robert Moser for helpful discussions. The computations were done at the Texas Advanced Computing Center. MSP, MRA, and HLS were supported by the Office of Naval Research MURI Grant N000141110701, while PJM and FML were supported by the U.S. Department of Energy, Office of Science, Office of Fusion Energy Sciences, under Award Numbers DE-FG05-80ET-53088 and DE-FG02-04ER-54742.

Determination of the Energy Flux of Internal Gravity Waves

Publication No. _____

Frank Moonyoung Lee, Ph.D.
The University of Texas at Austin, 2017

Supervisor: Philip J. Morrison

Internal gravity waves are traveling disturbances that propagate within a fluid whose density varies with depth, and two prominent examples where these occur are the atmosphere and the ocean. In the latter case, which is the focus of this work, the tidal forcing by the moon creates internal gravity waves (oftentimes referred to simply as "internal waves") that originate from the ocean bottom topography. The energy generated in the internal waves by this mechanism contributes significantly to the energy budget of the ocean. Hence it is important to determine the energy flux in the internal waves. However, it is not possible to obtain the energy flux $\boldsymbol{J} = p\,\boldsymbol{v}$ directly because the pressure and velocity perturbation fields, p and $\boldsymbol{v}$, cannot be simultaneously measured at the present time. The two primary methods for measuring internal waves in the laboratory are particle image velocimetry (PIV), which gives velocity perturbation fields $\boldsymbol{v}(x, z, t)$, and synthetic schlieren, which gives density perturbation fields $\rho(x, z, t)$. We present one method for obtaining the

time-averaged energy flux $\langle \boldsymbol{J} \rangle$ from PIV data by calculating the stream function $\psi(x, z, t)$, whose results agree to within 0.5% when compared with direct numerical simulations of the Navier-Stokes equations. The method was also applied to laboratory data, and again using direct numerical simulations, the agreement was found to be very good. A MATLAB code was developed with a graphical user interface that can be used to compute the energy flux and power from any two-dimensional velocity field data. Another method, using a Green's function approach, was developed to obtain the instantaneous energy flux $\boldsymbol{J}(x, z, t)$ from density perturbation data $\rho(x, z, t)$ such as that from synthetic schlieren. This was done for a uniform, tanh, and linear buoyancy frequency $N(z)$. Additionally, a finite-difference method was developed for the case of arbitrary $N(z)$. The results for $\boldsymbol{J}(x, z, t)$ are found to agree with results from direct numerical simulations, typically to within 6%. These methods can be applied to any density perturbation data using the MATLAB graphical user interface EnergyFlux.

Table of Contents

List of Figures

Chapter 1

Introduction to internal gravity waves

In this first chapter of the dissertation, some basic important topics regarding internal gravity waves will be briefly explained. In section 1.1, the nature of internal gravity waves will be explored using elementary physics concepts. In section 1.2 the basic linear internal gravity wave equations will be derived starting with the Euler equations of fluid mechanics. Section 1.3 will outline some properties of internal gravity waves by first deriving the dispersion relation, assuming traveling wave solutions, and from this the phase and group velocities will be calculated. In section 1.4 the energy flux of internal gravity waves will be derived from the equations of motion and energy conservation. Lastly, in section 1.5 a brief history regarding the determination of the energy flux from internal gravity waves produced in the laboratory will be outlined, with subsection 1.5.1 specifically focusing on the velocity-based approaches, and subsection 1.5.2 focusing on the density-based approaches.

1.1 Local fluid element description

Internal gravity waves, oftentimes referred to simply as "internal waves", are buoyancy-driven traveling disturbances that occur in fluids where the den-

sity varies with height under the influence of gravity. On Earth they primarily occur in the atmosphere and the ocean, the latter of which will be the focus of this work. The primary driving force behind the creation of internal waves in the ocean is the tidal motion due to the moon. This sloshing back and forth of the ocean water interacts with the topography at the ocean bottom and creates internal waves that propagate away from the peaks. These internal waves, with a size-scale of roughly on the order of a km, are known to act as an intermediary between the large-scale tidal motion (roughly 10^3 km) and smaller-scale overturning and mixing (less than 10 m).

We can gain some understanding of their nature by examining a fluid element in a stratified fluid (a fluid whose density $\rho_0(z)$ varies with height). We take the initial vertical position of said fluid element to be z_0 and at this position its density is given by $\rho_0(z_0)$. Its volume will be taken to be δV, which will not change because we assume the fluid to be incompressible. Then if we displace this fluid element upwards by an amount given by δz, it will be surrounded by fluid whose density is slightly less, and will feel a buoyant force in addition to the force of gravity. The net force then is given by

$$F_{net} = \delta V \rho_0(z_0 + \delta z)g - \delta V \rho_0(z_0)g. \tag{1.1}$$

Here, g is the acceleration due to gravity. The first term in (1.1) is the upward buoyant force resulting from the displacement of the lower density fluid with density $\rho_0(z_0 + \delta z)$, and the second term is the force exerted by gravity. Assuming the upward displacement is small, we can linearize by Taylor

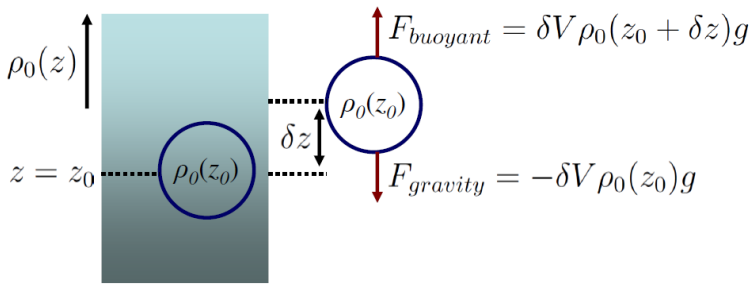

Figure 1.1: The density of the fluid ρ_0 decreases with height z, which is a stable configuration under gravity. A fluid element is then displaced from its equilibrium position z_0 by δz, which results in a Buoyant force from the fluid that has been displaced at the new location. The force of gravity is simply given from the fluid element's density, which is assumed to be unchanged from its original value at z_0.

expanding the lower density up to first order. This gives

$$F_{net} = \delta V g \left(\rho_0(z_o) + \frac{\partial \rho}{\partial z}(z_0)\delta z \right) - \delta V \rho_o(z_o)g. \tag{1.2}$$

The first and third terms in (1.2) cancel, and we write the net force using Newton's second law on the left-hand side to get

$$\delta V \rho_0 \delta \ddot{z} = \delta V g \frac{\partial \rho}{\partial z}(z_0)\delta z \tag{1.3}$$

$$\delta \ddot{z} = \frac{g}{\rho_0}\frac{\partial \rho}{\partial z}\delta z \tag{1.4}$$

$$\delta \ddot{z} \equiv - N^2 \delta z. \tag{1.5}$$

Thus to first order the fluid element behaves exactly like a harmonic oscillator with natural frequency N, which is called the "Brunt-Väisälä" or buoyancy frequency, and this quantity will typically depend on the height z.

1.2 The equations of motion

The derivation for the equations of motion for internal waves starts with the Euler equations, which are given by

$$\rho \frac{D}{Dt}\boldsymbol{v} = \rho\left(\frac{\partial \boldsymbol{v}}{\partial t} + \boldsymbol{v}\cdot\nabla\boldsymbol{v}\right) = -\nabla p + \rho\boldsymbol{a} \tag{1.6}$$

$$\frac{\partial \rho}{\partial t} + \nabla\cdot(\rho\boldsymbol{v}) = 0. \tag{1.7}$$

Here, ρ is the density of the fluid, D/Dt is the material derivative, and $\boldsymbol{v}$ is the velocity which is typically written as $\boldsymbol{v} = u\hat{\boldsymbol{x}} + v\hat{\boldsymbol{y}} + w\hat{\boldsymbol{z}}$, where u, v, and w are the x, y, and z components of the velocity, respectively. Also, the quantity p is the pressure, and $\boldsymbol{a}$ is the acceleration due to external forces. We take our system to be 2D and the only external force to be that due to gravity, and assume small amplitudes which allows us to drop the nonlinear term $\boldsymbol{v}\cdot\nabla\boldsymbol{v}$ in (1.6). This turns (1.6) into the following when each component is written out separately,

$$\rho\frac{\partial u}{\partial t} = -\frac{\partial p}{\partial x}, \qquad \rho\frac{\partial w}{\partial t} = -\frac{\partial p}{\partial z} - \rho g. \tag{1.8}$$

We will look for the equilibrium state of our system. The momentum equation in the x-direction (1.8) gives us

$$0 = -\frac{\partial p_0}{\partial x} \quad \rightarrow \quad p_0 = p_0(z). \tag{1.9}$$

This tells us that the equilibrium state is only a function of the height, or z-coordinate. The z-component of the momentum equation (1.8) gives

$$0 = -\frac{\partial p_0}{\partial z} - \rho_0 g \quad \rightarrow \quad \frac{\partial p_0}{\partial z}(z) = -\rho_0(z)g. \tag{1.10}$$

This gives us a functional relationship between the pressure and density at hydrostatic equilibrium. We will then examine what happens when we perturb about this equilibrium state, which means we take

$$u = \delta u(x, z, t), \quad w = \delta w(x, z, t) \tag{1.11}$$

$$\rho = \rho_0(z) + \delta\rho(x, z, t), \quad p = p_0(z) + \delta p(x, z, t), \tag{1.12}$$

where the δq_i's are the perturbation quantities for their respective variables $\boldsymbol{q} = (u, w, p, \rho)$. We insert (1.11) and (1.12) into the x-component of the momentum equation (1.8), which gives

$$\left(1 + \frac{\delta\rho}{\rho_0}\right) \frac{\partial}{\partial t}\delta u = -\frac{1}{\rho_0}\frac{\partial}{\partial x}(p_0 + \delta p). \tag{1.13}$$

Since the perturbations are small we then take $\delta\rho/\rho_0 \approx 0$, which is the same as saying that the inertial density changes very little. Also, the first term on the right-hand side of (1.13) is zero because the equilibrium pressure p_0 only depends on z. Then we're left with

$$\frac{\partial}{\partial t}\delta u = -\frac{1}{\rho_0}\frac{\partial}{\partial x}\delta p. \tag{1.14}$$

Next we plug (1.11) and (1.12) into the z-component of the momentum equation (1.8) to get

$$\left(1 + \frac{\delta\rho}{\rho_0}\right) \frac{\partial}{\partial t}\delta w = -\frac{1}{\rho_0}\frac{\partial}{\partial z}(p_0 + \delta p) - \left(1 + \frac{\delta\rho}{\rho_0}\right) g. \tag{1.15}$$

Once again we drop the density perturbation in the inertial term on the left-hand side of (1.15), but this time we must keep the same term on the right-hand side of the equation which multiplies g, because otherwise we would

eliminate the lowest order contribution to the dynamics by gravity. The approximation in this context is referred to as the "Boussinesq approximation". This time, the first and third terms on the right-hand side of (1.15) cancel each other due to the hydrostatic equilibrium condition given by (1.10). Then we are left with

$$\frac{\partial}{\partial t}\delta w = -\frac{1}{\rho_0}\frac{\partial}{\partial z}\delta p - \frac{g}{\rho_0}\delta\rho. \tag{1.16}$$

We will now turn our attention to the continuity equation,

$$\frac{\partial \rho}{\partial t} + \nabla \cdot (\rho \boldsymbol{v}) = 0. \tag{1.17}$$

We use a common vector identity to expand the second term on the left-hand side to get

$$\frac{\partial \rho}{\partial t} + \rho \nabla \cdot \boldsymbol{v} + \boldsymbol{v} \cdot \nabla \rho = 0. \tag{1.18}$$

We will take the flow to be incompressible, that is $\nabla \cdot \boldsymbol{v} = 0$, which means (1.18) becomes

$$\frac{\partial \rho}{\partial t} + \boldsymbol{v} \cdot \nabla \rho = 0. \tag{1.19}$$

We then, as was done previously with the momentum equations, plug the perturbations (1.11) and (1.12) into the continuity equation (1.19) to get

$$\frac{\partial}{\partial t}(\rho_0 + \delta\rho) + \delta u \frac{\partial}{\partial x}(\rho_0 + \delta\rho) + \delta w \frac{\partial}{\partial z}(\rho_0 + \delta\rho) = 0. \tag{1.20}$$

The first and third terms are zero because the equilibrium density ρ_0 doesn't depend on time or x, and we drop the fourth and sixth terms because they're

second order in the perturbations. Then we are left with

$$\frac{\partial}{\partial t}\delta\rho = -\frac{\partial \rho_0}{\partial z}\delta w. \tag{1.21}$$

We rewrite the right-hand side of (1.21) in terms of N, and collect the momentum equations for the perturbations (1.14) and (1.16), and also the incompressibility condition. Also, we drop the δ in front of the perturbation quantities, which are now our dynamical variables of interest. Then we have the following collection of equations of motion for linear internal waves:

$$\frac{\partial u}{\partial t} = -\frac{1}{\rho_0}\frac{\partial p}{\partial x}, \qquad \frac{\partial w}{\partial t} = -\frac{1}{\rho_0}\frac{\partial p}{\partial z} - \frac{\rho}{\rho_0}g \tag{1.22}$$

$$\frac{\partial \rho}{\partial t} = \frac{N^2\rho_0}{g}w, \qquad \frac{\partial u}{\partial x} + \frac{\partial w}{\partial z} = 0. \tag{1.23}$$

1.3 The dispersion relation

It will not be explicitly shown here, but using (1.22) and (1.23) we can isolate the vertical velocity w to get a wave equation given by

$$\frac{\partial^2}{\partial t^2}\left(\frac{\partial^2}{\partial x^2} + \frac{\partial^2}{\partial z^2}\right)w + N^2\frac{\partial^2}{\partial x^2}w = 0. \tag{1.24}$$

We then take traveling wave solutions for our dynamical variables. Here we specifically use

$$w = \bar{w}\, e^{i(\boldsymbol{k}\cdot\boldsymbol{x} - \omega t)}, \tag{1.25}$$

where $\bar{w}$ is the constant complex amplitude for w, $\boldsymbol{k}$ is the wave vector and $\boldsymbol{x}$ is the coordinates $\boldsymbol{x} = (x, z)$. Plugging (1.25) for the vertical velocity w in

(1.24) gives

$$\omega^2(k_x^2 + k_z^2)w - N^2 k_x^2 w = 0 \tag{1.26}$$

$$\omega^2 = \frac{k_x^2}{k_x^2 + k_z^2} N^2 \tag{1.27}$$

$$\omega = N \cos\theta. \tag{1.28}$$

Thus the dispersion relation $\omega(\boldsymbol{k})$ from (1.28) for internal waves tells us that the frequency ω of a wave does not depend on the magnitude of the wave vector $\boldsymbol{k}$ at all, but rather its direction θ. In practical usage this is expressed as the angle of the wave vector being determined by the frequency of the waves ω and the buoyancy frequency profile N, since the latter two are typically given. Additionally, for a given frequency of the wave ω, at the locations where the buoyancy frequency N is less than the frequency ω, the wave vector $\boldsymbol{k}$ becomes complex, which is more apparent in (1.27). In particular, the z-component of the wave vector k_z becomes imaginary, which from our traveling wave solutions (1.25), we can see that this means the waves become evanescent, and the location at which this occurs is typically referred to as the "turning depth". Using the dispersion relation (1.28) we can then calculate the phase velocity, which is given by

$$\boldsymbol{c}_p = \frac{\omega}{k}\hat{\boldsymbol{k}} = \frac{N}{k}\cos\theta(\cos\theta\hat{\boldsymbol{x}} + \sin\theta\hat{\boldsymbol{z}}). \tag{1.29}$$

The group velocity is given by

$$\begin{aligned}
\boldsymbol{c}_g =& \frac{\partial \omega}{\partial \boldsymbol{k}} = \frac{\partial \omega}{\partial k_x}\hat{\boldsymbol{x}} + \frac{\partial \omega}{\partial k_z}\hat{\boldsymbol{z}} && (1.30)\\
=& \left(\frac{1}{\sqrt{k_x^2+k_z^2}} - \frac{k_x^2}{(k_x^2+k_z^2)^{3/2}}\right) N\hat{\boldsymbol{x}} + \left(-\frac{k_x k_z}{(k_x^2+k_z^2)^{3/2}}\right) N\hat{\boldsymbol{z}} && (1.31)\\
=& \frac{N}{k}\frac{k_z}{k}\left(\frac{k_z}{k}\hat{\boldsymbol{x}} - \frac{k_x}{k}\hat{\boldsymbol{z}}\right) && (1.32)\\
\boldsymbol{c}_g =& \frac{N}{k}\sin\theta(\sin\theta\hat{\boldsymbol{x}} - \cos\theta\hat{\boldsymbol{z}}). && (1.33)
\end{aligned}$$

However, if we look at the phase and group velocities (1.29) and (1.33), we notice that

$$\boldsymbol{c}_p \cdot \boldsymbol{c}_g = 0. \tag{1.34}$$

Thus the phase and group velocities for linear internal waves are perpendicular to each other, which physically means that while a column of the fluid itself oscillates in one direction (in the direction of the group velocity), the different phases at any given point in time are represented by different columns of the fluid adjacent to any given column. This means the phase travels across the columns, perpendicular to the fluid motion. Figures 1.2 and 1.3 illustrate this.

1.4 The energy flux

The energy density of linear internal waves is given by

$$E = \frac{\rho_0}{2}(u^2+w^2) - \frac{g}{2\,d\rho_0/dz}\rho^2. \tag{1.35}$$

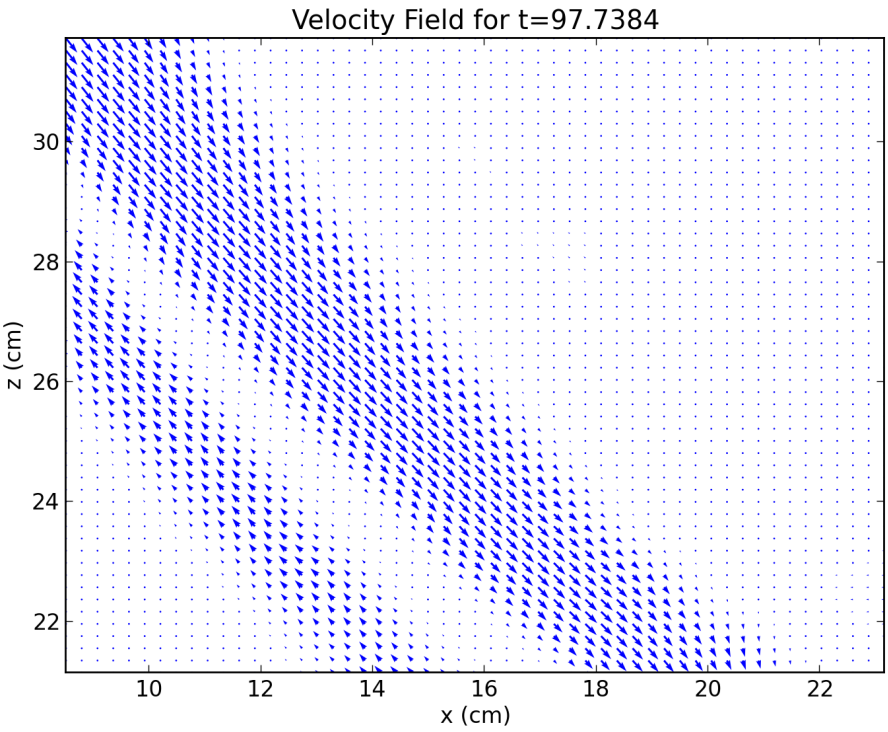

Figure 1.2: A snapshot of the velocity field of an internal wave from experimental data. The size of the arrows represents the magnitude of the velocity at each grid point. The internal wave is created by an oscillating knife-edge topography beyond the window above and to the left, and the beam itself is traveling downward to the right. The group velocity, represented by the velocity of the fluid itself, is along the beam, while the phase propagation is perpendicular to it, across the beam.

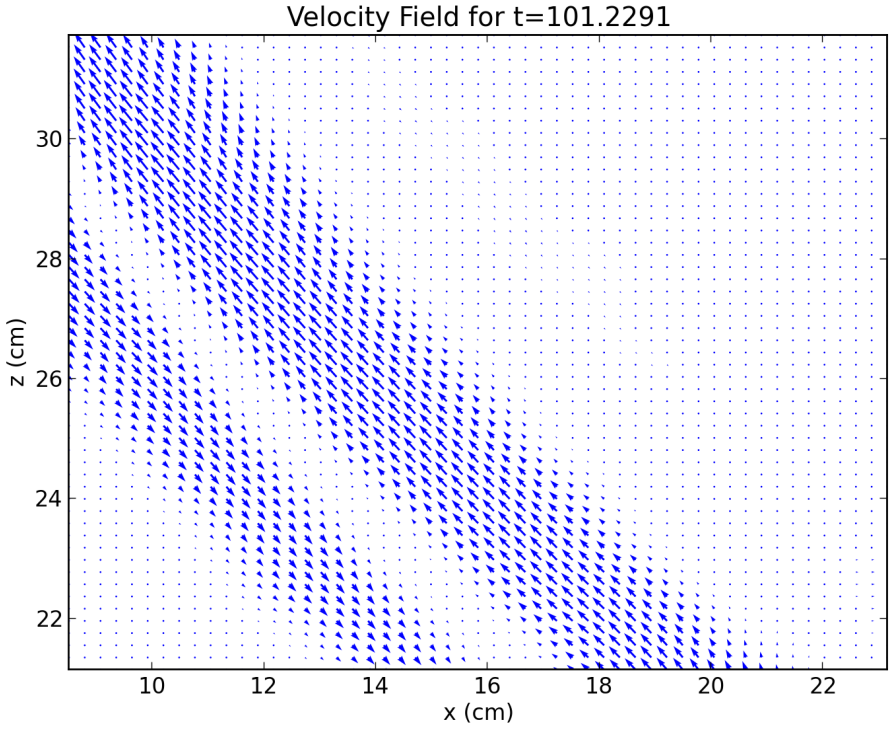

Figure 1.3: A snapshot of the same beam as in the previous figure, but roughly half of a period later. It is apparent that the phase has propagated across the beam, in this case upwards and to the right. The data was taken using particle image velocimetry (PIV), which is discussed in more detail in chapter 2.

The first term of (1.35) is pretty clearly the kinetic energy density, while the second term is the potential energy density, which may not be as obvious. It can be derived by using the harmonic oscillator description of the fluid elements as described in section 1.1, using N as the natural frequency from which the "stiffness constant" can be obtained, and z as the displacement from equilibrium which can be linked to the density perturbation, assuming small perturbations. Energy conservation gives us the relationship between the energy E and energy flux $\boldsymbol{J}$

$$\frac{\partial E}{\partial t} = -\nabla \cdot \boldsymbol{J}. \tag{1.36}$$

We plug (1.35) into (1.36) to get

$$\frac{\partial E}{\partial t} = \rho \left(u \frac{\partial u}{\partial t} + w \frac{\partial w}{\partial t} \right) - \frac{g}{d\rho_0/dz} \rho \frac{\partial \rho}{\partial t} = -\nabla \cdot \boldsymbol{J} \tag{1.37}$$

We then plug in our equations of motion (1.22) and (1.23) into (1.37) to get

$$-u \frac{\partial p}{\partial x} - w \frac{\partial p}{\partial z} = -\nabla \cdot \boldsymbol{J}. \tag{1.38}$$

Using incompressibility $\nabla \cdot \boldsymbol{v} = 0$ this gives the energy flux

$$\boldsymbol{J} = p\boldsymbol{v} = up\,\hat{\boldsymbol{x}} + wp\,\hat{\boldsymbol{z}}. \tag{1.39}$$

Internal waves transport momentum and energy in stably stratified fluids as propagating disturbances that are restored by buoyancy forces. The thermohaline circulation in the ocean stems at least in part from the conversion of energy in large scale tidal and rotational motions into internal waves that

eventually break and deposit their energy into gravitational potential energy through irreversible, small-scale mixing [49, 67]. To determine the role that internal waves play in global ocean mixing, it is important to understand the power present in the internal wave field.

1.5 Obtaining the energy flux in experiments

Theoretical [61, 5, 6, 9, 8, 45, 46, 34, 63, 14, 53, 57, 21, 26, 7, 15, 69] and numerical [32, 39, 42, 43, 52, 50, 73, 35, 36, 59, 22, 23, 24, 60, 13] studies have sought to determine the efficiency of the conversion of energy from tidal and rotational motions over bottom topography into radiated internal waves, but laboratory and field measurements of internal wave power remain scarce, owing to the difficulty in simultaneously measuring the perturbed pressure and velocity fields. Particle image velocimetry [1] has been used in laboratory studies of internal waves to characterize the velocity fields [27, 70, 71, 16, 35, 36, 54, 55], and synthetic schlieren has been used in a few studies to measure density perturbations averaged along the line of sight [2, 25, 10]; however, measurements of the accompanying pressure fields have not been made owing to technical challenges in doing so. In tank-based experiments the time-averaged energy flux has been calculated using data from the velocity or density fields.

Previously, the energy flux has been computed from velocity data by one approach (subsection 1.5.1), and from density perturbation data by two additional approaches (subsection 1.5.2). The aforementioned velocity approach

uses modal decomposition, which our velocity method does not require. The two density approaches provide leading order approximations for the time-averaged energy flux from measurements, but differ from our density approach (described in chapters 3 and 4) in that they cannot capture transient features because they rely on periodicity in time.

1.5.1 Velocity-based energy flux approaches

The velocity-based approaches for calculating the energy flux use continuity, incompressibility, and the linear Euler's equations, with the assumption of time-periodic internal waves. These approaches obtain the energy flux in terms of the stream function [8, 40], obviating the need for the pressure field. The two velocity-based approaches differ in how they calculate the stream function from velocity data: the first approach uses modal decomposition, while the second, our approach, obtains the stream function using path integrals.

The approach that makes a modal decomposition of the velocity field assumes hydrostatic balance (requiring the forcing frequency to be much smaller than the buoyancy frequency) [57]. An application of this approach to a tank-based experiment by Echeverri et al. [16] dropped the hydrostatic balance requirement and added a viscous correction. Most of the energy they observed was contained in the first mode, and the energy flux in modes higher than three was not measurable.

The modal-decomposition approach assumes time periodicity in obtaining the time-averaged energy flux. A periodic signal is obtained using Fourier

transforms, but the accuracy is limited because typical data records are only a few periods long, and also nonlinearities can lead to energy transfer to other frequencies. Further, a modal analysis requires determining the shapes of the vertical modes, but density data spanning the entire fluid depth are often not available. Also, in laboratory experiments the high viscous dissipation limits the results to only the first few modes.

Our velocity-based approach avoids modal decomposition and calculates the stream function directly [40] and is described in chapter 2. Instantaneous velocity fields obtained by particle image velocimetry are used to obtain the stream function. By calculating multiple path integrals between a base point and each point in the domain, this approach averages out some of the noise inherent to experimental measurements; however, accurate results depend on the base point of the integration being either at the boundary of the system, where the stream function is zero, or in a region of the domain where the velocity vanishes. While this approach also relies on time-periodicity of the field, a more complete representation of the stream function is possible compared to the first approach.

1.5.2 Density-perturbation-based energy flux approaches

The first approach that uses the density perturbation field is that of Nash et al. [51], who obtained the energy flux from observational oceanic data for density in a water column. The density perturbation is assumed to be the only contribution to the pressure perturbation, and thus integration of the

density perturbations results in the hydrostatic pressure perturbations. This assumption is valid when the buoyancy frequency of the ocean is much larger than the tidal frequency. The velocity perturbation is calculated from velocity profile measurements by removing the mean time-periodic background velocity and a constant to satisfy the baroclinicity assumption. In regions of the ocean where the most active internal wave fields exist, the time-averaged energy flux has been measured with this approach and used to verify corresponding ocean modeling [62, 3].

The approach of Nash et al. [51] can be applied not only to ocean measurements but also to laboratory measurements if synthetic schlieren and particle image velocimetry are performed simultaneously, as was done by Jia et al. [33]. However, the approach requires both density and velocity data for the entire water column. Additionally, the calculation of the pressure perturbations assumes that there is no contribution from the dynamic pressure, which is reasonable for oceanic data given the slow time scale over which the velocity field changes, but this assumption is invalid for some laboratory experiments and also in ocean settings where the water column is weakly stratified.

A second approach that uses the density perturbation field relies on Boussinesq polarization relations and eigenvector solutions of the linear and inviscid internal wave equations. The polarization relations, which assume periodic flows and plane wave solutions, provide a direct link between the amplitude and phase of any of the velocity components, density perturba-

tion, pressure perturbation, and vertical isopycnal displacement [64]. These relationships are functions of the internal wave frequency. The strength of this approach is that given a periodic or nearly periodic flow, a determination of the velocity field through PIV or isopycnal displacement (using synthetic schlieren) can be used to obtain the pressure and density fields [10]. When the flow field is not strictly periodic but is dominated by a single frequency, spectral methods can be used to decompose the system into its modal contributions, and the polarization relations can be applied to each modal component. This approach provides a direct means for calculating the pressure and thus the energy flux, but the approach relies on accurate spectral decomposition of the fields.

The polarization approach was applied to synthetic schlieren measurements of the isopycnal displacement field by Clark and Sutherland [10], who investigated internal wave beams radiating away from a turbulent patch. To determine the dominant wave frequency and wavenumber, multiple transects normal to the generated beams over multiple periods were analyzed using FFT methods. Then the maximum displacement amplitude based on the spatially averaged envelope was calculated. Combining these two results with the polarization relations yielded the energy flux generated at the dominant frequency and wavenumber pair.

While the approach of Clark and Sutherland [10] provides a notable first step for obtaining energy flux from synthetic schlieren data, it has some limitations. First, it requires that the system be periodic or nearly periodic.

In an aperiodic or transient flow field, the polarization relations require a large number of frequency-wavenumber pairs to reproduce the flow field. The necessity of accurate modal decomposition in both space and time of the synthetic schlieren data makes the averaging process difficult [10]. Another limitation is that the spatial averaging along the beam assumes no viscous dissipation, while the dissipation can be significant for laboratory internal waves [40].

Our density approach, which is described in chapters 3 and 4, uses a Green's function method to calculate the pressure perturbation directly from the density perturbation. The velocity perturbation is calculated directly from the density perturbation using the vertical momentum equation and incompressibility. This removes the limitations in the previous two density methods, and gives an instantaneous energy flux field instead of a time average.

Chapter 2

The energy flux from the velocity field

This chapter is heavily based on our Physics of Fluids publication, Lee et al. [40] [1]. The laboratory data and the Navier-Stokes simulation results were obtained by Matthew Paoletti. Here, we present a method for determining the energy flux and radiated power for propagating internal waves from only velocity field measurements without any knowledge of the pressure field, and we apply the method to results from direct numerical simulations and from laboratory data for tidal flow past a knife edge, for the geometry shown in figure 2.1. To circumvent the need for the perturbed pressure field in equation (1.39), we assume that the velocity field is predominantly two-dimensional, as has been the case in many internal wave studies. A two-dimensional velocity field with zero divergence can be expressed in terms of a scalar field, the stream function ψ, where

$$\boldsymbol{v} = u\hat{\boldsymbol{x}} + w\hat{\boldsymbol{z}} = -\frac{\partial\psi}{\partial z}\hat{\boldsymbol{x}} + \frac{\partial\psi}{\partial x}\hat{\boldsymbol{z}}. \tag{2.1}$$

It is straightforward to derive an expression for the energy flux for two-dimensional internal waves in terms of the stream function (see, e.g., Balm-

[1] F. M. Lee, M. S. Paoletti, H. L. Swinney, and P. J. Morrison. Experimental determination of radiated internal wave power without pressure field data. *Phys. Fluids*, 26:046606, 2014.

forth et al. [8] and Llewellyn Smith and Young [46]). We use such an expression to compute the radiated internal wave power from particle image velocimetry measurements for tidal flow over a knife edge ridge. This wave power is compared with that obtained from companion numerical simulations of the Navier-Stokes equations, where the power can be directly computed from (1.39).

This chapter is organized as follows. The theory behind our approach is presented in section 2.1 and our methods are described in section 2.2. In section 2.3 we show, using data from a numerical simulation of the Navier-Stokes equations, that the internal wave power obtained using the stream function method agrees with that obtained from pressure and velocity field data, provided that appropriate attention is given to the choice of the starting point for the stream function calculation. We then apply the stream function method to calculate internal wave power for laboratory data. The chapter ends with a discussion in section 2.4 and our conclusions in section 2.5.

2.1 Theory

We start with the set of linearized 2-dimensional equations for internal waves found in section 1.2 and they will be shown here again for readability:

$$\frac{\partial u}{\partial t} = -\frac{1}{\rho_0}\frac{\partial p}{\partial x}\,, \qquad \frac{\partial w}{\partial t} = -\frac{1}{\rho_0}\frac{\partial p}{\partial z} - \frac{\rho}{\rho_0}g\,, \tag{2.2}$$

$$\frac{\partial \rho}{\partial t} = \frac{N^2\rho_0}{g}w\,, \qquad \frac{\partial u}{\partial x} + \frac{\partial w}{\partial z} = 0\,, \tag{2.3}$$

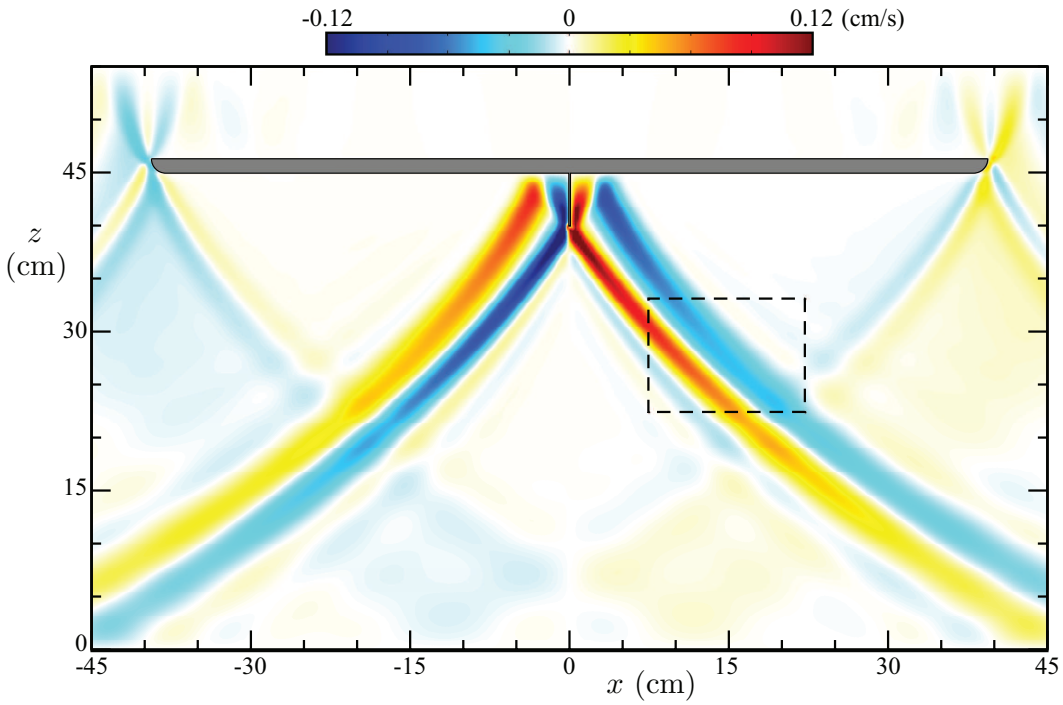

Figure 2.1: This snapshot of the vertical component of the velocity field (color), computed in numerical simulations for the same conditions as our laboratory experiments, reveals internal wave beams generated by knife edge topography (located at the top) that oscillates about $x = 0$; weaker internal waves are generated by the ends of the gray base plate. This numerical simulation mimics the finite-size effects present in the experiments, where waves reflect from the top and bottom boundaries but are damped for $|x| > 45$ cm. The dashed box shows the location of the experimental measurements of the velocity field. The internal wave beams bend because the buoyancy frequency $N(z)$ varies exponentially with z, as described in section 2.2.3. This snapshot is at time $t/T = 7.525$ after initiation of the oscillations, where $T = 2\pi/\omega = 6.98$ s is the oscillation period for a tidal excursion with amplitude $A = 1$ mm. (Fig. 1 from [40])

where x and z are the horizontal and vertical coordinates, respectively, u and w are the corresponding components of the velocity, and p and ρ are the pressure and density perturbations away from a hydrostatic background described by $\rho_0 = \rho_0(z)$, with g the acceleration due to gravity and N the buoyancy frequency,

$$N = \sqrt{\frac{-g}{\rho_0}\frac{\partial \rho_0}{\partial z}}. \tag{2.4}$$

When the density variations are weak enough so as to not significantly affect inertial terms, it is common to replace $\rho_0(z)$ by a constant value denoted ρ_{00}, while N retains a z-dependence. This procedure is a consequence of the Boussinesq approximation. The flux and power formulas we derive will be valid both with and without this approximation.

For 2-dimensional incompressible flow, the perturbation velocity components can be expressed in terms of a stream function ψ, as in (2.1). Then, using (2.1) and neglecting viscous dissipation, the equations of motion (2.2) and (2.3) imply energy conservation as follows:

$$\begin{aligned} \nabla \cdot \boldsymbol{J} = -\frac{\partial E}{\partial t} &:= -\frac{\partial}{\partial t}\left[\frac{\rho_0}{2}(u^2+w^2) - \frac{\rho^2 g}{2\partial\rho_0/\partial z}\right] \\ &= u\,\frac{\partial p}{\partial x} + w\,\frac{\partial p}{\partial z} = -\frac{\partial \psi}{\partial z}\,\frac{\partial p}{\partial x} + \frac{\partial \psi}{\partial x}\,\frac{\partial p}{\partial z}\,. \end{aligned} \tag{2.5}$$

where $\boldsymbol{J}$ is the energy flux. This time however, because we defined a stream function in (2.1), equation (2.5) implies at least two solutions for $\boldsymbol{J}$, e.g.,

$$\boldsymbol{J}_p = -\frac{\partial \psi}{\partial z}\,p\,\hat{\boldsymbol{x}} + \frac{\partial \psi}{\partial x}\,p\,\hat{\boldsymbol{z}} = p(u\,\hat{\boldsymbol{x}} + w\,\hat{\boldsymbol{z}}), \tag{2.6}$$

or

$$\boldsymbol{J}_\psi = \psi \left(\frac{\partial p}{\partial z}\, \hat{\boldsymbol{x}} - \frac{\partial p}{\partial x}\, \hat{\boldsymbol{z}} \right), \tag{2.7}$$

where $\boldsymbol{J}_p$ and $\boldsymbol{J}_\psi$ differ by a gauge condition,

$$\boldsymbol{J}_p = \boldsymbol{J}_\psi + \nabla \times (\psi p\, \hat{\boldsymbol{y}}). \tag{2.8}$$

The form of equation (2.6), $\boldsymbol{J}_p = p\boldsymbol{v}$, is the commonly used expression for the energy flux. However, we will present a form obtained from (2.7) with further manipulation. While the form of (2.6) requires both the velocity and pressure fields over time, the form we use will depend ultimately only on the velocity field.

We assume the stream function can be written as

$$\psi(x, z, t) = Re\{e^{-i\omega t}\varphi(x, z)\}, \tag{2.9}$$

where ω is the angular frequency of the internal waves and φ is the spatially dependent amplitude that is in general complex. Using (2.2), (2.3), (2.7), and (2.9), the following expression for the time-averaged energy flux is obtained:

$$\langle \boldsymbol{J}_\psi \rangle := \frac{i\rho_0}{4\omega} \left[(N^2 - \omega^2) \left(\varphi \frac{\partial \varphi^*}{\partial x} - \varphi^* \frac{\partial \varphi}{\partial x} \right) \hat{\boldsymbol{x}} - \omega^2 \left(\varphi \frac{\partial \varphi^*}{\partial z} - \varphi^* \frac{\partial \varphi}{\partial z} \right) \hat{\boldsymbol{z}} \right]. \tag{2.10}$$

To obtain the result in the Boussinesq approximation one simply replaces ρ_0 in this expression by the constant ρ_{00}.

The functions φ and φ^* can be found from the stream function ψ, which in turn can be obtained from the velocity field. Thus, the energy flux

expression $\langle \boldsymbol{J}_\psi \rangle$ does not require any knowledge of the pressure perturbations, in contrast to the standard form of (2.6), which when averaged over a period becomes

$$\langle \boldsymbol{J}_p \rangle := \frac{1}{T} \int_{t_0}^{t_0+T} dt \; p\boldsymbol{v} = \frac{1}{4} \big[(\mathring{u}\mathring{p}^* + \mathring{u}^*\mathring{p})\, \hat{\boldsymbol{x}} + (\mathring{w}\mathring{p}^* + \mathring{w}^*\mathring{p})\, \hat{\boldsymbol{z}} \big], \tag{2.11}$$

with $T = 2\pi/\omega$, $u(x,z,t) = Re\{e^{-i\omega t}\, \mathring{u}(x,z)\}$, where the symbol $\mathring{u}(x,z)$ denotes the spatially dependent complex amplitude, and similar expressions for w and p (and the complex conjugates u^*, w^*, and p^*) written in terms of their amplitudes.

Our calculation of $\langle \boldsymbol{J}_\psi \rangle$ for the time-averaged energy flux is essentially the same as that in Balmforth et al. [8] and Llewellyn Smith and Young [46], although these authors show an explicit dependence on the tidal velocity amplitude. They also use the Boussinesq approximation and, in addition, Llewellyn Smith and Young [46] make a hydrostatic approximation; more significantly, those authors did not use expression (2.10) to interpret experimental data in the manner we describe below. Note, since the two energy fluxes of (2.6) and (2.7) differ by a curl (the gauge term), the total power given by

$$P = \int_{\partial V} d^2x \, \langle \boldsymbol{J} \rangle \cdot \hat{\boldsymbol{n}} = \int_V d^3x \, \nabla \cdot \langle \boldsymbol{J} \rangle \,, \tag{2.12}$$

where ∂V is the surface bounding a volume V, will be identical when either $\boldsymbol{J}_\psi$ or $\boldsymbol{J}_p$ is inserted.

Thus, only the perturbation velocity field is needed to compute the power produced by topography in the form of internal waves. The caveat is

that because the internal wave equations were used to derive the time-averaged flux fields, the result would only be correct for a system that is dominated by internal waves. Additionally, the equations of motion used were linearized and inviscid, which means if there is a significant presence of higher-order harmonics or appreciable amounts of damping, the results might not be reliable. However, our simulations indicate the method is robust to the inclusion of dissipation. Also, because of the temporal periodicity assumption of (2.9), the system should ideally be in a steady state or close to it. Thus, even though we do not require knowledge of either the perturbation pressure or perturbation density field, use of $\langle \boldsymbol{J}_\psi \rangle$ narrows the scope of applicability to linear internal waves near a steady state with small damping. However, because the method does not require data from these two perturbation fields, obtaining the time-averaged energy flux of internal waves in the ocean is possible. Also, the details of the topography itself do not matter, as long as the velocity fields are solutions of the internal wave equations.

2.2 Methods

This section describes our methods: the computational algorithm for the flux in section 2.2.1, the numerical simulations of the Navier-Stokes equations in section 2.2.2, and the experimental geometry and techniques in section 2.2.3, which also shows that the simulation and experimental results are in good agreement.

2.2.1 Computational algorithm for the flux

A snapshot of the results of the simulations for tidal flow past the knife edge topography (discussed in the next subsection) is illustrated in figure 2.1. In order to compute the energy flux from only the velocity field using (2.10), we must first obtain the stream function ψ by inverting the relations of (2.1). This can be done by using the incompressibility condition (2.3) and integrating (2.1), resulting in

$$\psi(x,z,t) = \int_{x_0}^{x} \mathrm{d}x'\, w(x',z_0,t) - \int_{z_0}^{z} \mathrm{d}z'\, u(x,z',t) + \psi(x_0,z_0,t), \qquad (2.13)$$

where (x_0, z_0) is the starting point for the integration, and $\psi(x_0, z_0, t)$ is an arbitrary integration constant, which we set to zero for our calculations. We discuss the importance of properly choosing the point (x_0, z_0) in section 2.3.2. The integral from (x_0, z_0) to (x, z) is given in (2.13) by first integrating the vertical velocity field along the x-direction and then integrating the horizontal velocity field in the z-direction.

Since the stream function serves as a scalar potential for a conjugate velocity field, its values are theoretically independent of the path of integration. Therefore, we can also compute the stream function in the following manner:

$$\psi(x,z,t) = -\int_{z_0}^{z} \mathrm{d}z'\, u(x_0,z',t) + \int_{x_0}^{x} \mathrm{d}x'\, w(x',z,t) + \psi(x_0,z_0,t). \qquad (2.14)$$

In this case, the stream function is obtained by first integrating the horizontal velocities along a vertical path, and then integrating the vertical velocities along a horizontal path. Indeed, we are not restricted to these two specific

paths as any path between the points (x_0, z_0) and (x, z) can be used to compute the stream function. Thus, we can use any collection of paths that first travel along the grid horizontally, then vertically, and finally horizontally again, as shown in figure 2.2(a). Such paths of integration are given by

$$\psi(x,z,t) = \int_{x_0}^{x_i} dx' w(x', z_0, t) - \int_{z_0}^{z} dz' u(x_i, z', t) + \int_{x_i}^{x} dx' w(x', z, t) + \psi(x_0, z_0, t), \tag{2.15}$$

where x_i is any point between x_0 and x. We can also take paths that first travel vertically, then horizontally, and then vertically again, as shown in figure 2.2(b). These paths of integration are given by

$$\psi(x,z,t) = -\int_{z_0}^{z_i} dz' u(x_0, z', t) + \int_{x_0}^{x} dx' w(x', z_i, t) - \int_{z_i}^{z} dz' u(x, z', t) + \psi(x_0, z_0, t), \tag{2.16}$$

where z_i is any point between z_0 and z.

Statistical errors in the stream function can be minimized by computing the average value for all possible paths for the grid used in the simulation or experiment of the types shown in figure 2.2 (as given by (2.15) and (2.16)) between the starting point (x_0, z_0) and the point of interest (x, z). Figure 2.3 shows a snapshot of our experimental velocity data and the corresponding stream function. We find that stream function values computed from our experimental data using only the two paths defined by (2.13) and (2.14) differ by less than 1% from more computationally intensive multi-path method indicated in figure 2.2. However, the computationally more expensive multi-path

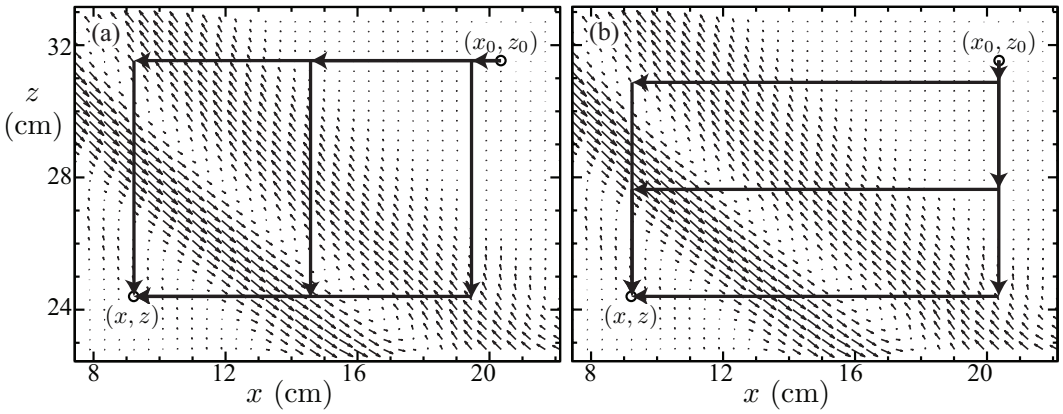

Figure 2.2: The stream function at a point (x, z) is determined by averaging the velocities integrated along paths that (a) first travel horizontally from the starting point (x_0, z_0) towards the point (x, z), then vertically, and then horizontally again, as well as (b) paths that first travel vertically, then horizontally, and then vertically again. The velocity component perpendicular to the path appears in each integrand, and all of the experimental or computational grid points in the box with corners at (x_0, z_0) and (x, z) are used. The conditions for these data are given in the caption for figure 2.1. (Fig. 2 from [40])

method would be preferable for noisy data. Optimization of the multi-path method could be pursued, but we do not do this here.

In principle the choice of the starting point (x_0, z_0) should not affect the computed internal wave power. However, in practice (x_0, z_0) must be chosen carefully, because of the arbitrary integration constant $\psi(x_0, z_0, t)$. Balmforth et al. [8] effectively chose a starting point along the boundary, where they could specify $\psi(x_0, z_0, t) =$ constant owing to the no-penetration boundary condition. We show in section 2.3.2 that choosing a starting point along or near a boundary is the best choice. If the experimental velocity field does not contain points near a boundary, then we find that a starting point away from

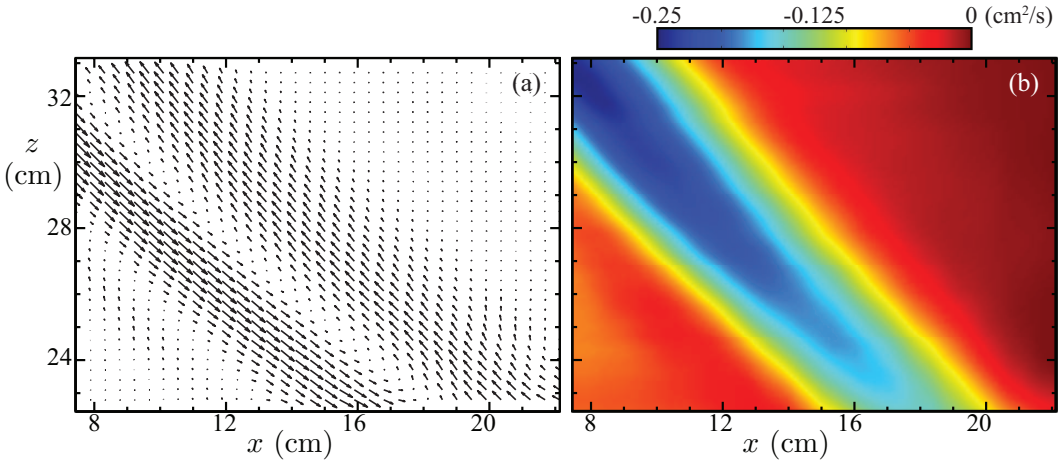

Figure 2.3: (a) A snapshot of the 2-dimensional velocity field used to compute (using (2.15) and (2.16)) (b) the corresponding stream function $\psi(x, z, t)$ with the top right corner as the starting point (x_0, z_0). The conditions for these data are given in the caption for figure 2.1. (Fig. 3 from [40])

the internal wave beams also works well. For example, a point in the upper right corner of figure 2.3 is satisfactory.

After determining the stream function for a tidal period T, the real and imaginary parts of the field $\varphi(x, z)$ must be determined by inverting (2.9). Specifically, we have

$$\varphi(x, z) = \frac{2}{T} \int_{t_0}^{t_0+T} dt\, \psi(x, z, t)\, e^{i\omega t}\,. \tag{2.17}$$

The derivatives of φ that appear in (2.10) are determined by moving them into the integrand and using the relations (2.1):

$$\frac{\partial \varphi}{\partial x} = \frac{2}{T} \int_{t_0}^{t_0+T} dt\, w(x, z, t)\, e^{i\omega t}\,, \tag{2.18}$$

$$\frac{\partial \varphi}{\partial z} = -\frac{2}{T} \int_{t_0}^{t_0+T} dt\, u(x, z, t)\, e^{i\omega t}\,. \tag{2.19}$$

The field φ and its derivatives can then be used in conjunction with a known background density profile $\rho_0(z)$, buoyancy frequency profile $N(z)$, and tidal frequency ω to determine the tidally-averaged energy flux field by (2.10) and the radiated power from (2.12).

2.2.2 Navier-Stokes numerical simulations

We numerically simulate the generation and propagation of internal waves by tidal flow of a stratified fluid over a knife edge ridge by solving the Navier-Stokes equations in the Boussinesq approximation using the code CDP-2.4 [28]. This code is a parallel, unstructured, finite-volume-based solver modeled after the algorithm of Mahesh et al. [47]; all subgrid scale modeling is disabled. By using a fractional-step time-marching scheme and multiple implicit schemes for the spatial operators [29], the code achieves second-order accuracy in both space and time. The following equations are solved for the total density ρ_T, total pressure p_T, and velocity field $\boldsymbol{v} = (u(x,z), w(x,z))$:

$$\frac{\partial \boldsymbol{v}}{\partial t} + \boldsymbol{v} \cdot \nabla \boldsymbol{v} = -\frac{1}{\rho_{00}} \nabla p_T - \frac{g\rho_T}{\rho_{00}} \hat{\boldsymbol{z}} + \nu \nabla^2 \boldsymbol{v} + \frac{F_{\text{tide}}}{\rho_{00}} \hat{\boldsymbol{x}}\,, \tag{2.20}$$

$$\nabla \cdot \boldsymbol{v} = 0\,, \qquad \frac{\partial \rho_T}{\partial t} + \boldsymbol{v} \cdot \nabla \rho_T = D \nabla^2 \rho_T, \tag{2.21}$$

where $\rho_{00} = 1$ g/cm^3 is a reference density, g is the gravitational acceleration, and $\nu = 0.01$ cm^2/s is the kinematic viscosity of fresh water. The salt diffusivity $D = 2 \times 10^{-5}$ cm^2/s is equal to the value for sodium chloride, which is used in the laboratory experiments described above, resulting in a Schmidt number of $\nu/D = 500$. Given the large Schmidt number, the density field does

not mix over the course of our simulations or experiments, which is expected given the lack of wave breaking and overturning for the parameters that we have examined. The tidal flow $\boldsymbol{u}_{\text{tide}} = -\hat{\boldsymbol{x}} A\omega \cos \omega t$ is driven by the tidal force $F_{\text{tide}} = \rho_{00} A\omega^2 \sin \omega t$, where a tidal excursion $A = 0.1$ cm matches the value used in the experiments. The time step is chosen to correspond to 2000 time steps per period for the experiments that have an exponential stratification (described below), and 4000 time steps per period for the case with uniform stratification ($N = \text{const}$) used to compare with analytical theory [46]. The simulations are run long enough to yield a steady-state for at least three periods, which typically requires at least 20 tidal periods.

Two different stratifications are used in the numerical simulations, an exponential $N(z)$ to compare experiments and simulations and a constant $N = 1.55$ rad/s to compare simulations with analytical theory. For the latter case, we choose a tidal frequency of $\omega = 0.255$ rad/s, which yields an internal wave beam slope of $S_{\text{IW}} = \sqrt{\omega^2/(N^2 - \omega^2)} = 1/6$.

The computational grids are generated with Pointwise Gridgen. Grid I, tailored to match the experiment (cf. figure 2.1), spans $-120 < x < 120$ cm and $0 < z < 55$ cm and has approximately 1.7×10^6 control volumes. The simulation topography is composed of a knife edge with height $H = 5$ cm and width $W/H = 0.032$ that is attached to a plate that extends nearly across the computational domain. The structured grid has smoothly varying spatial resolution with grid spacings of $\Delta x = 0.058$ cm and $\Delta z = 0.03$ cm near the topography, and $\Delta x = 2$ cm and $\Delta z = 0.1$ cm for locations far away from

the topography. To mimic the absorbing fiber mesh along the side boundaries in the experiments, we apply a Rayleigh damping term ($\propto \boldsymbol{v} - \boldsymbol{u}_{\text{tide}}$) for $|x| > 50$ cm.

The second domain, Grid II, is designed to minimize finite-size effects to allow for comparisons with the analytical predictions of Llewellyn Smith and Young [46]; for this case N is constant as in the analytical theory. Grid II spans $-400 < x < 400$ cm and $0 < x < 80$ cm and has approximately 1.1×10^6 control volumes. The knife edge in this case has the same dimensions as in the experiment, but the base of the knife edge is centered at $(x = 0, z = 0)$. The grid spacing is $\Delta x = 0.02$ cm and $\Delta z = 0.02$ cm in the vicinity of the knife edge, and smoothly increases to $\Delta x = 2$ cm and $\Delta z = 0.15$ cm along the periphery. Rayleigh damping is applied for $|x| > 300$ cm and $z > 50$ cm to prevent reflections.

In the simulations for both Grid I and for Grid II, no-slip boundary conditions are applied along the topography, top boundary, and bottom boundary, while periodic boundary conditions are used in the x-direction. Convergence tests with the spatial and temporal resolution doubled (halved) changed the computed velocities by less than 1% (4%).

A snapshot of the vertical velocity field computed using Grid I is shown in figure 2.1. The knife edge (centered at $x = 0$) produces four internal wave beams, two that initially propagate upward before reflecting from the base plate, and two others that propagate downward. The edges of the base plate at $|x| = 39.4$ cm also produce weaker internal wave beams. The area shown

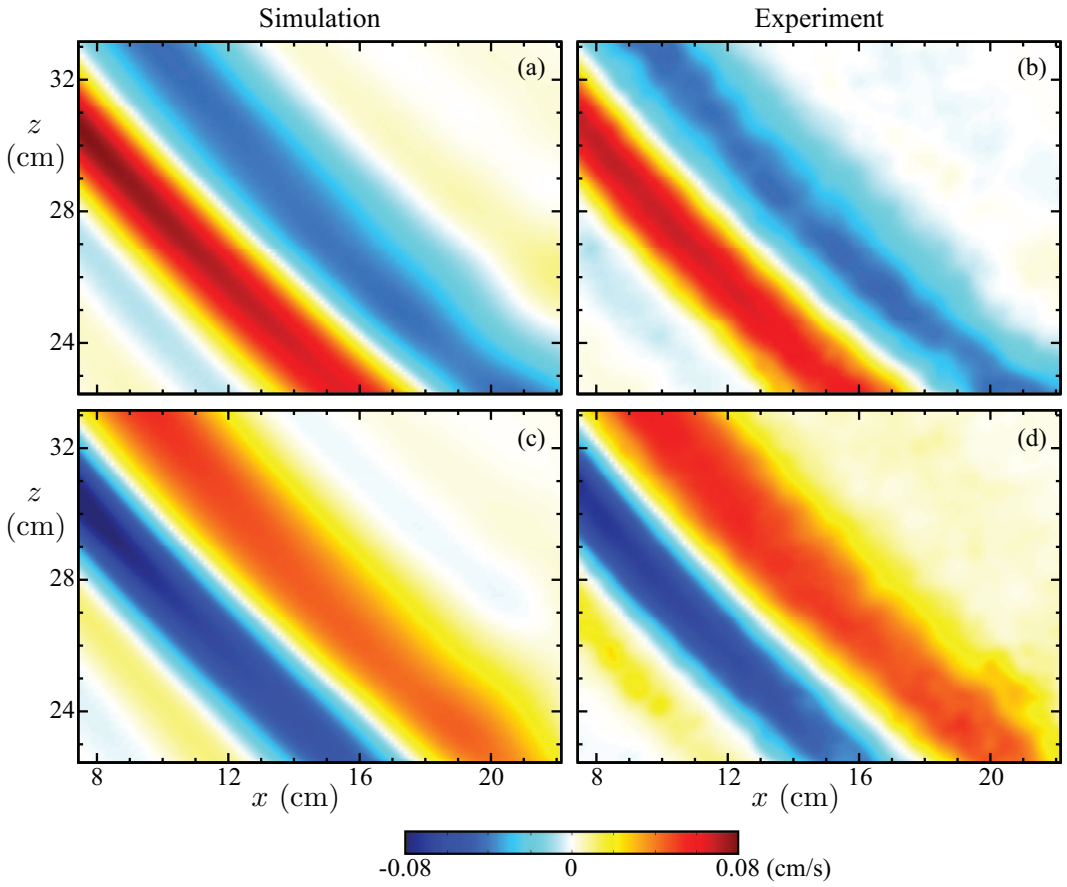

Figure 2.4: Snapshots of the horizontal (top) and vertical (bottom) components of the velocity field (color) determined in simulation (left) and experiment (right) agree well. The measurement region is shown as a dashed box in figure 2.1, and that figure's caption gives the conditions. (Fig. 4 from [40])

corresponds to the laboratory tank; the domain Grid I for the simulations is much wider. Rayleigh damping absorbs the wave beams outside of the area shown. To validate the simulation results, we compare in figure 2.4 the computed velocity field with that measured in the laboratory experiments. The agreement is quite good, as found in our prior comparisons of results from experiments with simulations using the CDP code [35, 36, 54]. The quantitative agreement between simulation and experiment is illustrated by the cross-sections of the velocity and vorticity fields shown in figure 2.5. Similar agreement between simulation and experiment is found for other times and spatial locations.

2.2.3 Experimental techniques

We examine the generation and propagation of internal waves in a glass tank that spans $-45 < x < 45$ cm, $0 < y < 45$ cm, and $0 < z < 60$ cm. The topography is inverted with its base at $z = 45$ cm (see figure 2.1). A knife edge ridge with a height $H = 5$ cm and width (in the x-direction) $W/H = 0.032$ is centered at $x = 0$ and spans the tank in the y-direction. The ridge is connected to a base that spans $-39.4 < x < 39.4$ cm, $1 < y < 44$ cm, and $45 < z < 46.27$ cm, to give a no-slip boundary condition. The edges of the base plate at $|x| = 39.4$ cm are rounded to reduce the spurious generation of internal tides from the ends.

A buoyancy frequency varying exponentially with depth is chosen to model the deep ocean [37, 54]. A density profile corresponding to exponentially

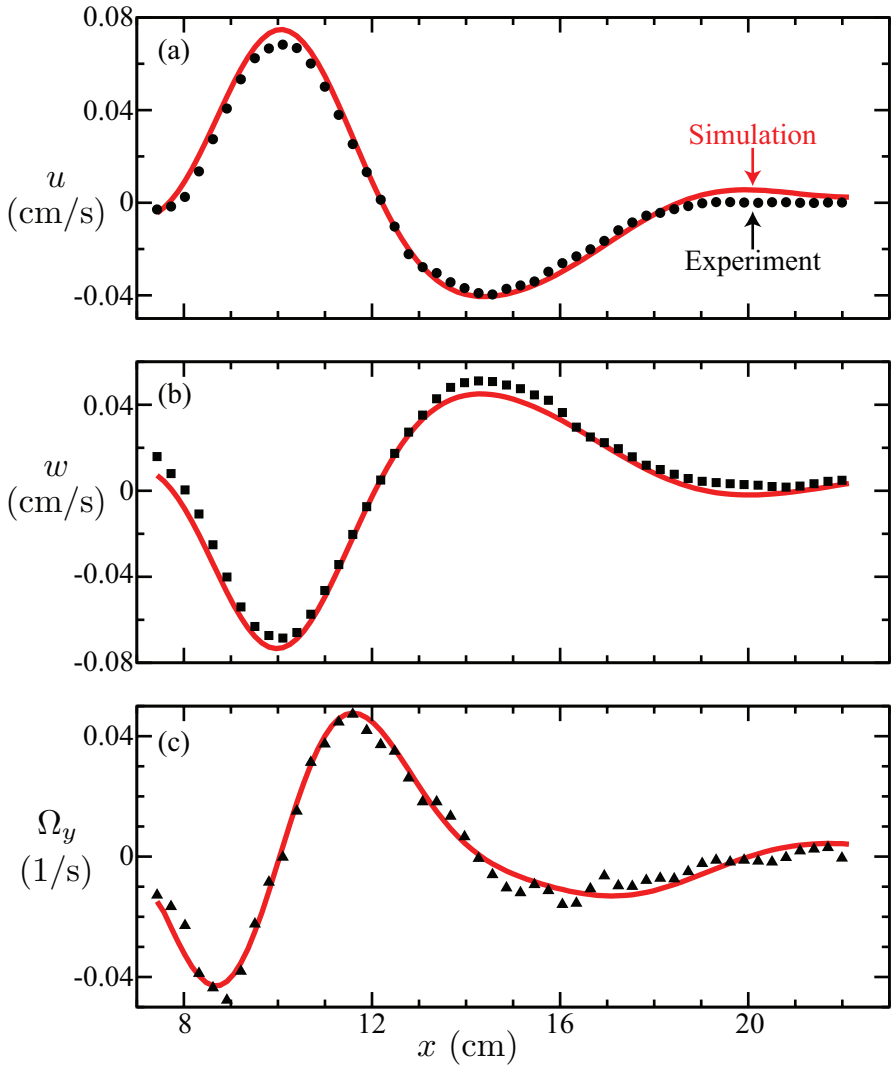

Figure 2.5: Cross-sections of (a) the horizontal velocity component u, (b) vertical velocity w, and (c) vorticity $\Omega_y = (\nabla \times \boldsymbol{v})_y$ measured at $z = 27.7$ cm show excellent agreement between the experimental measurements (black symbols) and numerical simulations (solid (red) curves). The conditions for the measurements and computations are given in the caption of figure 2.1. (Fig. 5 from [40])

varying buoyancy frequency is produced using the generalized double bucket method described by Hill [31]. The density as a function of depth is measured using an Anton Paar density meter; in the bottom of the tank the fluid density is 1098 kg/m^3, and at the top surface (55 cm above the bottom) the density is 1000 kg/m^3. The resultant buoyancy frequency profile is

$$N(z) = Ae^{-Bz} \tag{2.22}$$

over the range $0 < z < 50$ cm, where $A = 1.87$ rad/s and $B = 0.0141$ cm^{-1}. The buoyancy frequency at the base of the experimental topography is $N_{\mathrm{B}} = 0.99$ rad/s, and it exponentially increases towards its maximum value of 1.87 rad/s at $z = 0$ cm at the bottom of the tank.

Tidal flow is generated by oscillating the rigid topography and base plate rather than by driving the fluid over stationary topography. Our velocity measurements, then, are in the reference frame of the tidal flow. The position of the topography is given by

$$x(t) = A[1 - e^{(-2\omega t/3\pi)}] \sin(\omega t), \tag{2.23}$$

where the tidal excursion is $A = 0.1$ cm and the tidal frequency is $\omega = 0.90$ rad/s. The exponential term is added to allow for a gradual increase in the oscillation amplitude, which reaches 99% of its peak value after approximately 3.5 tidal periods [16]. The Reynolds number based upon the topographic height and tidal flow is $Re = A\omega H/\nu = 48$, while the Froude number is $Fr = A\omega/N_{\mathrm{B}}H = 0.02$. To minimize finite-size effects, we reduce

reflections of the internal waves at the side boundaries by placing fiber mesh at $|x| = 45$ cm.

We obtain two-dimensional velocity fields $\boldsymbol{v} = (u, w)$ by particle image velocimetry [1] in a vertical plane along the center of the tank at $y = 22.5$ cm. Hollow glass spheres with diameters $8 < d < 12$ μm and densities in the range $1.05 < \rho < 1.15$ g/cm^3 serve as seed particles, and are illuminated by a 5 mm thick laser sheet with a wavelength of 532 nm and a power of 2 W. We capture the motion of the tracer particles 40 times per period with a 12-bit CCD camera with 1296×966 pixel resolution spanning 15.25 cm in the x-direction and 11.36 cm in the z-direction, as shown schematically by the dashed box in figure 2.1. We use the CIV algorithm developed by Fincham and Delerce [19] to determine the instantaneous velocity fields, which are interpolated to a regular 100×100 grid with spatial resolution $\Delta x = 0.15$ cm and $\Delta z = 0.11$ cm.

2.3 Results

In section 2.3.1 we show, using velocity and pressure field data from a direct numerical simulation, that our method for computing internal wave power from velocity data alone yields results in good accord with the wave power computed in the usual way from velocity and pressure data. In the same section we compare the radiated power given by the analytical predictions of Llewellyn Smith and Young with the power computed in the direct numerical simulations. In section 2.3.2 we examine how the radiated power computed from the velocity field depends on the starting point for the calcula-

tion of the stream function from the velocity data. In section 2.3.3 laboratory measurements of a velocity field are used to compute energy flux, which is found to agree with results obtained from direct numerical simulations that give both velocity and pressure fields.

2.3.1 Internal wave power from fluxes $\langle \boldsymbol{J}_p \rangle$ and $\langle \boldsymbol{J}_\psi \rangle$

In this subsection we compare the power computed by the stream function method with the power computed from the velocity and pressure fields. We assume constant stratification (N = constant) in order to validate the stream function method by comparison with analytic theory. We take ρ_{00} to be the average value of the background density over the domain. The simplest way to compute the power is to take a box centered about the topography and integrate the energy flux normal to the surface along the perimeter of the box. However, because the system is symmetric about the topography, we consider only the rightward-propagating beams. Additionally, we choose a bounding box that is sufficiently tall such that the vertical energy flux through the horizontal segment of the perimeter at $z = 30$ cm is negligible. The vertical energy flux through the horizontal segment at $z = 0$ cm is negligible because of the solid boundary. Thus we compute the power by integrating the horizontal component of the energy flux over a vertical segment from $z = 0$ cm to $z = 30$ cm. The geometry and a snapshot of the computed velocity field are shown in figure 2.6.

The energy flux $\boldsymbol{J}_p$ computed from the pressure in (2.6) and the flux

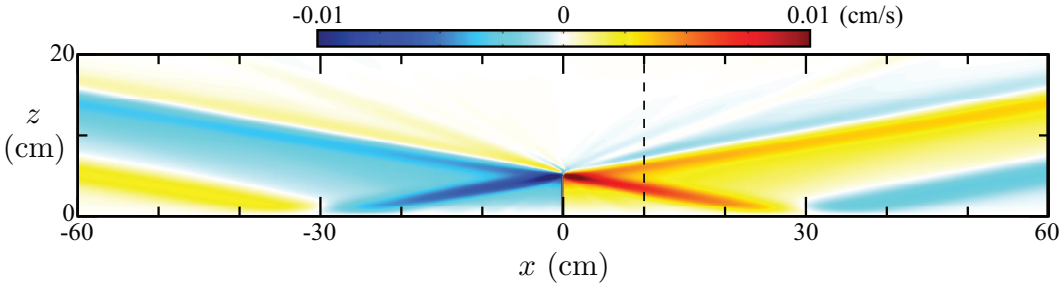

Figure 2.6: A snapshot of the velocity field (color) from a numerical simulation of tidal flow over knife edge topography for a fluid with uniform stratification ($N = \text{const}$). Four internal wave beams are generated at the tip of the knife edge and propagate at constant angles. Measurements of the horizontal energy flux through a cross-section at $x = 10$ cm (dashed line) are shown in Figs. 2.7(a) and 2.8(a). (Fig. 6 from [40])

$\boldsymbol{J}_\psi$ from the stream function in (2.7) differ by $\nabla \times (\psi p \hat{\boldsymbol{y}})$, which represents a gauge transformation. The striking difference between the time-averaged horizontal $\hat{\boldsymbol{x}}$ components of the two fluxes is illustrated in figure 2.7(a). While $\langle \boldsymbol{J}_p \rangle$ and $\langle \boldsymbol{J}_\psi \rangle$ are quite different near the topography, we find that far from the topography they become similar but not identical, as there is no requirement that the time average of the gauge term $\nabla \times (\psi p \hat{\boldsymbol{y}})$ vanish farther away from the topography.

Even though the energy flux fields computed using the pressure and the stream function methods differ, as mentioned before, the radiated power should be the same because it is given by the volume integral of the divergence of the energy flux (cf. (2.12)). Since the divergence of the gauge term $\nabla \times (\psi p \hat{\boldsymbol{y}})$ is zero, it does not contribute to the power. Indeed, the radiated power computed from our simulation data by the stream function and pressure

methods are in excellent agreement, as figure 2.7(b) illustrates; the root-mean-square difference between the two methods is less than 0.5%. This is our main result: the radiated internal wave power can be determined using velocity field data alone.

We now compare the computed radiated power with that predicted by Llewellyn Smith and Young [46] for tidal flow of an inviscid, uniformly stratified fluid over knife edge topography in an infinitely deep ocean (in the absence of rotation),

$$P_{\mathrm{LSY}} = \frac{\pi}{4}\rho_{00}H^2A^2\omega^2\sqrt{N^2-\omega^2}L_y, \tag{2.24}$$

where L_y is the length of the topography in the direction orthogonal to both the tidal flow and gravitational acceleration. We have replaced N with $\sqrt{N^2-\omega^2}$ in Llewellyn Smith and Young [46] to account for nonhydrostatic effects. The radiated internal wave power computed from the stream function and pressure methods is compared to the inviscid theory prediction by using P_{LSY} as normalization in figure 2.7(c). Immediately outside the laminar boundary layer at $x = 1$ cm, our computed values are 99.8% of the value predicted by the inviscid theory. Further away from the topography (increasing x), the power monotonically decreases owing to viscous dissipation, which is not present in theoretical studies [8, 45, 46, 63, 34, 57, 53, 14, 26, 21, 7, 15, 69]. The power rapidly decreases near $x \approx 0$ from dissipation within the laminar boundary layer. Near $x = 25$ cm the internal wave beams reflect from the bottom, producing a boundary layer with enhanced dissipation relative to the freely

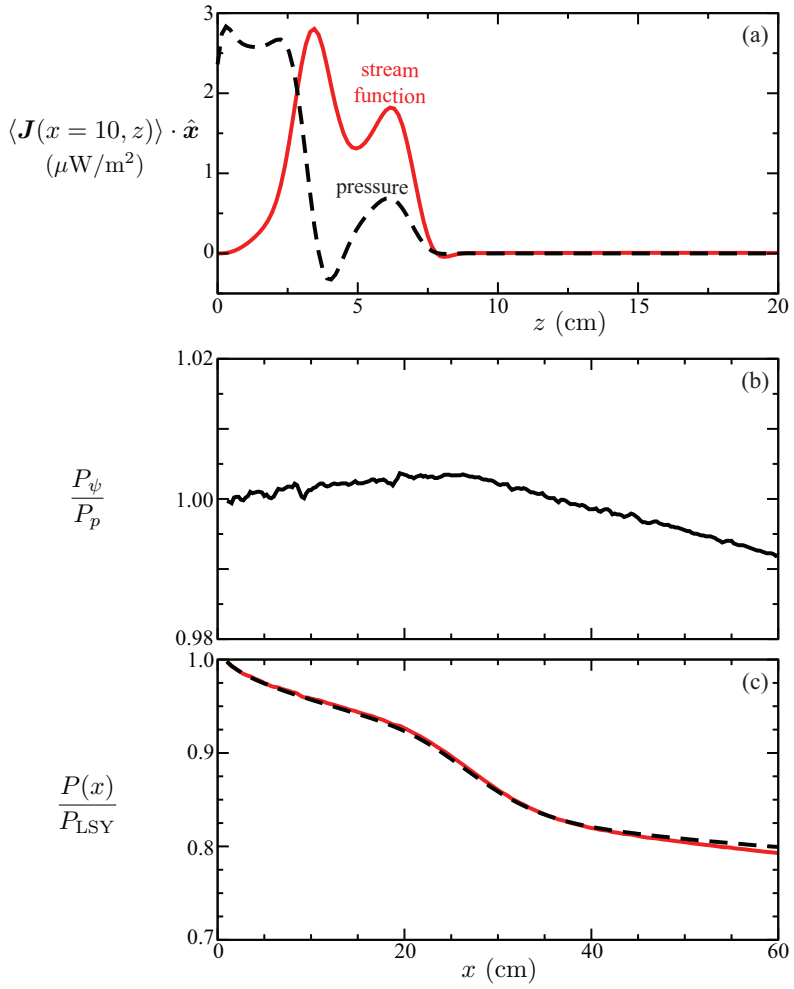

Figure 2.7: (a) The horizontal energy flux $\langle \boldsymbol{J}_\psi \rangle \cdot \hat{\boldsymbol{x}}$ using the stream function method ((2.10), red curve; $x_0 = 60$ cm, $z_0 = 0$) differs from the energy flux $\langle \boldsymbol{J}_p \rangle \cdot \hat{\boldsymbol{x}}$ using the pressure method ((2.11), dashed line). The data is from the numerical simulation with $x = 10$ cm. (b) The total power P_ψ by integrating $\langle \boldsymbol{J}_\psi \rangle \cdot \hat{\boldsymbol{x}}$ (solid (red) curve) is in excellent agreement with the total power P_p from the pressure and velocity, $\langle \boldsymbol{J}_p \rangle \cdot \hat{\boldsymbol{x}}$; the power is shown for vertical cross-sections at different x. (c) The total radiated power from numerical simulations for both approaches are compared with the prediction of Llewellyn Smith and Young [46]. The results agree with inviscid theory near the topography ($x = 0$) but decrease with increasing x due to viscous dissipation. (Fig. 7 from [40])

propagating internal waves in the bulk of the fluid (cf. figure 2.6). Although viscosity was neglected in our derivation of the energy flux, the method seems to account for viscous dissipation quite well.

2.3.2 Dependence on stream function starting point

In order to compute the energy flux and radiated power using only velocity data, the stream function must first be computed by using (2.15) and (2.16), which requires the choice of both a starting point (x_0, z_0) and a value for the arbitrary integration constant $\psi(x_0, z_0, t)$. Balmforth et al. [8] effectively chose a point on the boundary and set $\psi(x_0, z_0, t) =$ constant, which is justified by the no-penetration boundary condition. However, experimental observations often do not include points on a solid boundary, and that is the case in our experiment (see the dashed box in figure 2.1). Therefore, as a substitute for solid boundary points we choose effective boundary points starting as far away from the internal wave beams as possible, assuming that the stream function values at those points closely match those of the solid boundary and are thus constant in time. Further, since the value of the constant itself does not change the flux, we choose $\psi(x_0, z_0, t) = 0$.

To explore the effects of the choice of starting point on the calculation of the stream function, we consider internal waves generated by tidal flow of a uniformly stratified fluid ($N =$ constant) over a knife edge for the domain 2 (Grid II) described in section 2.2.2. This domain, larger than the experimental domain (domain 1), removes the laboratory domain's finite-size effects and

spurious generation of additional internal waves from the base plate. The snapshot of the vertical velocity field in figure 2.6 shows the four internal wave beams that are generated by the knife edge with its base at $(x = 0, z = 0)$. Two of the internal wave beams radiate upward, and two other beams initially propagate downward, reflect near $x = \pm 25$ cm, and then propagate upward. The waves are absorbed by Rayleigh damping before reflecting from the boundaries.

The horizontal energy flux and the total radiated internal wave power are shown in figure 2.8 for three starting points for the computation of the stream function (with $\psi(x_0, z_0, t) = 0$). The horizontal energy fluxes computed from the three representative starting points differ significantly; the starting point with $z_0 = 4$ cm is between the bottom boundary and the reflected wave that propagates to the right; the starting point with $z_0 = 12$ cm is between the two rightward-propagating internal waves; and the starting point with $z_0 = 20$ cm is above both internal waves but far from any solid boundary. The energy flux is strongest for $z_0 = 4$ cm. The energy flux has a similar structure for $z_0 = 20$ cm, but the flux is much lower for $z_0 = 12$ cm.

The total radiated power P_ψ integrated for vertical cross-sections at different x is shown in figure 2.8(b) for the three different starting points of the stream function calculation. P_ψ is normalized by the power computed by the pressure method, P_p. For $x > 30$ cm, the power P_ψ computed for starting points outside of the internal wave beams ($z_0 = 4$ and $z = 20$ cm) is in excellent agreement with P_p; the rms difference is 0.5% for $z_0 = 4$ cm and

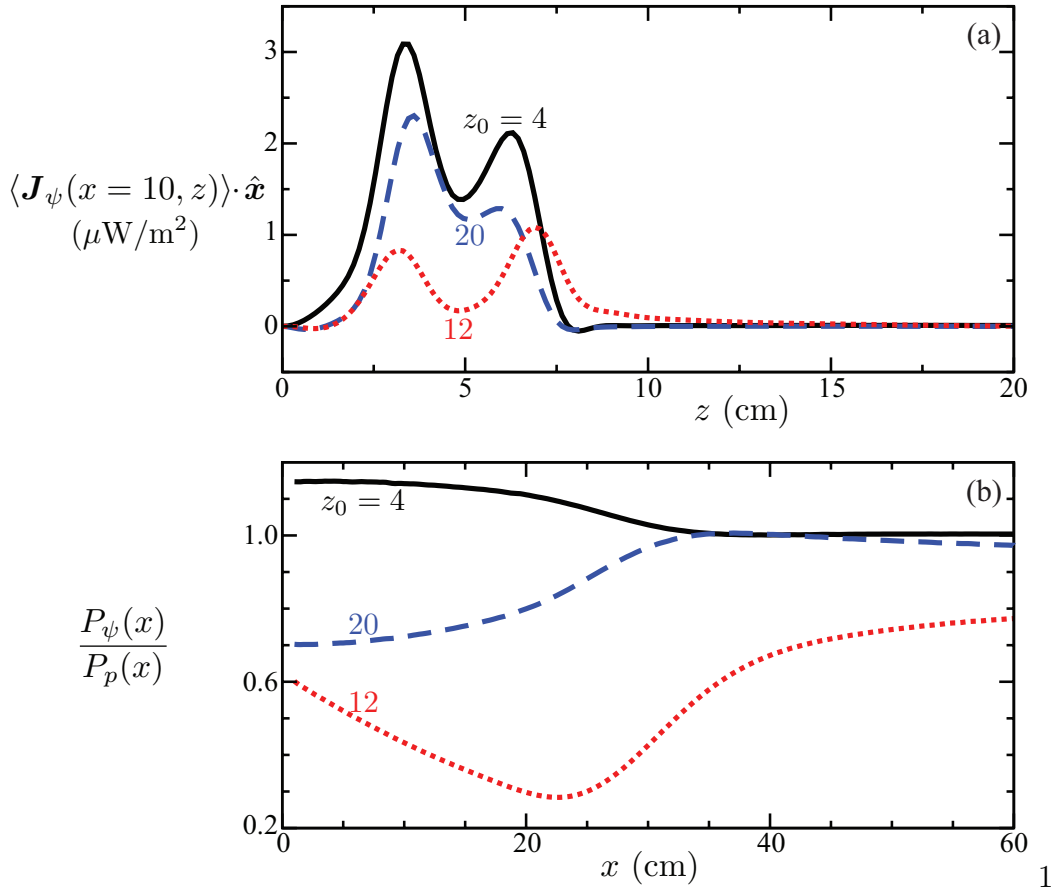

Figure 2.8: (a) The horizontal energy flux $\langle \boldsymbol{J}_\psi \rangle \cdot \hat{\boldsymbol{x}}$ determined by the stream function method (equations (2.10), (2.13), and (2.14)) for starting points with $x_0 = 60$ cm and $z_0 = 4$, 12, and 20 cm. (b) The internal wave power P_ψ obtained by integrating the horizontal flux vertically for different x, normalized by the power P_p computed using the pressure method, for the three different stream function calculation starting points. (Fig. 8 from [40])

1% for $z_0 = 20$ cm. For $x < 30$ cm (i.e., farther away from the $x_0 = 60$ cm starting point), P_ψ computed with $z_0 = 4$ cm is larger than P_p by as much as 15%, and for $z_0 = 20$ cm, P_ψ is smaller than P_p by as much as 30%. For the starting point located between the internal wave beams ($z_0 = 12$ cm) (cf. figure 2.6), P_ψ is smaller than P_p by at least 20% and as much as 70%. This example illustrates that the starting point for a stream function calculation of the flux should be outside of the internal wave beams, and the total internal wave power should be obtained for cross-sections far enough away from the topography to avoid near-field effects and close enough to the starting point for the stream function to reduce the cumulative error from quadrature over long paths.

2.3.3 Comparison of experiment and numerical simulation

Figure 2.9 compares the energy flux field from the numerical simulations $\langle \boldsymbol{J}_\psi^{\mathrm{sim}} \rangle$ with that from a laboratory experiment $\langle \boldsymbol{J}_\psi^{\mathrm{expt}} \rangle$ for the same conditions. In this figure it is seen that the energy flux computed by the stream function method for the simulation and laboratory agree well.

The radiated internal wave power computed for the simulation data by integrating the energy flux across the beam is 3.09 nW (per cm of topography) and 3.01 nW, respectively for the integrals of $\langle \boldsymbol{J}_p^{\mathrm{sim}} \rangle$ and $\langle \boldsymbol{J}_\psi^{\mathrm{sim}} \rangle$ across the beam; the internal wave power obtained by integrating the energy flux obtained from the laboratory data is 2.83 nW. The difference between the experimental and simulation results for the radiated power arises from differences between

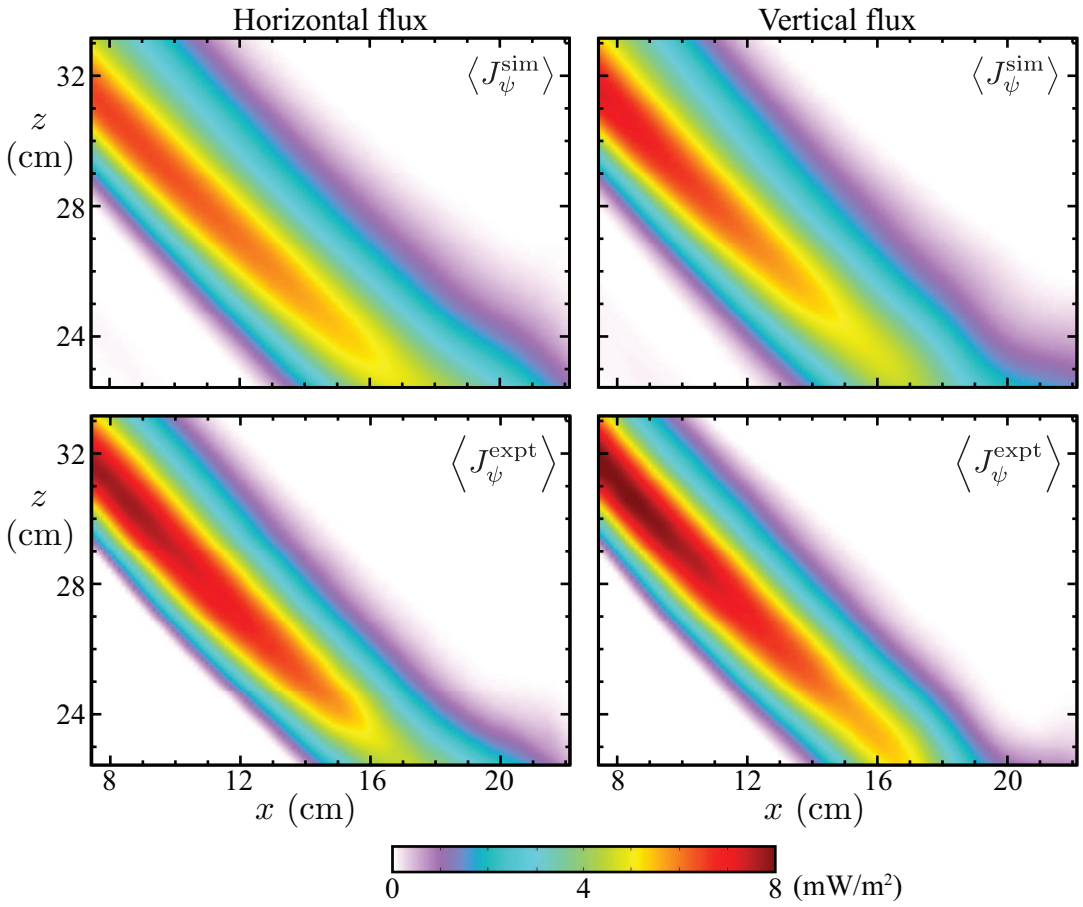

Figure 2.9: The tidally averaged horizontal (left) and vertical (right) energy flux computed by the stream function method for simulation data (top), compared with the method applied to laboratory data (bottom). The region shown is indicated by the dashed rectangle in figure 2.1. (Fig. 9 from [40])

the laboratory system and the simulation rather than from errors in the stream function methodology, which has been validated by using pressure and velocity data from the numerical simulation. The differences between the experiment and simulation include the viscosity, which is constant in the simulation but varies in the experiment by 20% from the tank bottom to the fluid surface; the sidewall boundary condition, which in the laboratory tank is absorbing because the walls are lined with a fiber mesh to reduce reflections; and the shape of the ends of the base plate on which the topography was mounted. Despite these differences the agreement is within 10%.

2.4 Discussion

The method presented for determining energy flux and radiated power for internal waves using only velocity field data could provide opportunities for laboratory experiments and field measurements that go beyond the capabilities of existing theory. While theoretical [38] and experimental [54] studies have examined the viscous decay of the velocity field for propagating internal waves in arbitrary stratifications, theoretical studies of internal wave generation for flow over topography have been for inviscid fluids [9, 8, 46, 34, 57, 53, 7, 15]. Figure 2.7(c) shows that the stream function method yields the decay of the wave power as well as the generated power. Therefore, velocity measurements can be used to characterize both the conversion of tidal motions to internal waves and the viscous decay as the waves propagate away from the topography.

Theoretical studies of the conversion of tidal motions to internal wave

power have focused on laminar flow over the topography, but the boundary currents can become intense and unstable, particularly for critical topography where the slope of the topography is equal to the local slope of the internal wave beams [71, 22, 23, 24, 13]. Indeed, recent numerical simulations have found that turbulence generated near critical topography can reduce the radiated internal wave power [60]. While the turbulence is 3-dimensional, the far field internal beams can be predominantly 2-dimensional [2] and hence could be determined by the stream function method.

2.5 Conclusions

We have shown that the energy flux and the integrated wave power for 2-dimensional internal waves can be determined using knowledge of only the velocity field, which can be written in terms of a single scalar field, the stream function. The energy flux field and radiated power can be computed from (2.10) and (2.12), in analogy with the methods used in prior theoretical work [8, 46, 34, 57, 53, 7, 15]. We have tested the stream function method for determining internal wave flux and power using results obtained for tidal flow over a knife edge, computed with a numerical simulation code that has been validated in previous studies [35, 36, 54, 13]. The results for the radiated internal wave power obtained from the stream function and pressure methods are found to agree within one percent, *if* the starting point for the stream function calculation is chosen near a boundary or far from the internal wave beams. We also made laboratory measurements of the velocity field for tidal flow past

a knife edge and used those data to determine the internal wave power, which agreed with the numerical simulation results within ten percent. Given the excellent agreement between the results from the pressure and stream function approaches for the simulation data, we believe the agreement between the experiment and simulation could be improved by designing an experiment that better satisfied the assumptions of the simulations.

Appendix A provides links for a Matlab code with a graphical user interface for the stream function method of determining energy flux and internal wave power from 2-dimensional velocity field data. A step-by-step description of the algorithm and its implementation are also included.

Chapter 3

The energy flux from the density perturbation field for uniform N

This chapter is heavily based on our Physical Review Fluids publication, Allshouse et al. [4] [1]. The laboratory data and the Navier-Stokes simulation results were obtained by Michael Allshouse. Here, using a Green's function approach, we present a more generally applicable method for calculating the instantaneous pressure, velocity, and energy flux from the density perturbation field; thus the method can be applied to both periodic and aperiodic data. The method was developed for use on laboratory density perturbation data but should also be applicable to field observations. This chapter is organized as follows. Section 3.1 presents the derivation of our method for calculating the instantaneous energy flux field $\boldsymbol{J}$. In subsection 3.1.1 we start with the linear Euler's equations and derive expressions for the pressure perturbation and the two velocity components in terms of the density perturbation. These allow for a general expression for $\boldsymbol{J}$ in terms of the density perturbation field. In subsection 3.1.2 a Green's function method is used to solve for the pressure perturbation field from a density perturbation field, which will be given

[1] M. R. Allshouse, F. M. Lee, P. J. Morrison, and H. L. Swinney. Internal wave pressure, velocity, and energy flux from density perturbations. *Phys. Rev. Fluids*, 1:014301, 2016.

by synthetic schlieren data. Section 3.2 describes our numerical simulations and experiments and compares their results. In subsection 3.3.1, our method is verified by comparing results for $\boldsymbol{J}$ calculated from a simulated density perturbation field with results obtained directly from numerical simulations. Subsection 3.3.2 presents the results of applying the method to laboratory data taken in a portion of the domain. Finally, section 3.4 presents our conclusions and discusses broader applications of our method. To aid in applying this method, we have developed a Matlab GUI, *EnergyFlux*, which is discussed in the appendix and provided in the supplementary materials.

3.1 Theory

Our approach uses the density perturbation field to calculate the instantaneous pressure, velocity, and energy flux fields. Starting with the linear Euler's, continuity, and incompressibility equations, we derive expressions for the pressure and velocity perturbation fields in terms of the density perturbation field. Section 3.1.1 presents these relationships without assuming any particular form for the buoyancy frequency N. For the specific case of uniform N, a solution for the pressure perturbation field is found in terms of the density perturbation field in section 3.1.2.

3.1.1 Energy flux from a density perturbation field

To calculate the energy flux from the density perturbation field, the pressure and velocity must first be obtained in terms of the density pertur-

bations. Assuming inviscid flow, we start with the two-dimensional Euler's equations, which give the linear wave equations that are the foundation of our approach. We obtain a partial differential equation that gives the pressure perturbations instantaneously from the density perturbation field, which acts as a source term, and then the incompressibility and the continuity equations together yield both velocity components as functions of the density perturbations.

As before, for readability we show here again the linearized two-dimensional Euler's equations for the density $\rho_0(z)+\rho(x,z,t)$ and pressure $p_0(z)+p(x,z,t)$, where $\rho_0(z)$ and $p_0(z)$ are in hydrostatic balance, and the velocity $\boldsymbol{v}(x,z,t)$:

$$\frac{\partial u}{\partial t} = -\frac{1}{\rho_0}\frac{\partial p}{\partial x}\,, \qquad \frac{\partial w}{\partial t} = -\frac{1}{\rho_0}\frac{\partial p}{\partial z} - \frac{\rho}{\rho_0}g\,, \tag{3.1}$$

$$\frac{\partial \rho}{\partial t} = \frac{N^2\rho_0}{g}w\,, \qquad \frac{\partial u}{\partial x} + \frac{\partial w}{\partial z} = 0\,, \tag{3.2}$$

where g denotes the gravitational acceleration, x and z are the horizontal and vertical coordinates, respectively, u and w are the corresponding components of the velocity $\boldsymbol{v}$, and the buoyancy frequency N is given by

$$N^2 = -\frac{g}{\rho_0}\frac{d\rho_0}{dz}. \tag{3.3}$$

The energy density is given by

$$E = \frac{\rho_0}{2}(u^2+w^2) - \frac{\rho^2 g}{2\,d\rho_0/dz}, \tag{3.4}$$

which together with the energy flux $\boldsymbol{J}$ satisfies conservation of energy,

$$\frac{\partial E}{\partial t} + \nabla \cdot \boldsymbol{J} = 0. \tag{3.5}$$

Using the equations of motion (3.1) and (3.2), we have the energy flux from (3.5),

$$\boldsymbol{J} = up\hat{\boldsymbol{x}} + wp\hat{\boldsymbol{z}}\,, \tag{3.6}$$

which is the main object of our consideration.

Next, using (3.1) to obtain the time derivative of $\nabla \cdot \boldsymbol{v}$ yields

$$\frac{\partial}{\partial x}\frac{\partial u}{\partial t} + \frac{\partial}{\partial z}\frac{\partial w}{\partial t} = \frac{\partial}{\partial x}\left(-\frac{1}{\rho_0}\frac{\partial p}{\partial x}\right) + \frac{\partial}{\partial z}\left(-\frac{1}{\rho_0}\frac{\partial p}{\partial z} - \frac{\rho}{\rho_0}g\right) = 0 \tag{3.7}$$

which after applying the chain rule taking care to account for the z-dependence of ρ_0 and substitutions involving (3.3) gives the following partial differential equation:

$$\frac{\partial^2 p}{\partial x^2} + \frac{\partial^2 p}{\partial z^2} + \frac{N^2}{g}\frac{\partial p}{\partial z} = -N^2\rho - g\frac{\partial \rho}{\partial z}. \tag{3.8}$$

Equation (3.8), together with boundary conditions discussed in section 3.1.2, yields the pressure perturbation field from a source that is determined by the density perturbation field at any given instant in time. We denote the solution of (3.8) by the functional $p[\rho]$.

To obtain a more intuitive and easier-to-solve Helmoltz-like equation, we transform (3.8) to a standard form in terms of a new variable q:

$$p(x,z) = q(x,z)\exp\left[-\frac{1}{2g}\int^z dz' N^2(z')\right]. \tag{3.9}$$

The relationship between q and ρ is then

$$\frac{\partial^2 q}{\partial x^2} + \frac{\partial^2 q}{\partial z^2} - \left(\frac{N}{g}\frac{\partial N}{\partial z} + \frac{N^4}{4g^2} \right) q = -\left(N^2 \rho + g \frac{\partial \rho}{\partial z} \right) \exp\left[\frac{1}{2g} \int^z dz' N^2(z') \right], \tag{3.10}$$

which when solved gives $p[\rho]$ via (3.9).

The vertical component of the velocity w is given by rearranging (3.2),

$$w = \frac{g}{N^2 \rho_0} \frac{\partial \rho}{\partial t}\,. \tag{3.11}$$

Using w, we find the horizontal component of the velocity u from the incompressibility condition by integrating in x,

$$u = -\int^x dx\, \frac{\partial w}{\partial z} = -\int^x dx\, \frac{\partial}{\partial z}\left(\frac{g}{N^2 \rho_0} \frac{\partial \rho}{\partial t} \right)\,. \tag{3.12}$$

The integration constant is zero if we take the initial point of integration to be at a location where the horizontal velocity is known to be zero.

Finally, using (3.11) and (3.12), we obtain the desired result, the instantaneous energy flux (3.6) entirely in terms of the density perturbation field ρ, provided we know $p[\rho]$, the solution of (3.8) for the pressure perturbation field,

$$\boldsymbol{J}(x,z,t) = -p[\rho]\, g \int^x dx\, \frac{\partial}{\partial z}\left(\frac{1}{N^2 \rho_0} \frac{\partial \rho}{\partial t} \right) \hat{\boldsymbol{x}} + \frac{p[\rho]\, g}{N^2 \rho_0} \frac{\partial \rho}{\partial t}\, \hat{\boldsymbol{z}}. \tag{3.13}$$

3.1.2 Green's function approach for uniform N

Before solving (3.10) for the pressure perturbations, the boundary conditions must be specified. A detailed discussion of the experimental setup will

be given in section 3.2.2, but for now we note that our boundary conditions are for a domain that will represent laboratory data taken from a tank where the top and bottom boundaries are visible, while the left and right boundaries are not, because they are taken to be far away. As an approximation of our laboratory domain, periodic boundary conditions are assumed for the left ($x = 0$) and right ($x = l$) boundaries, and no-flux boundary conditions are assumed for the top ($z = 0$) and bottom ($z = h$) of the domain. The periodic boundary conditions for the horizontal direction are reasonable since disturbances do not sense the actual boundary in that direction, while the no-flux conditions in the vertical direction are appropriate since the top and bottom boundaries of the measurement window are the solid boundary of the tank and the free surface.

The boundary conditions required for solving (3.8) follow from force balance. For the horizontal periodic boundary conditions, the first equation of (3.1) implies

$$\left.\frac{\partial p}{\partial x}\right|_{x=0} = \left.\frac{\partial p}{\partial x}\right|_{x=l}. \tag{3.14}$$

Similarly, applying the no-flux boundary condition on the top and bottom boundaries requires the vertical velocity there to be zero for all time, and this implies zero vertical force there as well. Then the second equation of (3.1) gives

$$\left.\left(\frac{\partial p}{\partial z} + \rho g\right)\right|_{z=0} = \left.\left(\frac{\partial p}{\partial z} + \rho g\right)\right|_{z=h} = 0. \tag{3.15}$$

However, the first equation of (3.2) tells us that the density perturbation does not change with time at the top and bottom boundaries since the vertical

velocity is zero there. Since initially the density perturbation on those boundaries is zero, it remains zero for all time. Thus (3.15) gives the following boundary condition for the top and bottom boundaries:

$$\left.\frac{\partial p}{\partial z}\right|_{z=0} = \left.\frac{\partial p}{\partial z}\right|_{z=h} = 0. \tag{3.16}$$

Because of the transformation (3.9), the boundary conditions on p, (3.14) and (3.16), imply the following boundary conditions on the variable q:

$$\begin{aligned} \left.\frac{\partial q}{\partial x}\right|_{x=0} &= \left.\frac{\partial q}{\partial x}\right|_{x=l} \\ \left.\frac{\partial q}{\partial z} - \frac{N^2}{2g}q\right|_{z=0} &= \left.\frac{\partial q}{\partial z} - \frac{N^2}{2g}q\right|_{z=h} = 0. \end{aligned} \tag{3.17}$$

In this section we consider the case where the buoyancy frequency profile is taken to be uniform, $N = N_0$. For such a profile, the equation for the pressure perturbation field (3.8) simplifes to give

$$\frac{\partial^2 q}{\partial x^2} + \frac{\partial^2 q}{\partial z^2} - \frac{N_0^4}{4g^2}q = -f(x,z), \tag{3.18}$$

where

$$f(x,z) = \left(N_0^2\rho + g\frac{\partial \rho}{\partial z}\right)\exp\left(\frac{N_0^2}{2g}z\right), \tag{3.19}$$

and the boundary conditions remain identical to (3.17) with the N_0 substituted in for N.

Next, the variables q and f are Fourier expanded in the horizontal

direction,

$$\begin{aligned} q(x,z) &= \mathrm{Re}\left\{ \sum_k Q_k(z) e^{-ikx/l} \right\} \\ f(x,z) &= \mathrm{Re}\left\{ \sum_k F_k(z) e^{-ikx/l} \right\}, \end{aligned} \tag{3.20}$$

where $k = 2\pi n/l$ with n being a positive integer. These series expansions can be done because the horizontal extent of the domain is finite, and they automatically satisfy the boundary conditions for the x-direction. This allows the dimensionality of the problem to be reduced to one. Then (3.18) and the remaining boundary conditions for the vertical direction become

$$\frac{\partial^2 Q_k}{\partial z^2} - \kappa^2 Q_k = - F_k, \tag{3.21}$$

$$\frac{\partial Q_k}{\partial z} - \frac{N_0^2}{2g} Q_k \bigg|_{z=0} = \frac{\partial Q_k}{\partial z} - \frac{N_0^2}{2g} Q_k \bigg|_{z=h} = 0, \tag{3.22}$$

where $\kappa^2 = k^2 + N_0^4/4g^2$. Solving for Q_k for each mode k and summing over all the modes gives us q which will then give p, the pressure perturbation field.

Equation (3.21) can be solved by taking a Green's function approach. This is as far as we can take the solution analytically, since the source term F_k in (3.21) is given from laboratory data. The Green's function G_k for this case satisfies

$$\frac{\partial^2 G_k}{\partial z^2} - \kappa^2 G_k = \delta(z - z'), \tag{3.23}$$

$$\frac{\partial G_k}{\partial z} - \frac{N_0^2}{2g} G_k \bigg|_{z=0} = \frac{\partial G_k}{\partial z} - \frac{N_0^2}{2g} G_k \bigg|_{z=h} = 0. \tag{3.24}$$

Considering (3.23) on each side of the jump at $z = z'$,

$$\frac{\partial^2 G_k}{\partial z^2} - \kappa^2 G_k = 0\,, \tag{3.25}$$

gives a solution of the form

$$G_k(z,z') = \begin{cases} G_k^{z>z'} = Ae^{\kappa z} + Be^{-\kappa z}, & z > z' \\ G_k^{z<z'} = Ce^{\kappa z} + De^{-\kappa z}, & z < z', \end{cases} \tag{3.26}$$

where the constants A, B, C, and D are determined by the following matching conditions:

$$G_k^{z>z'}(z,z')\Big|_{z=z'} = G_k^{z<z'}(z,z')\Big|_{z=z'}, \tag{3.27}$$

$$\frac{\partial}{\partial z} G_k^{z>z'}(z,z')\Big|_{z=z'} = 1 + \frac{\partial}{\partial z} G_k^{z<z'}(z,z')\Big|_{z=z'}. \tag{3.28}$$

After applying the matching conditions (3.27), (3.28), and the boundary conditions (3.24), the following Green's function (3.26) for mode k is obtained:

$$G_k(z,z') = \frac{1}{\gamma}\left[\kappa_+^2\, e^{\kappa z_+} + 2k^2 \cosh(\kappa z_-) + \kappa_-^2\, e^{-\kappa z_+}\right], \tag{3.29}$$

where $z_+ = z + z' - h$, $z_- = |z - z'| - h$, $\gamma = -4\kappa k^2 \sinh \kappa h$, and $\kappa_\pm = \kappa \pm N_0^2/(2g)$.

The solution is obtained by convolving G_k with F_k (which is given in terms of the perturbation density ρ from (3.19)) to find the Q_k in (3.21), which are the Fourier coefficients for q in (3.18), which then can be transformed to find the pressure perturbation field p,

$$p(x,z) = \mathrm{Re}\left\{ -\frac{2}{l} e^{-N_0^2 z/2g} \sum_k e^{-ikx} \int_0^h dz'\, G_k(z,z') \int_0^l dx'\, f(x',z')\, e^{ikx'} \right\}, \tag{3.30}$$

where f, recall, is determined by ρ according to (3.19).

3.2 Numerical simulations and laboratory experiments

To test our approach and to explore its robustness, we apply it to density perturbation data for both numerically simulated and experimentally measured internal wave beams. The numerical simulations are described in section 3.2.1, while the laboratory tank system and synthetic schlieren measurements are described in section 3.2.2. Comparison of the density perturbation fields from the simulations and the synthetic schlieren measurements is made in section 3.2.3 in order to validate the application of our method to laboratory data.

3.2.1 Navier-Stokes numerical simulations

Our direct numerical simulations of the Navier-Stokes equations yield density, velocity, and pressure perturbation fields for a system with a driven internal wave beam. The energy flux computed from these fields will be compared to the values obtained by the approach that uses only density perturbation data, as described in section 3.1.2. The simulations use the CDP-2.4 code, which solves the Navier-Stokes equations in the Boussinesq approximation [28]. This finite-volume based solver implements a fractional-step time-marching scheme, with subgrid modeling deactivated. The code has been validated in previous laboratory and computational studies of internal waves [35, 40, 13, 72, 56].

The simulations are conducted in a two-dimensional domain with $x \in [-3.0, 3.0]$ m and $z \in [0, 0.63]$ m. Domain dimensions and parameters for

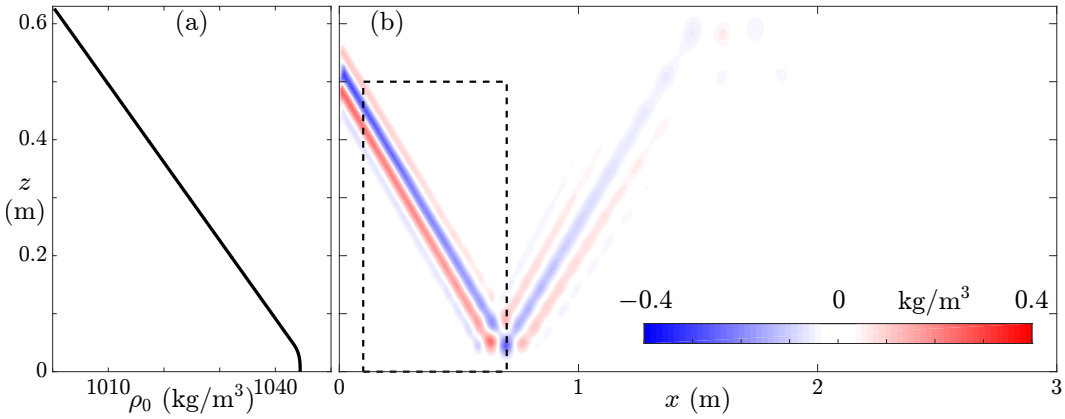

Figure 3.1: (a) The analytic density profile used for the simulations; the buoyancy frequency is constant, $N = 0.8533$ rad/s, except $N = 0$ in a layer about 0.04 m thick at the bottom. (b) Simulation results for the density perturbation field from the internal wave generated in the upper left corner. The simulation domain is a rectangular box that extends from -3 m to +3 m, while the laboratory schlieren measurements are made in a region that corresponds to the box bordered by dashed lines. In this snapshot, made at an instant after 11.75 periods of forcing, the internal wave beam has reached a steady state in the region of the schlieren measurements, but the flow is still evolving in the region to the right of the dashed box. (Fig. 1 from [4])

the simulation are selected for comparison with the experiment discussed in section 3.2.2. The simulation solves the following for the total density ρ_T, pressure p_T, and velocity $\boldsymbol{v}_T$:

$$\frac{\partial \boldsymbol{v}_T}{\partial t} + \boldsymbol{v}_T \cdot \nabla \boldsymbol{v}_T = -\frac{1}{\rho_{00}} \nabla p_T + \nu \nabla^2 \boldsymbol{v}_T - \frac{g\rho_T}{\rho_{00}} \hat{\boldsymbol{z}}, \tag{3.31}$$

$$\frac{\partial \rho_T}{\partial t} + \boldsymbol{v}_T \cdot \nabla \rho_T = \kappa \nabla^2 \rho_T, \nabla \cdot \boldsymbol{v}_T = 0, \tag{3.32}$$

where $\rho_{00} = 1000$ kg/m^3 (density of water), $\nu = 10^{-6}$ m^2/s (kinematic viscosity of water at 20^{o}C), and $\kappa = 2 \times 10^{-9}$ m^2/s (the diffusivity of NaCl in water). Initially the system is stationary with a linear density stratification with buoyancy frequency $N = 0.8533$ rad/s, except in the bottom 0.04 m where the density is constant (figure 1(a)). The boundary conditions are free-slip at the top and no-slip at the bottom. The left and right boundaries are periodic with Rayleigh damping, proportional to the velocity, implemented within 0.5 m of the left and right ends of the domain, preventing any advection through the boundary.

An internal wave beam is produced using a momentum source in $x \in [-0.01, 0.01]$ m and $z \in [0.43, 0.5825]$ m that imposes the velocity

$$\boldsymbol{v}_T = \omega A(z) \sin(\omega t - k_z z) \hat{\boldsymbol{x}}, \tag{3.33}$$

with an amplitude profile given by

$$A(z) = \exp(-(z - 0.50625)^2/0.22), \tag{3.34}$$

where the lengths are in meters, and $k_z = 82.45$ m^{-1}. A time step $\delta t = 0.0025$ s (5200 steps per period) is sufficient for temporal convergence. Spatial

convergence is obtained using a structured mesh with resolution $\delta x \approx 10^{-7}$ m near the boundaries, $\delta x \approx 10^{-4}$ m within the internal wave beam, and $\delta x \approx 10^{-2}$ m away from the active region. Changes in the velocity field are less than 1% when spatial and temporal resolutions are doubled.

A snapshot of the density perturbation field from the simulation is presented in figure 3.1(b). Only the right half of the domain is shown because the system is symmetric about $x = 0$ m. The internal wave beam is produced at $x = 0$ m at a height of about $z = 0.5$ m, and the reflection of the beam occurs at $(x, z) = (0.7, 0.04)$ m. The constant density layer in the bottom 0.04 m does not propagate waves because the forcing frequency is higher than the local buoyancy frequency. This snapshot is taken after 11.75 periods of forcing, which is sufficiently long for the beam to reach the bottom of the domain but not yet reach a steady state.

3.2.2 Experimental techniques

The intended application of the approach is for observed data either in the ocean or in a tank experiment. A tank-based experiment analogous to the simulation is performed where synthetic schlieren measurements are made to obtain the instantaneous density perturbation field.

The laboratory system for determining the density perturbation field by the synthetic schlieren method is diagrammed in figure 3.2(a): a density-stratified fluid is contained in a lucite tank that has interior dimensions of 4 m $\times$ 0.7 m $\times$ 0.15 m, and the apparatus for generating internal waves

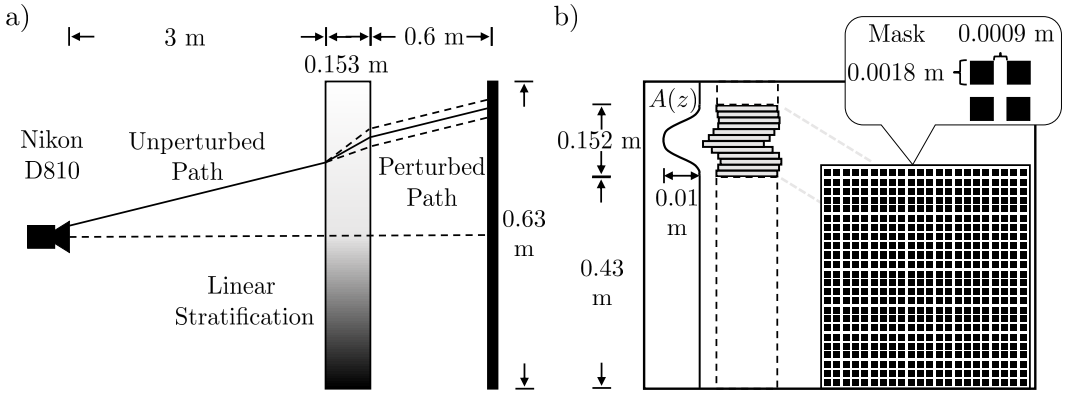

Figure 3.2: (a) A sketch of the experimental system. The camera observes, through the stratified fluid, a white screen located 0.6 m beyond the tank. The screen is covered by a mask (shown in (b)), and is back-lit by a panel of LEDs. Density perturbations caused by the internal wave beam change the fluid index of refraction, causing the mask to appear to move, and digital movies record this motion. (b) The internal wave generator has 12 plates that are driven by a camshaft, and each cam is an eccentric disk on a hexagonal rod that is rotated by a stepper motor. The disk eccentricity, $A(z)$, is a Gaussian profile. The mask covering the LED panel is a rectangular array of black squares, each 0.0018 m $\times$ 0.0018 m with 0.0009 m gaps in between. (Fig. 2 from [4])

(figure 3.2(b)) is 3 m from the end of the tank. The tank is filled slowly from the bottom, using the generalized double-bucket procedure of Hill [31], which uses two fluid reservoirs, one with pure water and the other with saturated salt water, to produce the desired fluid density profile. In our tank, the density increases linearly from 1000 kg/m^3 (pure water) at the top to a density of 1045 kg/m^3 (salt solution) at a height just 0.04 m above the bottom; below 0.04 m the density is approximately constant (see figure 3.1(a)). The constant density layer is added to lift the fluid away from optical distortions at the bottom of the tank. To measure the stratification, fluid samples are withdrawn from the tank at various heights and their densities are measured with an Anton-Parr density meter.

An internal wave beam is generated with a camshaft-driven wavemaker based on the design of Mercier et al. [48] (see figure 3.2(b)). A rotating camshaft drives a stack of 12 delrin plastic plates (cams) to produce a velocity profile approximating the one used in the simulations. The cams are 0.0762 m diameter circular disks that are offset from their centers by distances prescribed by equation (3.34). The hexagon drive shaft gives a phase difference of $\pi/3$ between consecutive disks. The wavemaker is driven at $(2\pi)/13$ rad/sec, which yields a beam with an angle of $\theta = 34.5^o$ with respect to the horizontal, based on the dispersion relation $\sin\theta = \omega/N$.

The density perturbation field resulting from the two-dimensional internal wave beam is observed using the synthetic schlieren method, which uses the linear relationship between the local density gradient and the index of

refraction of the density-stratified fluid [65, 12]. The distorted images of the mask's square grid pattern (cf. figure 3.2) are recorded with a camera on the opposite side, as in Sutherland et al. [66]. Calculation of the corresponding density perturbation field through integration, however, has proven to be challenging because the time-dependent image must have a large signal-to-noise ratio in order to obtain accurate density perturbation fields to implement the method described in section 3.1. As a result of this challenge, only a few investigations have actually calculated density perturbation fields from schlieren measurements [18, 68, 30, 33].

To allow us to accurately integrate the density-perturbation field, we achieve a large signal-to-noise ratio using a Nikon D810 camera with 7360 $\times$ 4912 pixels to image the pattern of black squares of the mask (see figure 3.2(b)). The camera is placed 3 m in front of the tank. The D810 camera has focus and mirror locks that reduce camera and focus jitter during closure of the mechanical shutter. The camera images a 0.86 m $\times$ 0.51 m region that starts 0.1 m to the right of the wavemaker and extends upward from the bottom of the tank. Images are taken at a frequency of 1 Hz, which corresponds to 13 images per wave period. There are 10 pixels across each black square in the image; in the quiescent system the image of a black square moves less than 0.1 pixel due to thermal variations and camera shake. In the most intense part of the internal wave beam the black squares are displaced typically by 6 pixels.

The positions of the individual black squares in the images are determined with subpixel accuracy using a particle tracking code that identifies

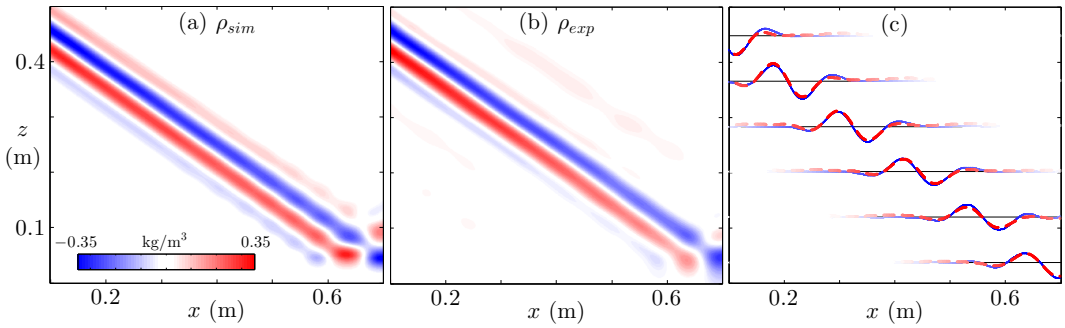

Figure 3.3: The instantaneous density perturbation field from (a) simulation and (b) experiment. (c) The synthetic schlieren density perturbation measurements (red dashed) agree well with the numerical simulation results (blue solid) at different heights in the tank. The horizontal black lines correspond to zero perturbation. The maximum amplitude of the perturbation is 0.36 kg/m^3. (Fig. 3 from [4])

centers of squares by a least-squares method [20]. To create the displacement values, reference positions of the squares are determined from a sequence of images obtained before the wavemaker is turned on. Then the displacement field of the squares is computed from the images in the digital movie, and the displacements are used to calculate perturbations of $\nabla\rho$. Through application of a partial-differential-equation solver that eliminates the rotational noise in the measurements, the density-gradient perturbations are used to calculate a density perturbation field [30]. While we performed the calculation independently, the density perturbation field can be computed from schlieren data using the software package DigiFlow [11].

3.2.3 Comparison between simulation and experiment

Care was taken to match the conditions of the experiment and simulation, but there are differences, particularly in the layers of nearly constant density at the top and bottom of the laboratory tank. The laboratory wavemaker forcing profile modeled by equation (3.34) was fit to the eccentricity profile used in the experiments, but the match was imperfect. However, the frequencies were accurately matched. Another minor difference between the simulation and experiment is that the free surface in the experiment falls and rises about 10^{-7} m, while the simulation compensates for the small periodic volume flux with a background flow that is at least five orders of magnitude smaller than the velocities in the beam. Finally, our comparisons between the simulation and experiment are made at an early enough time that the internal wave beam has not reflected off the far end of the tank.

The simulated density perturbation field matches well with the laboratory schlieren data obtained in the region corresponding to the black dashed box of figure 3.1, as can be seen by comparing figures 3.3(a) and (b). The amplitude of the experimentally measured density perturbation is 2% smaller than in the simulation. The experimental internal wave beam has a narrower band of large density perturbation, which is perhaps due to weaker realized forcing by the top and bottom plates of the wavemaker. Finally, the density perturbation below the reflection region differs from the experimental internal wave beam, which penetrates further into the bottom near-constant density layer.

The simulated and experimental density perturbation profiles at six heights are compared in figure 3.3(c). The rms difference (relative to the beam amplitude) between the simulated and measured density perturbation fields within the beam is about 9%, except near the bottom of the tank where the difference rises to as much as 30%. The large error in the constant density layer at the bottom boundary arises because, as aforementioned, the simulation uses an analytic density profile that closely but not exactly models the density profile near the bottom of the laboratory tank.

3.3 Results

Given the density perturbation fields from section 3.2.1, we obtain the instantaneous velocity, pressure, and energy flux using our method, and compare them to the simulated results in section 3.3.1. This verification of the method presented in section 3.1 uses the entire simulation domain, which satisfies the boundary conditions in equations (3.14) and (3.16). Then section 3.3.2 applies the method to laboratory schlieren measurements of the density perturbation field. These calculations are made in a subdomain of the simulations, but we show that with appropriate buffering of the laboratory data the results for the energy flux determined by the method agree well with direct Navier-Stokes simulations.

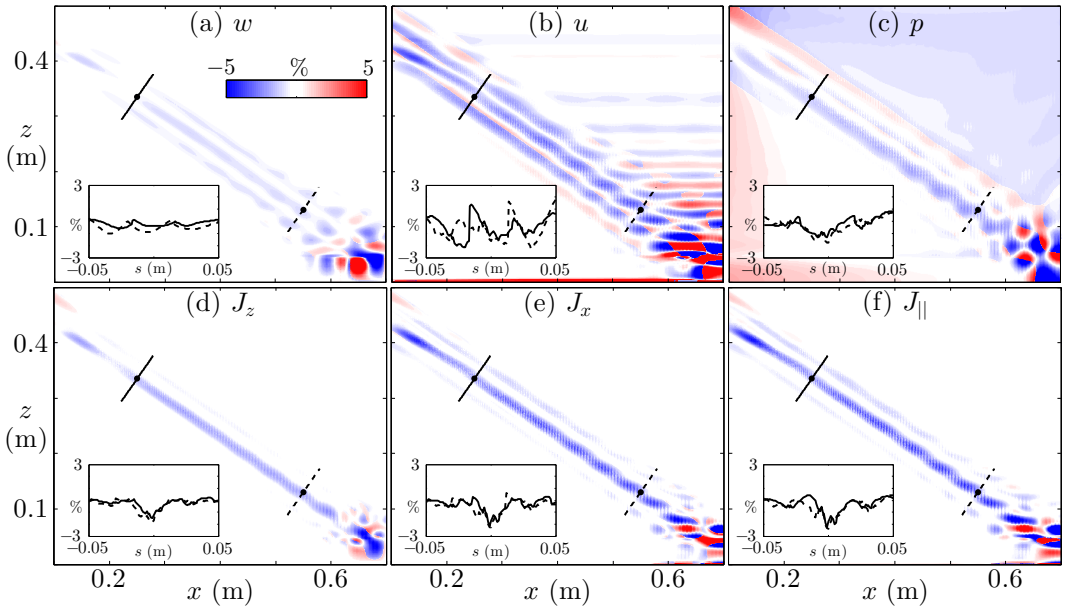

Figure 3.4: The percent difference (relative to the peak amplitude) of the instantaneous fields calculated solely from the simulation density perturbation field compared with the direct Navier-Stokes simulation values for w (a), u (b), p (c), J_z (d), J_x (e), and the energy flux component parallel to the beam, $J_{\parallel}$ (f). The insets show profiles in the beam towards the top-left (solid) and bottom-right (dashed) corners of the domain. Excluding the reflection region where the buoyancy frequency deviates, the difference is within 3% for all quantities. (Fig. 4 from [4])

3.3.1 Verification of the method by comparison with direct numerical simulations

The Green's function method for determining the instantaneous velocity perturbations, pressure perturbations, and energy flux from density perturbation data for internal waves is verified by comparison with results from the numerical simulations. As figure 3.4 shows, the fields w, u, and p calculated solely from simulation density perturbation data agree with the direct simulation values typically to within a few percent, and the results for the energy flux $\boldsymbol{J}$ agree with the simulations to within 1% throughout most of the domain, except in the thin constant density layer near the bottom. There the buoyancy frequency profile deviates from the uniform value of the rest of the domain. Note that all percent differences are relative to the peak amplitude. The analysis is performed on the internal wave field in the entire domain in figure 3.1 to satisfy the boundary conditions (3.14) and (3.16).

The vertical velocity component w in figure 3.4(a) is straightforwardly obtained from the time derivative of the density perturbation field (3.11). Throughout the domain the results closely match, and across the beam the rms percent difference (normalized by the peak amplitude) between the density-calculated and simulated values is 0.8%. The largest errors occur where the wave beam is generated and in the region where the beam reflects from the thin constant density layer at the bottom (cf. figure 3.1(b)). In the latter region the percent difference is as high as 11%.

The horizontal velocity component u is calculated by integrating the

incompressibility condition with the previously calculated w of (3.12). Taking initial integration points where the velocity is known to be zero or small, the normalized rms difference between u from the density-calculated method and from direct simulations is 2.2% across the internal wave beam. The amplitude-normalized percent difference is less than 2% throughout the beam but reaches errors as large as 26% at the constant density layer interface. However, because we assume the starting point has zero velocity, any error in our assumption that the starting point has zero velocity will propagate across the horizontal slice, as is evident to the right of the beam.

The first step in determining the pressure perturbation field from the density perturbation field is the calculation of the Fourier coefficients of $f(x, z)$ (3.20) for each horizontal slice of the domain. We find that 300 modes are sufficient for convergence for the high resolution simulation data with a small beam width relative to the domain width. The Fourier coefficients are then used in the Green's function calculation to obtain the pressure perturbation field p (cf. (3.30)). The normalized rms difference between this calculated p and the value of p direct from the simulations is 3% in the beam (figure 3.4(c)). Again the largest errors (11%) are in the regions of wave beam generation and reflection.

Finally, the energy flux is obtained by multiplying the calculated velocity and pressure perturbation fields. Figures 3.4(d) and (e) compare J_z and J_x obtained from the density perturbation field with the direct numerical simulations, respectively. The normalized rms difference in the vertical energy

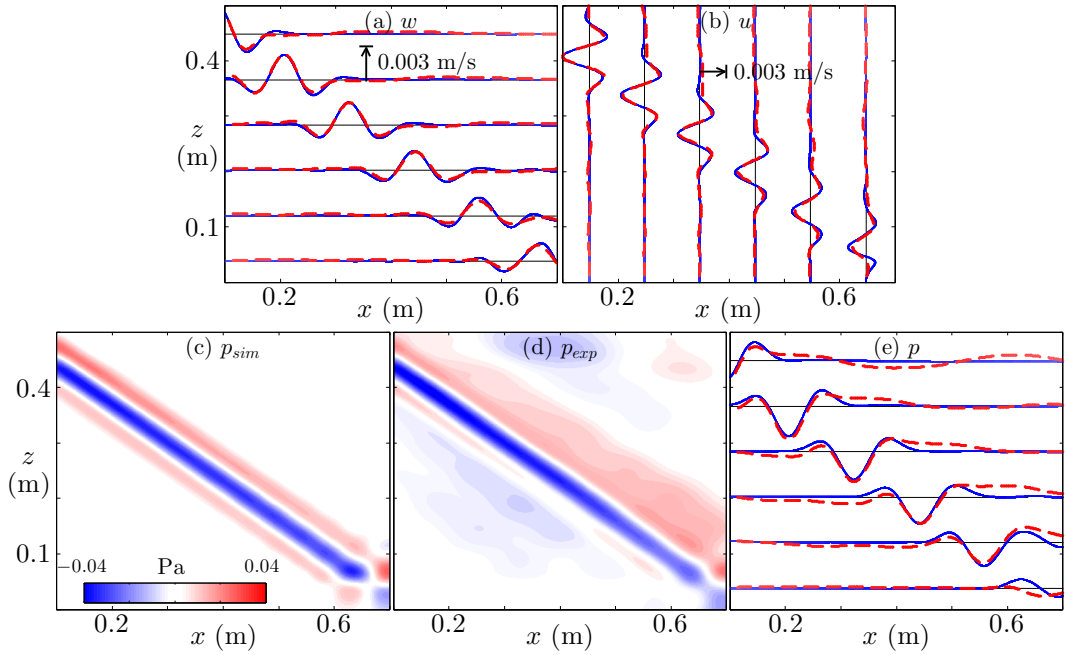

Figure 3.5: Experimental (red dashed) and simulation (blue solid) results at different heights are compared for w (a) and u (b). (c) The pressure perturbation field from the simulation. (d) p from the Green's function method applied to laboratory data. (e) A comparison of the results in (c) and (d) at different heights. (Fig. 5 from [4])

flux in the internal wave beam is 0.8%, which matches the precision of the vertical velocity calculation. The maximum difference in the flux magnitude occurs in the reflection region and is 4.5% (cf. figure 3.4(f)), which is lower than the individual components because the overestimate of the calculated vertical velocity is partially compensated by an underestimate of the pressure. Throughout most of the beam the normalized percent difference between our method and the direct Navier-Stokes simulation result for the energy flux is less than 1.0%. Because the calculation of the velocity and pressure tend to underestimate the actual values, the energy flux is also underestimated.

3.3.2 Application of the method to laboratory data

Having verified the method in the previous subsection, we now apply it to the experimental data presented in section 3.2.3. The data is obtained in the portion of the domain within the black dashed box in figure 3.1, but this subdomain does not satisfy the boundary conditions taken for the method. However, in appendix B.1 we present a procedure that accommodates data sets for subdomains that do not strictly satisfy the boundary conditions. For better comparisons between the simulated and experimental results, the simulation data in this subsection uses a lower data resolution, which is identical to that of the experiment. As mentioned in section 3.2.3, the measured and simulated density perturbation fields are not identical, but closely represent the same instant allowing the use of the simulated results for comparison of the velocity perturbation, pressure perturbation, and energy flux fields.

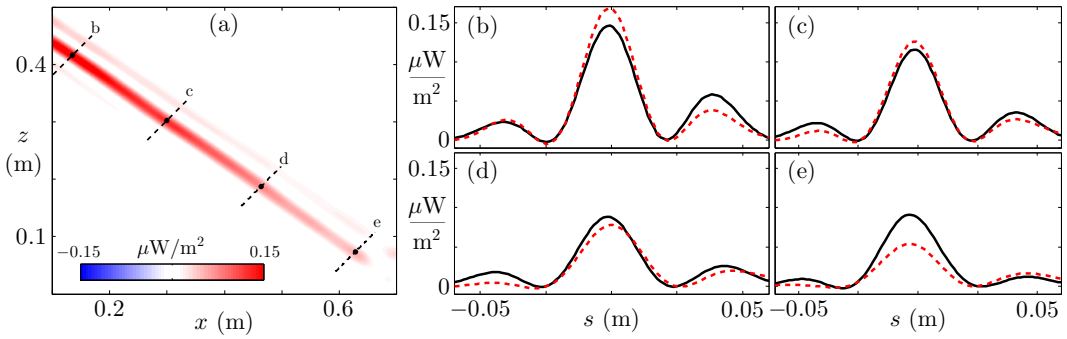

Figure 3.6: (a) The energy flux in the direction of the internal wave beam, obtained using the Green's function method on the experimental density perturbation data. (b)-(e) The energy flux in cross sections of the beam, computed from the Navier-Stokes simulations (black solid) and from the Green's function method on the laboratory measurements (red dashed). The agreement is very good in (c) and (d), but less so in regions where the simulations have less accurate representations of the laboratory system, that is, near the internal wave source (b) and near the unstratified the thin bottom layer (e). (Fig. 6 from [4])

The velocity components from the simulations and laboratory measurements are compared in figures 3.5(a) and (b). The camera was limited to 13 frames per period, but despite this large time step the results calculated from the lower-resolution simulation data for the time derivative of the density perturbation differ from the high-resolution results presented in section 3.3.1 by less than 1%. The vertical velocity profiles from the simulation and experiment in figure 3.5(a) have an average normalized rms difference of 8.1% in the beam. The horizontal velocity profiles in figure 3.5(b) have similar average normalized rms differences, 8.4%. The largest error, as much as 30%, occurs in the reflection region where the simulation and laboratory density stratification profiles differ.

Outside the beam the velocity field calculated from the experimental density perturbation field agrees well with the values direct from the simulations. However, outside the beam the pressure perturbation field p found by applying the Green's function method to the experimental data does not agree as well with the corresponding values from the numerical simulation, as figures 3.5(c) and (d) show. The differences between p from the simulation and the experiment result primarily from the differences in the lower mode Fourier components, because of error at larger length scales in the experimental density perturbation data (not shown). The resultant difference is evident in the plots of p at different heights in figure 3.5(e). The average normalized rms difference in p in the beam and for the full domain are comparable, 15.1% and 14.0%, respectively.

Despite the differences in p direct from the simulation and the Green's function calculation of the laboratory data, the energy flux obtained by the Green's function method differs from the simulation typically by only 6% (rms difference normalized by the flux amplitude), as figure 3.6 shows. The Green's function result for the flux outside of the beam does not have the artifacts present in the pressure field, because in those regions the velocity is close to zero. The agreement is not as good at the upper left (cf. figure 3.6(b)), where the laboratory internal wave generator is represented by an approximate model form in the Navier-Stokes simulations, and at the lower right where the beam reflects from a thin unstratified bottom layer, which is also only modeled approximately in the Navier-Stokes simulations (cf. figure 3.6(e)).

3.4 Conclusions

We have presented a Green's function method for calculating the instantaneous energy flux field $\boldsymbol{J} = p\boldsymbol{v}$ solely from the density perturbation field for linear internal waves in a density-stratified fluid with a uniform buoyancy frequency N. $\boldsymbol{J}$ is obtained from the density perturbation field through separate computations of p, u, and w: p using the Green's function expression of (3.30), w from the continuity equation (3.11), and u from incompressibility and knowledge of w from the previous calculation. The method was verified using numerical Navier-Stokes simulations of our laboratory experiment on internal waves generated in a tank with a linearly stratified density fluid. In most of the domain, w, u, p, and $\boldsymbol{J}$ calculated using the Green's function method solely from the density perturbation field from a Navier-Stokes simulation agree within a few percent with results obtained directly from the simulation. However, in regions near the wave generator and the unstratified bottom fluid layer, the results obtained directly from the simulations and from the Green's function method differ by as much as 5%.

The Green's function method was then applied to laboratory schlieren data. In order to match the boundary conditions in the derivation, (3.14) and (3.16), we used data buffers described in appendix B.1 because the observational window for the schlieren measurements did not span the entire tank. The density perturbation field determined from the schlieren data differs from the numerical simulation by about 11%, but a counterbalance of errors in the velocity and pressure fields led to energy flux values from the experiment that

agree with the numerical simulations to within 6%.

The Green's function method developed here was applied to internal waves in a linearly stratified fluid (uniform buoyancy frequency) and an analytic solution was found. However, the theory in section 3.1.1 applies to *any* stratification. Systems with nonlinear stratifications can be analyzed numerically with (3.13), and for some buoyancy frequency profiles $N(z)$ analytic solutions are possible, as is discussed in chapter 4.

While the method was applied here to a single internal wave beam, it also was found to work for a wave field where a parametric subharmonic instability produced wave energy at two new wavenumbers and frequencies; this would be difficult to treat by time-averaged methods. A modification of the present method could be made for systems with a known time-varying spatially uniform background flow, such as tidal flow. Another interesting extension would be to weakly three-dimensional density perturbation fields, such as those that occur near ocean ridges and in coastal waters.

To aid in the application of this method, a Matlab GUI has been developed, as described in appendix B.2. Implementation of the GUI requires the density perturbation field, the coordinates of the data, the time step size, and the buoyancy frequency (which is assumed to be constant). If a data set does not satisfy the boundary conditions assumed in our analysis, the GUI can implement the buffering technique used on our data and discussed in appendix B.1. The GUI includes an operations manual and also a tutorial which recalculates the numerical results from section 3.3.2.

Chapter 4

The energy flux from the density perturbation field for non-uniform N

This chapter, at the time of this writing, is heavily based on a manuscript [41] which has been submitted to The Journal of Fluid Mechanics. The Navier-Stokes simulation results and the finite difference method were obtained by Michael Allshouse. In chapter 3 a Green's function method was used to calculate the instantaneous energy flux field from a density perturbation field [4] for a fluid with constant buoyancy frequency,

$$N(z) = \sqrt{\frac{-g}{\rho_0}\frac{\partial \rho}{\partial z}}, \tag{4.1}$$

but in the oceans N varies significantly with depth, as figure 4.1 illustrates with data from two locations in the North Atlantic.

Recognizing the strength of the Green's function method, we extend that method to accommodate linear N and tanh N^2 profiles. These two profiles are selected due to their mathematical properties and their presence in ocean stratifications. The tanh N^2 profile is often a good approximation in the ocean when two nearly constant buoyancy-frequency zones are separated by a pycnocline, as figure 4.1(a) illustrates. The linear N profile can occur in the ocean when there is no strong pycnocline, and the buoyancy frequency near

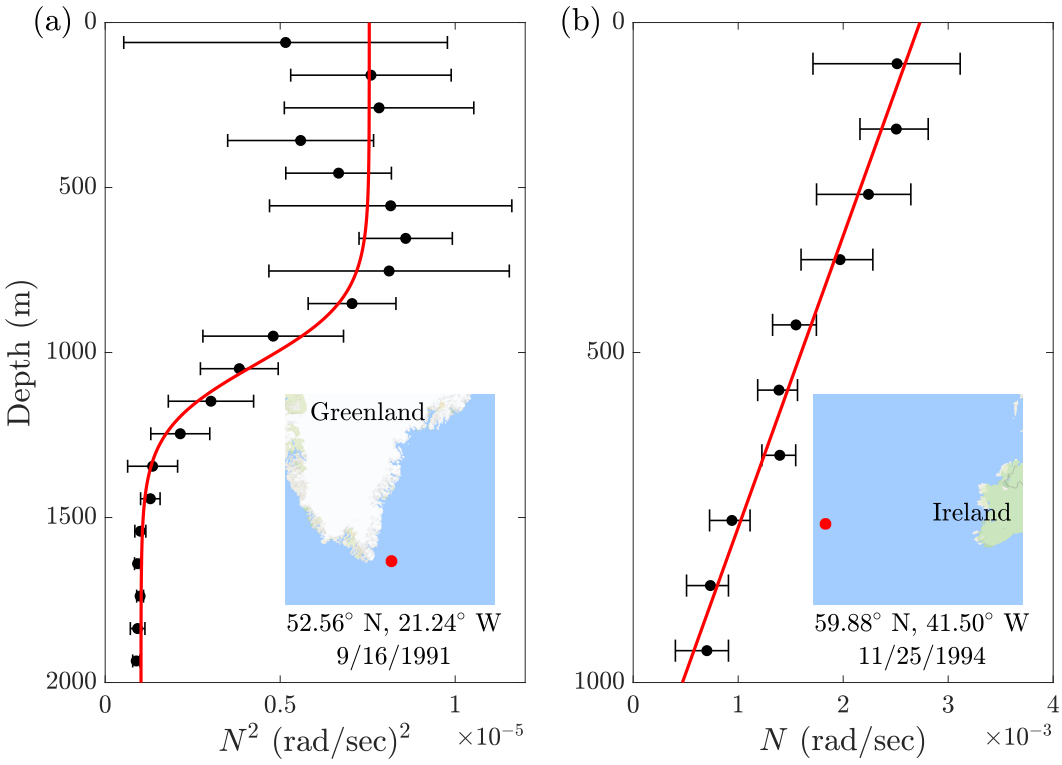

Figure 4.1: Two buoyancy frequency profiles from a World Ocean Circulation Experiment data set: (a) A measured buoyancy frequency squared profile (black dots) fit to a tanh profile (red). (b) A measured buoyancy frequency profile (black dots) fit to a linear profile (red). The insets show regions 1000 km $\times$ 1000 km that contain the locations (red dots) where the measurements were made. The mean buoyancy frequency (squared for (a)) of bins of stratification measurements is plotted as a function of depth (black dots) with error bars representing two standard deviations from the mean.

the surface decays to a nearly constant value in the depth, as illustrated in figure 4.1(b).

However, because many buoyancy frequency profiles cannot be adequately approximated by either a linear N or a tanh N^2 profile as in figure 4.1, the general $N(z)$ case must be treated separately. To account for this, we present a numerical method for computing the instantaneous energy flux field solely from a density perturbation field that can have an *arbitrary* $N(z)$ profile.

The present work provides a tool for laboratory experiments and field measurements: the calculation of the instantaneous energy flux field from density perturbation data. The tool can be applied to ocean density perturbation space-time data when such data becomes available. The tool, comprised of methods presented here and in Allshouse et al. [4], provides the *instantaneous* rather than time-averaged energy flux field. Thus the resultant energy flux and integrated far-field power include all spectral components, while previous methods provided only the global conversion rates or monochromatic results.

This chapter is organized as follows. An outline of our method for obtaining the energy flux from the density perturbation field in a tanh N^2 and linear N stratification is presented in section 4.1. This method is then verified with numerical simulations in section 4.2. A finite difference method for calculating the energy flux for an arbitrary buoyancy frequency profile is presented in section 4.3, and is applied to an ocean-inspired stratification. Lastly, conclusions and potential applications of this work are presented in

section 4.4.

4.1 Theoretical development

As this work builds off the theoretical foundation presented in chapter 3 and Allshouse et al. [4], we present the general equations in section 4.1.1. These equations provide the velocity perturbation field as a function of the density perturbation, and a functional relationship between the density and pressure perturbation fields is established. For an analytic tanh N^2 and linear N, we calculate the Green's function in section 4.1.2 and section 4.1.3, respectively.

4.1.1 Generalities

Our goal of obtaining the energy flux (1.39) from the density perturbation field alone requires calculating the pressure perturbation and components of the velocity perturbation from the density perturbation field. The details of these calculations were given in Allshouse et al. [4] for a uniform N profile, but here we present a condensed version of the pressure perturbation calculation, as needed for the calculations for the tanh N^2 and linear N profiles.

As before, we begin with the linearized Euler equations for perturbation about a hydrostatic background, and they are shown here again for readability:

$$\frac{\partial u}{\partial t} = -\frac{1}{\rho_0}\frac{\partial p}{\partial x}\,, \qquad \frac{\partial w}{\partial t} = -\frac{1}{\rho_0}\frac{\partial p}{\partial z} - \frac{\rho}{\rho_0}g\,, \tag{4.2}$$

$$\frac{\partial \rho}{\partial t} = \frac{N^2\,\rho_0}{g}w\,, \qquad \frac{\partial u}{\partial x} + \frac{\partial w}{\partial z} = 0\,, \tag{4.3}$$

where u and v are the horizontal and vertical components of the velocity

perturbation, respectively, p is the pressure perturbation, ρ is the density perturbation, ρ_0 is the hydrostatic background density profile, and N is the buoyancy frequency. By manipulating (4.2) and (4.3) we obtain an equation for the pressure perturbation in terms of the density perturbation,

$$\frac{\partial^2 p}{\partial x^2} + \frac{\partial^2 p}{\partial z^2} + \frac{N^2}{g}\frac{\partial p}{\partial z} = -N^2\rho - g\frac{\partial \rho}{\partial z}\,. \tag{4.4}$$

First, we solve this equation for p assuming we have the measured ρ.

Equation (4.4) is brought into a convenient form by first applying the following transformation:

$$p(x,z) = q(x,z)\,T(z) \tag{4.5}$$

where

$$T(z) = \exp\left[-\frac{1}{2g}\int^z dz' N^2(z')\right] \tag{4.6}$$

and then Fourier expanding in x, yielding

$$\frac{d^2Q}{dz^2} - \left(k^2 + \frac{N}{g}\frac{dN}{dz} + \frac{N^4}{4\,g^2}\right)Q = -F. \tag{4.7}$$

Here $F(z;k)$ and $Q(z;k)$ denote the Fourier components of

$$f(x,z) = \frac{1}{T(z)}\left(N^2\rho + g\frac{\partial \rho}{\partial z}\right) \tag{4.8}$$

and $q(x,z)$, respectively.

We solve (4.7) for Q given F by obtaining the Green's function for the Fourier components, which satisfies

$$\frac{d^2}{dz^2}G(z,z';k) - \left(k^2 + \frac{N}{g}\frac{dN}{dz} + \frac{N^4}{4g^2}\right)G(z,z';k) = 0, \quad z \neq z'\,, \tag{4.9}$$

with a no-flux condition in the z direction at the top and bottom of the domain,

$$\left(\frac{dG}{dz} - \frac{N^2}{2g}G\right)\Big|_{z=0,\,h} = 0\,, \tag{4.10}$$

and the Green's function matching conditions,

$$G^+(z') = G^-(z') \tag{4.11}$$

$$\frac{dG^+}{dz}(z') = \frac{dG^-}{dz}(z') + 1\,. \tag{4.12}$$

Thus, given profiles for the buoyancy frequency N and source term f, the pressure perturbation is given by the following expression:

$$p(x,z) = \mathrm{Re}\left\{ -\frac{2}{l}\,T(z)\sum_k e^{-ikx}\int_0^h dz'\,G(z,z';k)\int_0^l dx'\,f(x',z')\,e^{ikx'}\right\}, \tag{4.13}$$

where $k = 2\pi n/l$, l is the width of the system, and n is a positive integer.

Next, we obtain the components of the velocity perturbation. The vertical component follows by inverting the first equation of (4.3) yielding,

$$w = \frac{g}{N^2\,\rho_0}\frac{\partial \rho}{\partial t}, \tag{4.14}$$

and the horizontal component is obtained by using the vertical velocity perturbation (4.14) and the incompressibility condition, the second equation of (4.3), which gives the differential equation

$$\frac{\partial u}{\partial x} = -\frac{\partial}{\partial z}\left(\frac{g}{N^2\rho_0}\frac{\partial \rho}{\partial t}\right). \tag{4.15}$$

None of these calculations depend on the particular form of the buoyancy frequency profile, so it is possible to perform all the necessary expressions for calculating the energy flux from ρ alone in a general stratification.

To calculate analytically the Green's function for (4.9), it is necessary that the functional form of the buoyancy frequency profile be specified. Chapter 3 [4] investigates the particular case where the buoyancy frequency is constant resulting in a Green's function that is exponential. In section 4.1.2 we present the calculations for obtaining the pressure perturbation for the tanh N^2 profile, and in section 4.1.3 we present the analogous calculation for the linear N profile.

4.1.2 The tanh profile

The buoyancy frequency profile we assume in this section is given by

$$N^2(z) = \frac{N_1^2 + N_2^2}{2} + \frac{N_2^2 - N_1^2}{2} \tanh\big(\alpha(z - z_t)\big) \tag{4.16}$$

$$\equiv \eta_+ + \eta_- \tanh\big(\alpha(z - z_t)\big), \tag{4.17}$$

because this gives a convenient form for $N\,dN/dz$. Here α controls the transition width between the two buoyancy frequency values N_1 and N_2, and z_t is the midpoint of the transition. Note, for large α (4.17) approximates a two-layer N^2 profile, which we will investigate in section 4.2.2. We assume that $N^4/4g^2$ in (4.9) is negligible. For low mode numbers, outside of the transition region, k^2 ($\sim 10^0 - 10^1$ m^{-2}) is much larger than $N^4/4g^2$ ($\sim 10^{-2}$ m^{-2}), and near the transition region k^2 is roughly the same order as $(N/g)(dN/dz)$. For larger mode numbers k^2 is the dominant term. Thus for simplicity we keep k^2 and $(N/g)(dN/dz)$ and drop $N^4/4g^2$ for all modes. Upon substituting the

stratification of (4.17), the Green's function equation, (4.9) becomes

$$\frac{\partial^2}{\partial z^2}G(z,z';k) - \left(k^2 + \frac{\alpha\,\eta_-}{2\,g}\,\mathrm{sech}^2(\alpha(z-z_t))\right)G(z,z';k) = 0, \quad z \neq z'\,. \tag{4.18}$$

Equation (4.18) is of the form of a well-studied time-independent Schrödinger equation (e.g. [17, 58, 44]).

With the dimensionless coordinate transformation

$$z = z_t + \frac{1}{\alpha}\tanh^{-1} y, \tag{4.19}$$

equation (4.18) becomes

$$(1-y^2)\frac{d^2\bar{G}}{dy^2} - 2\,y\frac{d\bar{G}}{dy} + \left(\nu(\nu+1) - \frac{\mu^2}{1-y^2}\right)\bar{G} = 0, \quad y \neq y'\,, \tag{4.20}$$

where the dimensionless Green's function $\bar{G}$ is given by

$$G(z(y)) = \frac{1}{\alpha}\bar{G}(y) \tag{4.21}$$

and the parameters ν and μ are given by

$$\nu_\pm = -\frac{1}{2} \pm \frac{1}{2}\sqrt{1 - \frac{2\,\eta_-}{\alpha\,g}}\,, \qquad \mu = \frac{k}{\alpha}\,. \tag{4.22}$$

Thus the transformation takes (4.18) into the associated Legendre equation (4.20), which has the two linearly independent solutions $P^\mu_\nu(y)$ and $Q^\mu_\nu(y)$, the associated Legendre functions of the first and second kind, respectively. Then, solving (4.20) with the boundary conditions (4.10) and the matching conditions (4.11) and (4.12) gives the Green's function,

$$\bar{G}(y,y') = \frac{1}{D\,W}\begin{cases} \left(\Phi_2 P^\mu_\nu(y') + \Pi_2 Q^\mu_\nu(y')\right)\left(\Phi_1 P^\mu_\nu(y) + \Pi_1 Q^\mu_\nu(y)\right), & y < y' \\ \left(\Phi_1 P^\mu_\nu(y') + \Pi_1 Q^\mu_\nu(y')\right)\left(\Phi_2 P^\mu_\nu(y) + \Pi_2 Q^\mu_\nu(y)\right), & y > y'\,. \end{cases} \tag{4.23}$$

Here

$$D = -\begin{vmatrix} \Pi_1 & \Pi_2 \\ \Phi_1 & \Phi_2 \end{vmatrix}, \qquad W = 2^{2\mu}\frac{\Gamma(\frac{\nu+\mu+2}{2})\Gamma(\frac{\nu+\mu+1}{2})}{\Gamma(\frac{\nu-\mu+2}{2})\Gamma(\frac{\nu-\mu+1}{2})}, \tag{4.24}$$

$$\Pi_{1,2} = \frac{dP_\nu^\mu(y_{0,h})}{dy} - \frac{N_{1,2}^2}{2\,g\,(1-y_{0,h}^2)}P_\nu^\mu(y_{0,h}), \tag{4.25}$$

$$\Phi_{1,2} = -\frac{dQ_\nu^\mu(y_{0,h})}{dy} + \frac{N_{1,2}^2}{2\,g\,(1-y_{0,h}^2)}Q_\nu^\mu(y_{0,h}). \tag{4.26}$$

Note, the transformation factor $T(z)$ for this case is given by

$$T(z) = \left\{\frac{\cosh[\alpha(z_0-z_t)]}{\cosh[\alpha(z-z_t)]}\right\}^{\eta_-/(2\,\alpha\,g)} \exp\left[\frac{\eta_+(z_0-z)}{2\,g}\right]. \tag{4.27}$$

For further information on the numerical calculation of the Green's function see appendix D.

4.1.3 The linear profile

The calculations for the linear N profile are similar to those of section 4.1.2, so we only highlight the important differences. The linear profile for the buoyancy frequency is given by

$$N(z) = \frac{dN}{dz}\cdot(z-z_t) \equiv N'\cdot(z-z_t), \tag{4.28}$$

where z_t is now the location where the buoyancy frequency becomes zero. We again neglect $N^4/4g^2$ ($\sim 10^{-2}$ m^{-2}) in comparison to k^2 and $(N/g)(dN/dz)$ ($\sim n^2$ and ~ 1 m^{-2}, respectively) as we insert (4.28) into (4.9). For the linear N profile, instead of (4.18) we obtain

$$\frac{\partial^2}{\partial z^2}G(z,z';k) - \left(k^2 + (N')^2\frac{(z-z_t)}{g}\right)G(z,z';k) = 0, \quad z \neq z'. \tag{4.29}$$

With the coordinate transformation

$$z = z_t - g\,k^2(N')^{-2} + g^{1/3}(N')^{-2/3}\,y\,, \tag{4.30}$$

where once again y is a dimensionless coordinate variable, equation (4.29) becomes

$$\frac{d^2}{dy^2}\bar{G}(y) - y\,\bar{G}(y) = 0, \quad y \neq y'\,, \tag{4.31}$$

which is the Airy equation with the two independent solutions $Ai(y)$ and $Bi(y)$, the Airy functions of the first and second kind, respectively. Then, the dimensionless Green's function is given by

$$\bar{G}(y,y') = \frac{\pi}{D}\begin{cases}\Big(\beta_2 Ai(y') + \alpha_2 Bi(y')\Big)\Big(\beta_1 Ai(y) + \alpha_1 Bi(y)\Big), & y < y' \\ \Big(\beta_1 Ai(y') + \alpha_1 Bi(y')\Big)\Big(\beta_2 Ai(y) + \alpha_2 Bi(y)\Big), & y > y'\,,\end{cases} \tag{4.32}$$

which when given dimensions becomes

$$G(z(y)) = g^{1/3}(N')^{-2/3}\bar{G}(y). \tag{4.33}$$

Here

$$D = -\begin{vmatrix}\alpha_1 & \alpha_2 \\ \beta_1 & \beta_2\end{vmatrix}\,, \tag{4.34}$$

$$\alpha_{1,2} = \frac{dAi(y_{0,h})}{dy} - \frac{1}{2}\,g^{-2/3}(N')^{4/3}(z_{0,h} - z_t)^2 Ai(y_{0,h})\,, \tag{4.35}$$

$$\beta_{1,2} = -\frac{dBi(y_{0,h})}{dy} + \frac{1}{2}\,g^{-2/3}(N')^{4/3}(z_{0,h} - z_t)^2 Bi(y_{0,h})\,, \tag{4.36}$$

where z_0 and z_h are the coordinates of the bottom and top of the domain, respectively, and y_0 and y_h are the corresponding transformed coordinates. The transformation factor $T(z)$ in this case is given by

$$T(z) = \exp\left\{ \frac{(N')^3}{6\,g} \left[(z_0 - z_t)^3 - (z - z_t)^3 \right] \right\}. \tag{4.37}$$

4.2 Analysis verification

To verify the Green's function analysis in section 4.1, we compare those predictions with results for the energy flux obtained from direct numerical simulations of the Navier-Stokes equations. The simulations are described in section 4.2.1. The simulated velocity perturbation, pressure perturbation, and energy flux fields of internal waves in a stratified fluid are compared with the predictions from the analyses for a tanh N^2 profile in section 4.2.2 and for a linear N profile in section 4.2.3.

4.2.1 Simulation of the density perturbation field

To verify the Green's function method, we perform direct numerical simulations of the Navier-Stokes equations in the Boussinesq approximation. These simulations provide the density perturbation field needed to calculate the velocity perturbation, pressure perturbation, and energy flux fields. The simulations use the CDP-2.4 algorithm, which is a finite volume solver that implements a fractional-step time-marching scheme [28, 47]. This code has previously been used to simulate internal waves and has been validated with experiments [35, 40, 13, 72, 56, 4].

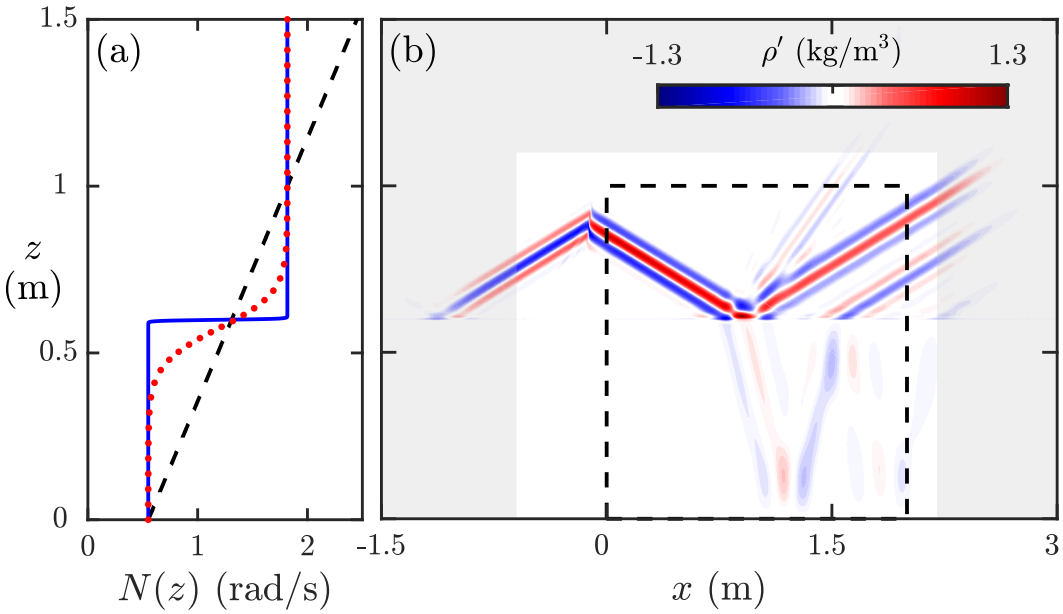

Figure 4.2: (a) The N profile of a broad transition tanh N^2 (dotted red curve) and a narrow transition tanh N^2 profile (solid blue curve). The dashed black line is a linear N profile. (b) The simulation domain and density perturbation field for the narrow transition tanh N^2 internal wave field. Rayleigh damping is applied in the gray region of the field. The sub domain used for analysis is bound with a black dashed line.

Our two-dimensional simulations span the domain $x \in [-1.5, 3]$ m and $z \in [0, 1.5]$ m. The simulation solves for the total density ρ_T, pressure p_T, and velocity $\boldsymbol{v}_T$:

$$\frac{\partial \boldsymbol{v}_T}{\partial t} + \boldsymbol{v}_T \cdot \nabla \boldsymbol{v}_T = -\frac{1}{\rho_{00}} \nabla p_T + \nu_w \nabla^2 \boldsymbol{v}_T - \frac{g\rho_T}{\rho_{00}} \hat{\boldsymbol{z}}, \tag{4.38}$$

$$\frac{\partial \rho_T}{\partial t} + \boldsymbol{v}_T \cdot \nabla \rho_T = \kappa_s \nabla^2 \rho_T, \nabla \cdot \boldsymbol{v}_T = 0, \tag{4.39}$$

where $\rho_{00} = 1000$ kg/m^3 (density of water), $\nu_w = 10^{-6}$ m^2/s (kinematic viscosity of water at 20^{o}C), and $\kappa_s = 2 \times 10^{-9}$ m^2/s (the diffusivity of NaCl in water). The system is initially at rest and the prescribed density field is unperturbed. The initial density field is analytically derived from the buoyancy frequency profiles presented in figure 4.2(a). The boundary conditions at the bottom and top are no slip and free slip, respectively. The left and right boundaries are set to be periodic; however, Rayleigh damping is used along the perimeter of the domain (gray region in figure 4.2(b)), thus forcing the velocity to be negligible at the left and right boundary.

The internal wave beam is produced by using a momentum source that forms a rectangle with height 0.15 m and width 0.04 m, centered at $(-0.02, 0.8)$ m and rotated to match the internal wave beam angle corresponding to the buoyancy frequency at $z = 0.8$ m. The wave beam velocity imposed is

$$\boldsymbol{v}_T = \omega A(z') \sin(\omega t - k_z z') \hat{\boldsymbol{x}'}, \tag{4.40}$$

with an amplitude profile given by

$$A(z') = \exp(-(z')^2/0.0022), \tag{4.41}$$

where the lengths are in meters, the rotated coordinates x' and z' correspond to the beam tangent and normal coordinates centered at $\boldsymbol{x} = (-0.02, 0.8)$ m, respectively, $\omega = 2\pi/13$ rad/sec and $k_z = 8245$ m^{-1}. A time step size $\delta t = 0.0025$ s (5200 steps per period) is sufficient for temporal convergence. Spatial convergence is obtained using an unstructured mesh with resolution $\delta x \approx 0.0014$ m inside the region $x \in [-0.8, 1.80]$ m, $y \in [0.5, 1.1]$ m. This high resolution region contains the beam generation, the density gradient transition for the tanh N^2 profiles, and generation of any additional beams. The resolution outside of this region grows to $\delta x \approx 0.0025$ m near the boundaries. Changes in the velocity field are less than 1% when spatial and temporal resolutions are doubled.

The density perturbation field for the case where we have a rapid change in buoyancy frequency (blue line in figure 4.2(a)) is presented in figure 4.2(b). The internal wave beam is generated at $(-0.02, 0.8)$ m and produces a beam propagating to the right that is the focus of our studies and a beam propagating to the left which is damped out by the Rayleigh damping. The beam propagating down to the right reaches the interface at $z = 0.6$ m at which point three beams are produced: a reflected beam to the top right at the same angle to the horizontal as the incoming beam, a transmitted beam to the bottom right that has a different angle, and a reflected second harmonic beam at approximately twice the incoming angle. This particular snapshot is shown after 23.06 periods of forcing, which is sufficient for the beam in the region of interest to reach steady state.

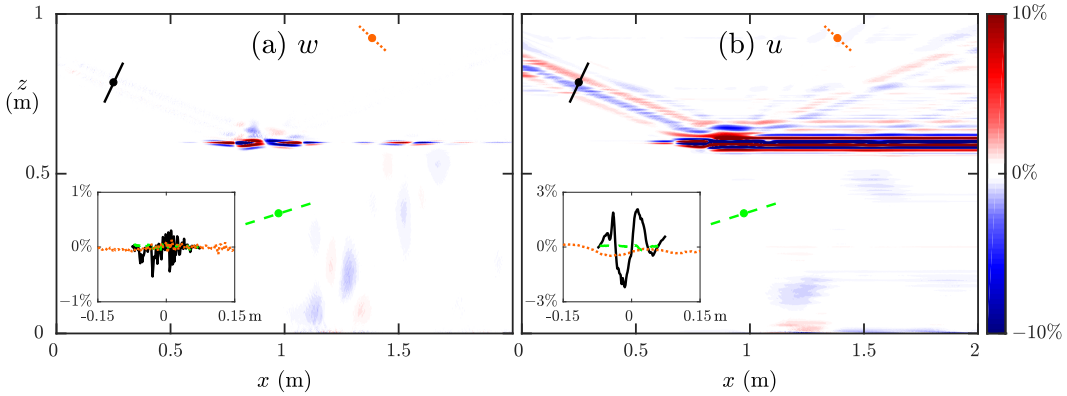

Figure 4.3: The beam-normalized percent difference between the density-perturbation-based method and the simulation for (a) w and (b) u. The insets show the percent difference across the beam for three transects: the incoming beam (solid black), the transmitted beam (dashed green), and the second harmonic beam (dotted orange).

4.2.2 Tanh N^2 profile analysis verification

The vertical (4.14) and horizontal (4.15) components of the velocity and the pressure perturbation calculated from the density perturbation using the Green's function (4.23) for the tanh N^2 profile are verified by comparison with the direct numerical simulations described in section 4.2.1. For large α the tanh N^2 profile can be approximated as a two-layer N system, as illustrated in figure 4.2(a), where $\alpha = 4$, corresponding to a transition thickness of 0.01 m for a 95% change in N^2; this is at least an order of magnitude smaller than the the beam width and domain height. Henceforth the large α case is called the "narrow transition" tanh N^2 profile.

The difference between the density-perturbation-based velocity perturbation and the simulated velocity perturbation for the narrow transition tanh

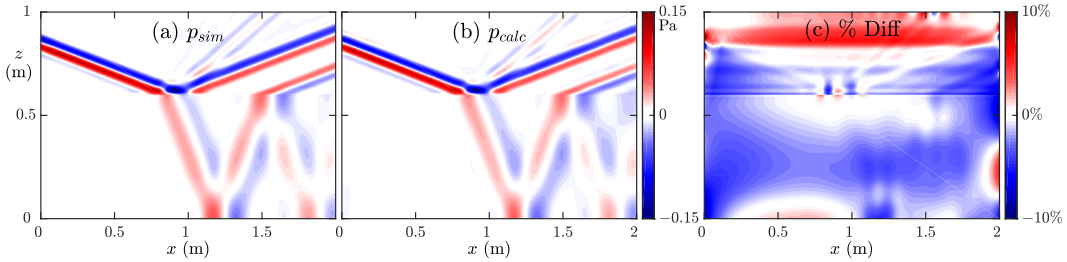

Figure 4.4: The pressure perturbation field from (a) the direct numerical simulation and (b) the Green's function calculation from the density perturbation. (c) The beam-normalized percent difference between the two pressure fields from the two methods.

N^2 profile are presented in figure 4.3; in most of the domain, the difference is less than 3% (with respect to the beam amplitude), except in the transition region at $z = 0.6$ m where there is a significant amount of nonlinearity. Because the horizontal velocity perturbation is found by solving an ODE on constant z levels (4.15), the patch of large vertical velocity perturbation error is propagated horizontally from the reflection site; thus the region of error is larger for u. Despite this nonlinearity, the error is small in most of the domain.

Next we investigate how well the Green's function method calculates the pressure perturbation field from the density perturbation field. Figure 4.4(a) shows the simulated pressure perturbation field, and figure 4.4(b) shows the pressure perturbation calculated using the Green's function method. Despite the nonlinearities in the narrow transition layer, the Green's function method, which is based on the linear equations, yields accurate estimates of the pressure perturbation for the reflected, transmitted, and second harmonic beams, as figure 4.4(b) illustrates. The beam-normalized percent difference between

the calculated and simulated pressure perturbation fields is presented in figure 4.4(c). The calculation is accurate to within 5% over most of the domain, and to better than 10% everywhere except within 0.02 m of where the beam enters the domain. Near the top of the domain, the Green's function method overestimates the pressure perturbation by $4-6\%$, which causes some distortion in the second harmonic, as can be seen around (1.25, 0.8) m in figures 4.4(a) and 4.4(b). The Green's function method underestimates the pressure perturbation in the center of the domain, but the error is less than 5%.

Finally, we use the calculated velocity and pressure perturbation fields to compare the energy flux $\boldsymbol{J}$ directly from the numerical simulations with the flux computed from the Green's function analysis. The magnitude of the energy flux from the simulations is presented for the narrow transition tanh N^2 profile in figures 4.5(a). For the narrow transition region case the energy flux for the reflected beam is higher than for the transmitted beam and an order of magnitude greater than in the second harmonic. The beam-normalized percent difference of the horizontal and vertical energy flux are presented in figures 4.5(b) and (c), respectively. Outside of the immediate vicinity of the interface region at $z = 0.6$ m the percent difference is less than 3%. The accumulated error from multiplying the calculated velocity and pressure perturbation to obtain the flux components is large at the narrow transition interface as a consequence of error in the horizontal velocity perturbation, which is compensated to some extent by a more accurate pressure perturbation cal-

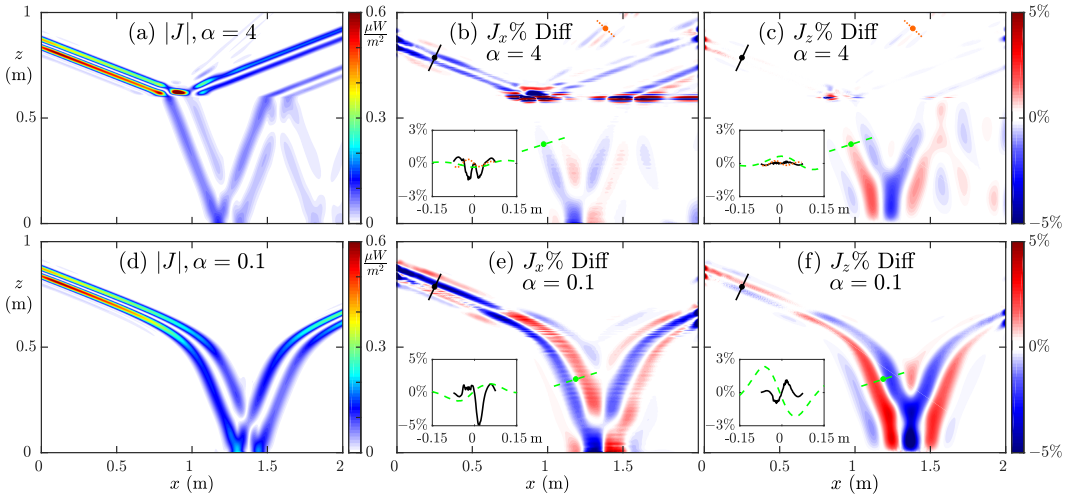

Figure 4.5: The energy flux magnitude computed in direct numerical simulations for (a) narrow ($\alpha = 4$) and (d) broad transition ($\alpha = 0.1$) tanh N^2 profile. The beam-normalized percent difference between the x-component of the energy flux from the simulations and from the Green's function method is shown in (b) and (e), respectively, for the narrow and broad transition regions, and corresponding results for the z-component of the energy flux are in (c) and (f). For each case an inset shows the difference between the simulations and Green's function methods is less than 5% for most of the domain; the insets in each panel show the difference along two or three beam transects.

culation at the interface; the error is smaller for J_z than for J_x. In the lower half of the domain the magnitude of the energy flux is underestimated due to underestimation of the pressure perturbation. The insets show that the error along three beam transects is mostly smaller than 3% for the narrow transition simulation.

We also simulate a tanh N^2 profile with a broader transition thickness layer of 0.31 m ($\alpha = 0.1$). We omit the comparison of the velocity and pressure perturbations for brevity and instead examine the energy fluxes, as shown in figure 4.5. The energy flux field for the broader tanh N^2 profile is presented in figure 4.5(d). The internal wave beam passes through the broad transition without reflection because there are no rapid changes in buoyancy frequency. This smooth transition reduces the nonlinearities so there are significantly smaller errors in the velocity perturbation field and thus the energy flux field as compared to the narrow transition tanh N^2. The magnitude of the energy flux decreases as the beam widens in the bottom of the domain and then increases again as the beam narrows after reflection. Beam-normalized percent differences are presented for the horizontal and vertical energy flux in figures 4.5(e) and (f), respectively. There is a change of overestimating the energy flux in the top of the domain to underestimating the energy flux in the bottom of the domain. This is most clearly seen at (0.7,0.7) m where the bands of constant phase change from red to blue and vice versa. This change is due to errors in the pressure perturbation. The two insets show that within the beam the percent difference is consistently less than 5%.

Figures 4.5(a)-(c) demonstrate that our method can handle rapid changes N^2, while the broad N^2 transition thickness in figures 4.5(d)-(f) is more representative of ocean stratifications. Figure 4.5(d) shows the energy flux amplitudes and reveals that the broadening of the transition layer eliminates the reflected and second harmonic beams. Further, the error in the broad transition region in figures 4.5(e)-(f) is much smaller than in the narrow transition region figures 4.5(b)-(c). The errors of the energy flux calculation for the two tanh N^2 profiles are less than 5% except in the narrow transition region (cf. insets of figure 4.5).

4.2.3 Linear profile analysis verification

To verify that the theory for the linear N profile of section 4.1.3 is valid, we perform simulations analogous to those in section 4.2.2. The energy flux field in figure 4.6(a) demonstrates that the internal wave beam bends more gradually for the linear N profile (figure 4.6(a)) as compared to the tanh N^2 profiles discussed in section 4.2.2 (figure 4.5(a) and (d)). This slower change is due to the smaller gradient of the buoyancy frequency for the linear N profile. Again, because there are no rapid changes in N there are no reflection depths other than the bottom of the system, so nonlinearities are limited to the reflection point at (1.6, 0) m.

We present only the errors in the energy flux calculation; the errors in the velocity and pressure perturbation calculations are qualitatively the same as the results in figures 4.3 and 4.4. Figures 4.6(b) and (c) show the

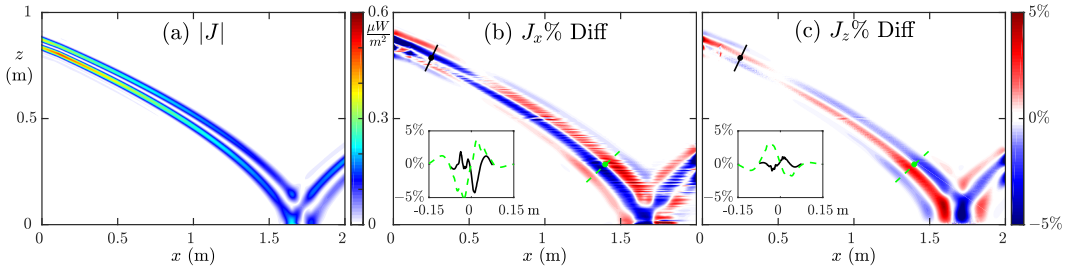

Figure 4.6: (a) The energy flux magnitude from the numerical simulation for the linear N profile. The beam-normalized percent difference between simulation and the Green's function method for the (b) x and (c) z components of the energy flux; the difference is less than 5% for most of the beam, as illustrated by insets showing the difference for two beam transects.

percent difference of the horizontal and vertical components of the energy flux, respectively. As with the tanh N^2 profile comparisons, the errors in the energy flux field are confined to the internal wave beam. Throughout the beam the difference between the simulation and Green's function method is less than 5%, as illustrated by the beam transects in the insets of figures 4.6(b) and (c); the largest errors occur where the beam enters and leaves the domain and where it reflects off the bottom boundary. The transition from pressure perturbation overestimation to underestimation is highlighted by the change from red to blue and vice versa near (0.5, 0.75) m.

4.3 Arbitrary stratification analysis

Implementation of the Green's function method is convenient for systems with stratifications where an analytic representation of the Green's function exists. While some stratifications in the ocean and laboratory may ap-

proximately fit to these particular stratification profiles as we show in figure 4.1, making this density-perturbation-based calculation more general is necessary for most applications. To accomplish this generalization, we use a finite difference method to determine the pressure perturbation field. We present the method in detail along with a comparison between the Green's function method and the finite difference method in section 4.3.1. Then, we apply the finite difference method to an ocean-inspired stratification in section 4.3.2.

4.3.1 Finite difference method

Since the velocity perturbation calculation does not depend on having an analytic stratification, only the calculation of the pressure perturbation field requires modification for application to general stratifications. This is accomplished by implementing a numerical solver of the second order differential equation (4.7). The boundary conditions for this differential equation are analogous to (4.10):

$$\left(\frac{dQ}{dz} - \frac{N^2}{2g}Q\right)\Bigg|_{z=0,\,h} = 0\,. \tag{4.42}$$

We solve equation (4.7) using a second-order finite difference method. The Robin boundary conditions are calculated to second order by adding ghost points to the top and bottom of the domain. This numerical method is applied to both the real and imaginary components for every Fourier mode. After the calculation of $Q(z;k)$ using the finite difference method, the dependence in the x-direction is accounted for by multiplying by the particular Fourier mode

just as it is done for the Green's function method. Finally, the transformation (4.6) is performed to determine the contribution to the pressure perturbation field by that particular mode.

Applying this strategy to the previous analytic stratifications provides a baseline for comparison to the Green's function method. The percent difference of the pressure perturbation fields relative to the Green's function results are presented in figure 4.7. This figure shows that the pressure perturbation fields calculated using the finite difference method are everywhere less than 5% different for the tanh profile and less than 1% different for the linear buoyancy frequency profile when compared to the Green's function pressure perturbation. The only major discrepancy between the two methods is near the narrow transition in the tanh N^2 profile shown in figure 4.7(a). In this region, the Green's function method is consistently more accurate than the finite difference method. This is highlighted in figure 4.7(c) by comparing pressure perturbation profiles just above the transition layer. The discrepancy is likely due to the Green's function's accurately accounting for the rapid change in the buoyancy frequency when it modifies the coefficients in the calculation of the Legendre functions. The length scale of the transformed coordinate variable y of (4.19) is set by the steepness coefficient α. This increases the spacial resolution at rapid transitions. The finite difference method can only account for variations on the scale of the original data set step size, which, in the case of the narrow transition, is too coarse.

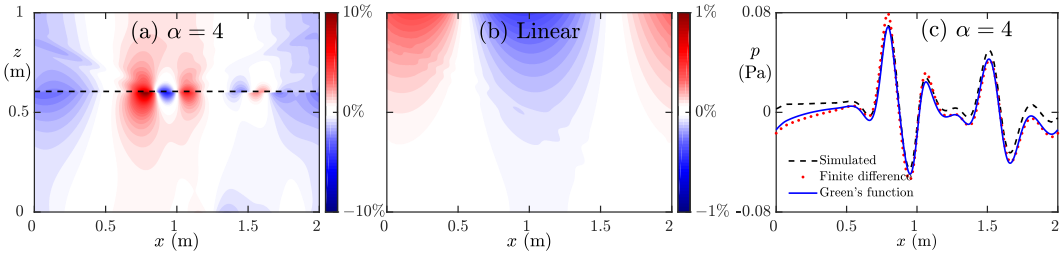

Figure 4.7: The percent difference between the Green's function and finite difference pressure perturbation fields for (a) the narrow transition tanh N^2 profile and (b) the linear profile. (c) Pressure perturbation profiles from the narrow tanh N^2 simulation (black), Green's function method (red), and finite difference method (blue) at $z = 0.605$ m.

4.3.2 Verification of the finite difference method

To further validate the finite difference method, we apply the method to a stratification that does not fit a simple analytic function as was the case in sections 4.1 and 4.2. The stratification we simulate is based on a density profile measured in the ocean during the World Ocean Circulation Experiment (WOCE). The particular profile presented in figure 4.8(a) was measured at 165° W, 51.5° N on September 20^{th}, 1994. This profile features two layers of large density gradient similar to the transitions of the tanh N^2 profiles. The first, more abrupt layer is centered at 30 m below the surface and the second layer is centered at 100 m. The full profile extends to a depth of 1000 m, but there is little variation in the buoyancy frequency below 200 m.

In order to simulate the beams in a similar domain and time scale as the analytic stratifications, we rescale the vertical coordinate and the density. We note that this is done to mimic the actual ocean profile and use it as an

inspiration, rather than to model it accurately. Because the length scale of the transition layers in the simulation are small compared to the length scale of the beams the rescaled simulation done here stress-tests the method.

The first adjustment we make is to provide additional vertical space above the stratification features so that the internal wave beam is fully developed and the resulting reflection off the top of the first transition is visible. The vertical coordinate is scaled from 200 m to 0.8 m in the simulation. The density is also modified to increase the buoyancy frequency, so that the values of the buoyancy frequency are comparable to those used in the Green's function verification. The minimum buoyancy frequency of the scaled density profile is $N = 0.55$ rad/s and the maximum value is $N = 2.40$ rad/s. Finally, we shift the location of forcing to be at (0.2, 1.2) m to have the internal wave beam enter from the top to demonstrate the flexibility of the domain of measurement. The time scale and forcing periodicity match the previous simulations.

The magnitude of the energy flux field is presented in figure 4.8(b). There are a number of reflections and transmissions due to the more complicated density profile. For the first transition layer, the internal wave beam produces reflections off the top and bottom of the pycnocline layer, which can be seen at (0.5, 0.8) m and (1.0, 0.8) m, respectively. In addition to the reflected energy, some of the internal wave energy is trapped in the pycnocline layer and is transported to the right (e.g. (1.25, 0.7) m). A large fraction of the energy however is transmitted through the layer. Very little energy is

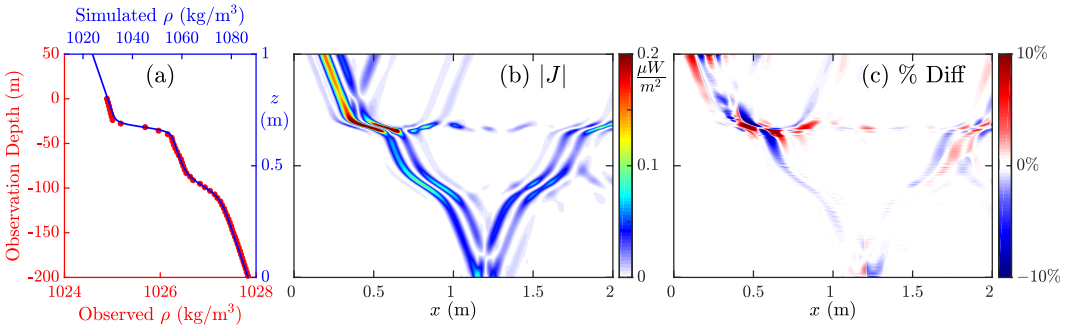

Figure 4.8: (a) Density profile from the ocean (red) and the scaled version used for simulation (blue). (b) The simulated absolute energy flux field. (c) The beam-normalized percent difference between the simulated and finite difference energy flux fields.

reflected off the second layer, allowing the rest of the energy to reflect off the bottom of the domain.

The finite difference method is applied to the modified ocean density profile, and the beam-normalized percent difference of the energy flux magnitude is presented in figure 4.8(c). The largest errors occur near the more abrupt transition layer. The maximum percent difference in this region 28.1%. There is no consistent trend with regards to under or over estimating the energy flux. Outside of the immediate region of the sharper transition, the percent difference is generally within 5%. It is also important to note that the method is able to capture and accurately determine the energy flux in the reflected, transmitted, and trapped internal waves outside of the highly nonlinear first reflection region.

4.4 Conclusions

We have presented two methods for calculating the instantaneous internal wave energy flux field using only density perturbation field data. Both methods are applicable to nonlinear stratifications: the first method, a Green's function method, uses convenient analytic density stratification profiles, while the second, a finite difference method, applies to arbitrary stratification profiles.

Using our Green's function method we obtained the instantaneous energy flux from density perturbations for two buoyancy frequency profiles: one linear in z and the other where $N(z)^2 \propto \tanh(z)$. The difference between the Green's function method and our direct numerical simulations is less than 5% outside of regions containing significant nonlinearity. Despite the Green's function method being based on linear theory, it accurately predicts the energy flux in the transmitted, reflected, and second harmonic beams, which involve significant nonlinearities.

With our finite difference method we showed how to capture the energy flux in an internal wave field containing nonlinear interactions, wave beam reflections, and second harmonic beams for any buoyancy frequency profile $N(z)$. This method was compared with the Green's function method and direct numerical simulations, and again the errors are less than 5% for most of the domain.

The two methods presented here and in chapter 3 [4] allow detailed

studies of the entire instantaneous energy flux field for internal wave field data, as contrasted with methods that yield a single global conversion rate or a time-averaged result. Our methods can be used to determine the instantaneous velocity perturbation, pressure perturbation, and energy flux fields from density perturbation data obtained in experiments using synthetic schlieren or light attenuation measurements. We emphasize that the methods require only the density perturbation field over time and the background buoyancy frequency profile. Application to ocean observations will be possible provided a time-varying density perturbation field can be measured. The methods assume the flow is two dimensional, but future work could extend the method to weakly three-dimensional flows as in ocean applications.

The Matlab GUI "*EnergyFlux*" developed in chapter 3 [4] is extended to include the methods discussed in this paper. The GUI requires density perturbation data, domain coordinates, time step size, and the $N(z)$ profile. A manual and tutorial that reproduces the results in this work is available to make possible straightforward applications of the methods presented here.

Chapter 5

Summary

Internal waves, which are traveling waves supported by buoyancy forces in a stratified fluid, are an intermediary between the large-scale tidal motion and smaller scale mixing and are crucial in understanding the energy budget of the ocean. It is therefore useful to conduct studies regarding the energy flux of internal waves in the laboratory, which is made possible by controlling the salinity of water using the two-bucket method [31]. The waves are measured in the laboratory by two primary methods: PIV, which gives the velocity perturbation field, and synthetic schlieren, which gives the density perturbation field. However the energy flux requires the knowledge of both the velocity and pressure perturbation fields, the simultaneous measurement of which is at the present time extremely difficult. The work presented in this dissertation allows the determination of the energy flux for both types of measurements. For the PIV case, an experimentalist can take any measured velocity field dominated by internal waves and obtain the time-averaged energy flux field, given that the data spans more than one period of oscillation and that the buoyancy frequency profile N is known. For the synthetic schlieren case, an experimentalist can take the measured density perturbation field for internal waves and obtain the instantaneous energy flux field, given that the

buoyancy frequency is known. Specifically for uniform N, linear N, and tanh N^2, the method presented provides an analytic Green's function with which to convolve the density perturbation as the source. For arbitrary empirical N profiles the energy flux is found numerically with a finite-difference method. All the methods presented were verified against direct numerical simulations where all the relevant quantities were known, and the methods were found to be accurate to within a few percent excluding regions where significant non-linearities were present. Matlab programs with user-friendly graphical user interfaces are provided for the implementation of the methods. Overall, the work in this dissertation simplifies the process of determining the energy flux of internal waves produced in the lab, without having to specify any of the topographic details that create the waves, and also without the need to restrict to just vertical modes or impose hydrostatic boundary conditions.

Appendices

Appendix A

Guide to the Matlab GUI using velocity data

The Matlab code and GUI for the stream function method for determining the energy flux and power by Lee et al. [40] are available at `ftp://ftp.aip.org/epaps/phys_fluids/E-PHFLE6-26-052404`. The latest version is available at the following URLs: `http://www.mathworks.com/matlabcentral/fileexchange/44833` and `http://chaos.utexas.edu/wp-uploads/2013/12/internalwaves_streamfunction_fluxfield.zip`. This guide contains information that is needed to use the GUI. All of the following equation references are from the above-mentioned *Physics of Fluids* paper.

A.1 Input data format

The user must first supply the .mat file which contains the velocity components, the grid, and a fluid parameters array containing the background density and buoyancy frequency information. The names of the various arrays can be user-specified, but the defaults are as follows. Horizontal velocity: u, vertical velocity: w, horizontal coordinate: x, vertical coordinate: z, fluid parameters: h_rho0_N.

Velocity components: The velocity components must be two separate

arrays of identical shape. The first dimension is the z direction, the second dimension is the x direction, and the third is time. The units for the inputs for the program are cgs.

Coordinate arrays: The coordinate arrays must be in the same shape as the velocity components minus the time dimension and must also be separate arrays for the x and z coordinates. The arrays are in the form of outputs for the Matlab function "meshgrid." Refer to the Matlab help documents for further details.

Fluid parameters: The fluid parameter array should contain as its first column the heights at which the background density (second column) and buoyancy frequencies (third column) are evaluated. The heights need not match with the z-component coordinate array specified previously; the values for the background density and buoyancy frequency will be interpolated (cubic) to fit it. If the Boussinesq approximation with uniform reference density and N is being used, the two values can be input as scalars.

A.2 Other parameters

The user then specifies the relevant parameters. The frequency of the internal wave field must be supplied in rad/s. Additionally, the number of timesteps in a period of oscillation, the timestep at which to start evaluating the power, and how many periods to average over must be specified. The energy flux expression is time-averaged over an integer number of periods.

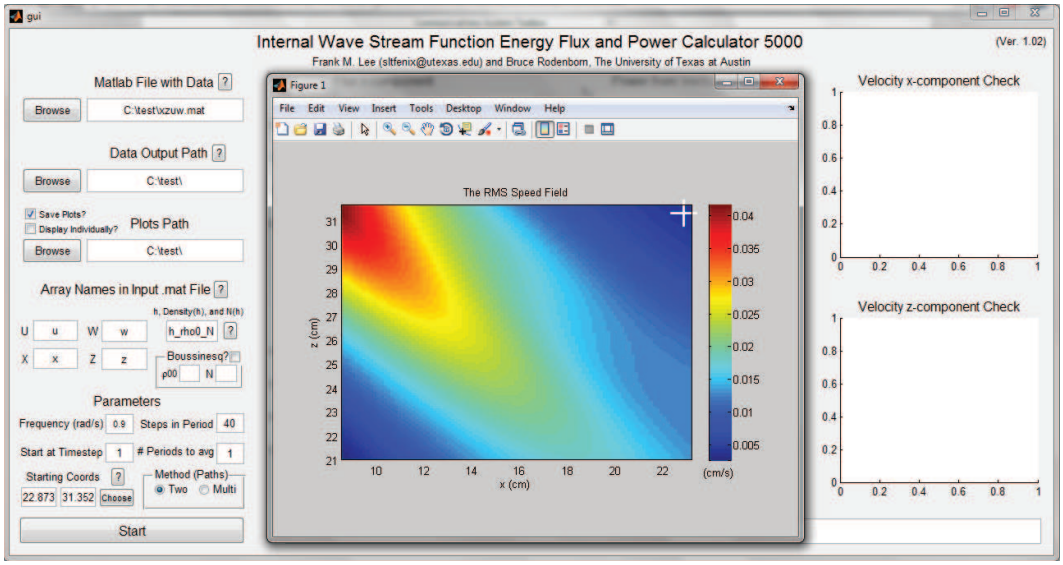

Figure A.1: The user can specify the starting point of the stream function calculation by clicking on a plot of the RMS speed field of the input data.

Additionally, the starting coordinates (in cm) must be specified for the stream function calculation, which can be chosen by clicking on a displayed plot of the RMS speed field, as shown in Fig. A.1. The stream function is taken to be zero at those coordinates at all times. The user can also choose between the two-path and multi-path methods. The multi-path method is roughly an order of magnitude slower than the two-path method, and should be used to reduce the error if the data supplied has a lot of noise.

A.3 Calculation of the stream function

Once all the data and parameters are supplied, the algorithm uses trapezoidal quadrature of the x-velocity values along the z-coordinates, and

the z-velocity values along the x-coordinates to find the stream function at each grid point. For the two-path method, it will average over two simple L-shaped paths from the starting point to the evaluation point given by equations (2.13) and (2.14). For the multi-path method it will average over every Z-shaped path within the box that forms between the starting point and the evaluation point which is given by equations (2.15) and (2.16). Note that if the starting point and evaluation point have the same x or z coordinate, then the only possible path is a straight line. The two-path method calculates only two path integrals for each grid point (excluding the points in line with the starting point), which means it will integrate over $2MN - M - N$ paths, where M is the grid size in x, and N is the grid size in z. The multi-path method calculates $M + N + 2$ paths for each point, where M and N are the number of grid points between the evaluation point and the initial point in the x and z directions. Then the total number of paths integrated for the whole grid is $\frac{1}{2}[M^2N + MN^2 - (M + N)^2 + 3(M + N) - 4]$. The stream function is found for every timestep in the specified range. Derivatives of the calculated stream function are taken and checked against the input velocity components at the initial timestep at the middle of the domain.

A.4 Calculation of the energy flux

Once the stream function $\psi(x, z, t)$ has been calculated, $\varphi(x, z)$ and its derivatives are calculated (equations (2.17) – (2.19)). The real part of φ is found by trapezoidal quadrature in the time direction at each grid point where

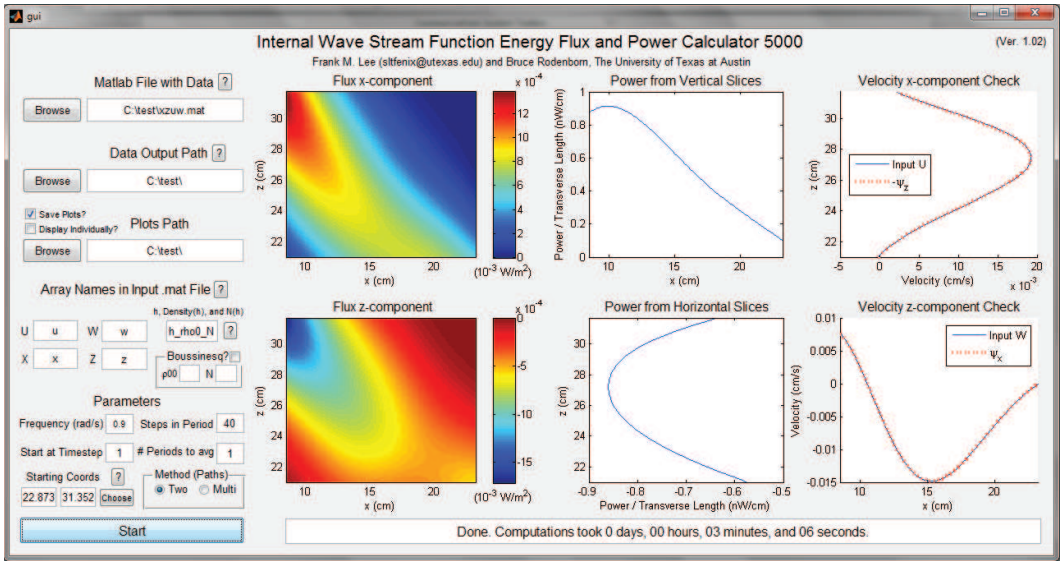

Figure A.2: After the various input parameters are inserted into the GUI, the Matlab program calculates and displays the flux fields, the powers, and velocity checks.

the integrand is the product of the stream function and $\cos \omega t$. The imaginary part is found using $\sin \omega t$ in place of $\cos \omega t$. The derivatives are done the same way except the velocity components are used instead of the stream function. Then the energy flux (equation (2.10)) is calculated using these quantities. The flux fields and the powers are displayed (Fig. A.2) and output into both .txt and .mat files to the specified folder.

Appendix B

Guide to the Matlab GUI using density perturbation data

B.1 Cropped domains and buffering

Density perturbation data from synthetic schlieren measurements are often from regions that do not contain the boundaries of the fluid system, and the boundary conditions (3.14) and (3.16) used to find the pressure perturbations are in general not satisfied on the boundaries of a 'cropped' measurement window. Cropping affects the calculation of pressure but not the calculation of the vertical velocity field (3.11), and as long as there is a point in the domain where the horizontal velocity is zero, the calculation for the horizontal velocity field (3.12) is unaffected as well. In this section, we use simulation data that have been cropped to test the effects on computations of the pressure and energy flux, and we present a procedure to minimize its impact.

The Fourier series expansion in (3.21) reduces the dimensionality of the problem while respecting the boundary condition (3.14). Cropping the left and right sides of the domain in a way that results in the beam passing through the side boundaries will in general violate the periodic boundary condition and introduce a step discontinuity. Because the pressure perturbation

is calculated as a Fourier series in the horizontal direction (3.30), this cropping introduces Gibbs-phenomenon-like edge artifacts in the solution on the left and right boundaries. For reference, we show in figure B.1(a) the simulated pressure perturbation field in the domain used in the main body of the paper, and the impact of cropping the sides is shown in figure B.1(b). The edge artifacts resulting from the cropping can be present at the opposite end of the domain from where the beam penetrates, but the cropping does not significantly change the pressure field in the middle of the domain.

The boundary conditions at the top and bottom (3.16) are physically more important than those at the sides (3.14) because a no-flux condition is applied at the top and bottom for the Green's function (3.24). If the beam passes through the top and/or bottom boundary, then the no-flux condition is violated and error is introduced in the Green's function. Figure B.1(c) shows that the resulting errors can be significant near the top and bottom boundaries, but again in the middle region the solution is quite good. When the data are cropped in both directions, the errors from both the side and top-bottom cropping are present as one might expect, as shown in figure B.1(d).

To minimize errors caused by cropping we introduce a method of buffering the data. This buffering is applied only to the pressure calculation as the velocity calculations do not depend on the boundary conditions. Figure B.2(a) shows an example of buffering the density perturbation field used to calculate the pressure perturbation in the cropped domain of figure B.1(d). The original domain inside the black dashed box is extended by 5% in all directions.

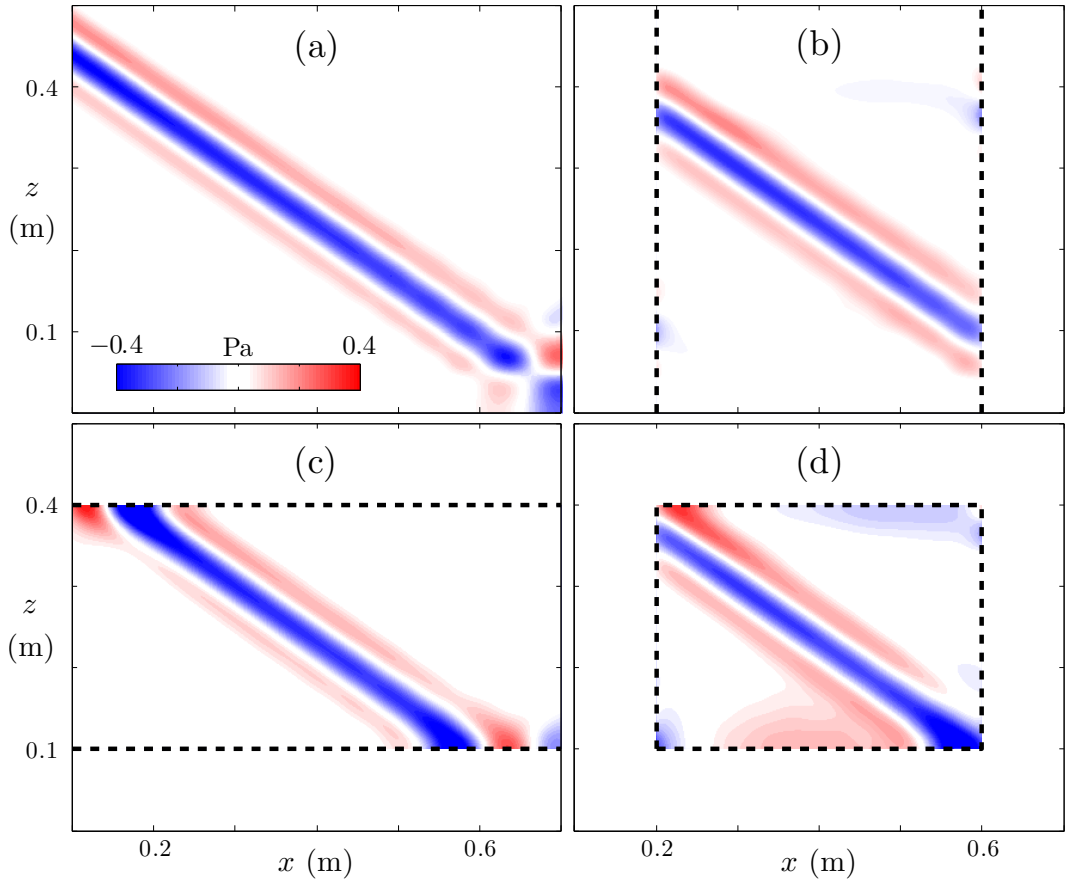

Figure B.1: Calculated pressure perturbation fields for the whole fluid domain (a) and for domains that have been cropped on the sides (b), the top and bottom (c), and both (d). The artifacts near the edges of the cropped domains (b), (c), and (d) arise from the violation of the boundary conditions (3.14) and (3.16). (Fig. 7 from [4])

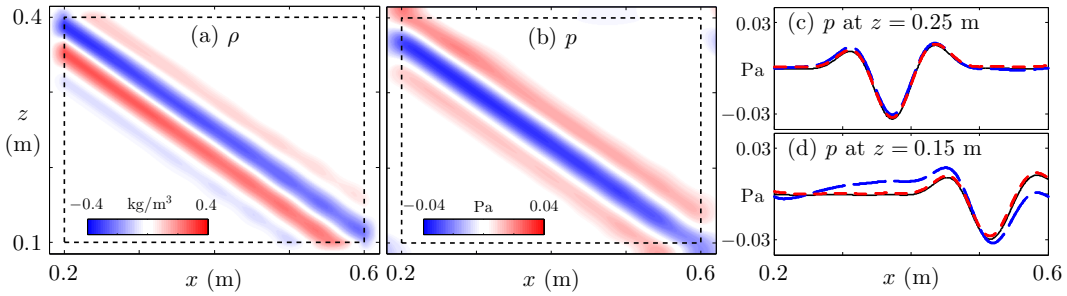

Figure B.2: (a) The density perturbation field calculated from the original data inside the black dashed box plus a 5% buffer area. (b) Pressure perturbation field (in Pascals, Pa) obtained from the buffered density perturbation data. This is much better than the un-buffered calculation from figure B.1(d). Comparison of the simulated pressure perturbation (black solid) at heights $z = 0.25$ m (c) and $z = 0.15$ m (d) with the pressure perturbation calculated by the Green's function method both with a buffer (red dashed narrow) and without (blue dashed wide). (Fig. 8 from [4])

The jump in density perturbation is removed by applying a smoothing filter on the new density perturbation field. In this smoothing process the density perturbation at the boundaries of the new domain is held at zero, and the values in the old domain are diffused into the expanded domain. This diffusion process results in modifications to the density perturbation field in the region of interest. The original density perturbation field is then substituted back into the region of interest. The final result is a density perturbation field that smoothly transitions from the original density perturbation to zeros along the edges, as shown in figure B.2(a).

The pressure perturbation calculation can then be applied to the extended domain and the results with a 5% buffer region are shown for the density perturbation field in figure B.2(a), and for the pressure perturbation

field in figure B.2(b). For this small buffer size there are still some erroneous signatures in the top right and bottom left of the domain that are similar to the results from cropping the sides of the domain, but these errors are much smaller and are mostly contained in the buffer region. The addition of the buffer significantly reduces the error in the pressure perturbation calculation throughout the original domain. Figure B.2(c) shows that the results in the middle of the domain are essentially the same with and without a buffer, but near the boundaries the benefit of the buffer is significant, as figure B.2(d) shows. The normalized rms difference relative to the direct simulation results for the pressure perturbation calculation without the use of a buffer over the entire domain is 17%, while the addition of a 5% buffer around the whole domain reduces the normalized rms error to 5%. Going further with a 20% buffer reduces the error to 3%, which is comparable to the precision found in the verification (section 3.3.1).

Buffering the data domain seems to bring subtly different beneficial effects for the horizontal and vertical directions. The main benefit of buffering the left and right sides of the domain seems to be the removal of the step discontinuities at those boundaries. Since the original density perturbation source is Fourier expanded in the horizontal direction, the solution for the pressure perturbation is a Fourier series of Green's functions G_k and their corresponding Fourier coefficient fields F_k. By removing the step discontinuities in the density perturbation field, the Gibbs-phenomenon-like edge effects in the series solution for the pressure perturbation is significantly reduced. However, this

means that excessive buffering in the horizontal direction (approaching the horizontal length-scale of the beam) can artificially introduce lower k modes and produce errors.

The main benefits of buffering the top and bottom of the domain seem to be to push the no-flux boundary away from the original boundary, and to produce an extension of the beam that somewhat mimics the original density perturbation. Pushing the no-flux boundary away makes the Green's function behavior more appropriate for a beam that does not reflect at the boundary. The extension of the beam in the buffer region provides an approximate source that, combined with the aforementioned improved Green's function, produces a better result for the pressure perturbation near the boundary in the original domain. The effective range (for one e-folding) of the Green's function's response for mode k is roughly $1/k$, and for the data used in this paper this value is roughly 10 cm for the first mode. Thus for a given point in the domain, density perturbation sources up to 10 cm away contribute significantly to the solution for the pressure perturbation at that point. This is a big reason why cropping the domain produces errors near the edges but not in the middle; the points near the edges are missing density perturbation sources from the cropping, while the points in the middle are mostly unaffected because they "see" all of their appropriate sources within the effective range. The extension that mimics the beam in the diffused buffer region provides approximate density perturbation sources for the points near the boundaries to reduce the error. Buffering the top and bottom of the domain does not have the same limitation

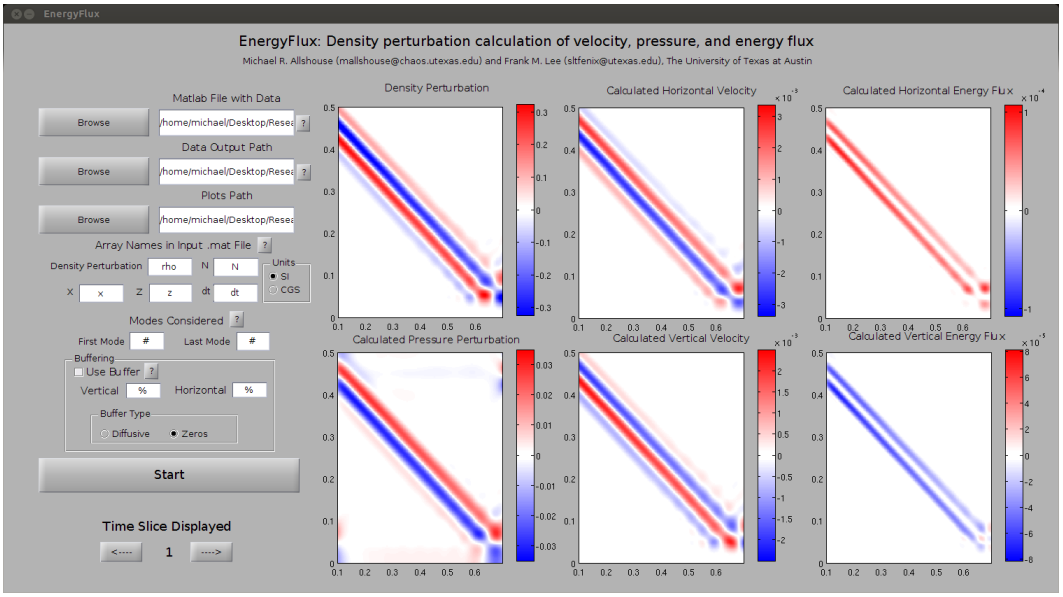

Figure B.3: Demonstration of the GUI interface *EnergyFlux* featuring the settings used for the results in section 3.3.2. (Fig. 9 from [4])

as buffering the sides, and can be taken as large as one wants. However, for the data set presented here, not much was gained beyond 15% buffering and the results do not seem to converge to the real answer near the edges for larger buffering, since the beam extension in the buffered region never quite looks like the original beam that has been cropped away.

B.2 Implementation of Matlab GUI *EnergyFlux*

To aid in the implementation of this method, a graphical user interface *EnergyFlux* was developed for Matlab. This software is available in the supplemental materials along with a tutorial for use. The GUI, manual, and data set can be accessed at `https://www.mathworks.com/matlabcentral/`

`fileexchange/55514-energyflux`. The GUI requires only the density perturbation field over a number of time steps, the corresponding coordinates, buoyancy frequency, and time step size. The GUI allows for the implementation of the data buffering procedure presented in appendix B.1 and the selection of what range of horizontal modes to consider in the calculation.

Appendix C

Tutorial for the Matlab GUI *EnergyFlux*

The Matlab code and GUI for the Green's function based approach for determining the velocity, pressure, and energy flux by Allshouse, Lee, Morrison, and Swinney are available at `https://journals.aps.org/prfluids/supplemental/10.1103/PhysRevFluids.1.014301`. The latest version is available at the following URLs, `https://www.mathworks.com/matlabcentral/fileexchange/55514-energyflux` and `http://chaos.utexas.edu/wordpress/wp-content/uploads/2016/06/supplmental-information.zip`. This guide contains information that is needed to use the GUI and a tutorial to analyze the attached data set. All of the necessary equations and derivations are from chapter 3. To demonstrate the implementation of the code, a data set from our simulated results is included.

C.1 Input data format

The user must first supply the .mat file which contains the density perturbation field and the coordinate grid. There is also the option to include the buoyancy frequency, N, and the time step; however, these parameters can be input manually in the GUI. The names of the various arrays can be user-

specified, but the defaults are as follows: Density perturbation - *rho*, horizontal coordinate: x, vertical coordinate, z, buoyancy frequency - N, and time step - dt.

Density perturbation: The density perturbation is a single array that contains density perturbation data for multiple time steps. The first dimension is the z direction, the second dimension is the x direction, and the third is time. In order to calculate the time derivatives, there must be density perturbation for at least two time instances.

Coordinate arrays: The x and z coordinate arrays must be in the same shape as the density perturbation array minus the time dimension. These arrays are in the form of outputs for the Matlab function "meshgrid."

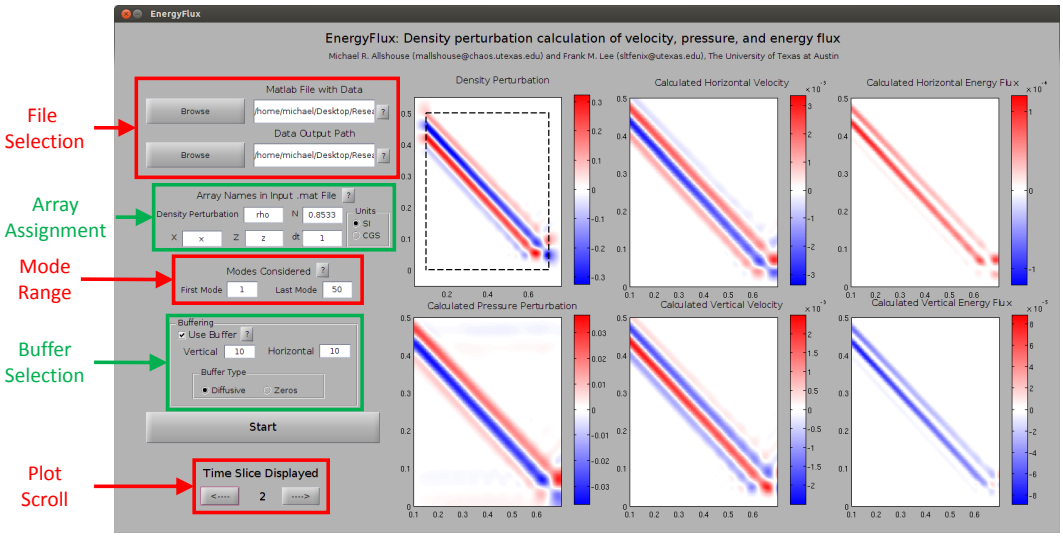

Figure C.1: *EnergyFlux* GUI with labels.

Optional parameters: The buoyancy frequency and the time step are optional parameters that can be included in the data file. Both values must be scalars.

C.2 Pre-execution steps

The following steps must be performed before the calculation.

- *Data set selection* - By clicking the "Browse" button for the "Matlab File with Data" you will have the ability to select the .mat file containing the necessary data.

- *Output folder selection* - By default the output data will be saved into the same folder that contains the input data. If you want to change this select the "Browse" button for the "Data Output Path."

- *Set Array Names* - Set the variable names for the density perturbation and coordinates. If you have save the buoyancy frequency and time step in the array file set these variable names as well. If you want to input this manually, simply replace the variable name with the value.

- *Units convention* - Select the SI or CGS units radio button based on the unit convention of your data set.

C.3 Optional features

The user is given two optional features that can be used. The first sets the mode number range for the analysis. The second adds a data buffer around the original data set.

C.3.1 Mode number selection

The calculation performs a Fourier analysis on each horizontal slice of the data set and then for each mode within the calculation range performs the Green's function integration. There are potential situations where not all modes contribute significantly to the output result, and reducing the number of modes considered will reduce the run time accordingly. If you know what the mode range should be, you can replace the "#" with the number. If you are unsure what modes to consider, the code will automatically set them for you. The range automatically selected starts with the first mode and ends at the first mode where the spectral contribution is less than 1% of the maximum.

C.3.2 Data buffering

As explained in appendix B, buffering the data can reduce erroneous signatures in the pressure field. To include buffering, check the box next to "Use Buffer." If a buffer is used, you will need to set its extent as a percentage of the domain in that direction. For example, a 10% vertical buffer will extend the domain up by 10% and down by 10% of the original height of the domain. There are two types of buffering. The "Diffusive" option creates a buffer with

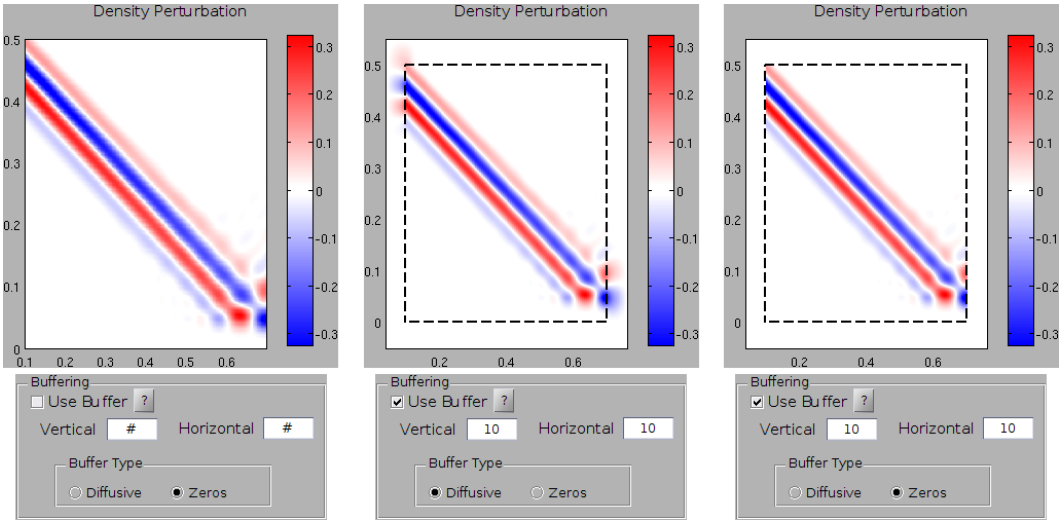

Figure C.2: (left) No buffer used. (Center) "Diffusive" and (right) "Zero" buffering options.

a gradual decay of the density perturbation from the edge of the original data set to zero at the new boundary. The "Zeros" option extends the domain with a density perturbation of zero. When buffering is used, the density perturbation plot will show the extended domain. The result of different "Buffering Selection" and the corresponding density plots are presented in figure C.2.

C.4 Execution and results

To execute the calculation after the inputs, modes, and buffering have been set, click the "Start button." There will be a number of progress bars that pop up as the calculation is performed. As each calculation is completed the results will be plotted to the right. The output data will be saved into the designated folder as "greens_function_outputs.mat".

Note: You must be in the directory containing the GUI and the necessary functions or have added that directory to your path in order to run the GUI.

C.5 Tutorial

Along with the gui and functions, a data set has been provided to the user to give an example of the data format and to execute this tutorial.

C.5.1 Download and startup

Download the zip folder and extract the files. This should contain five .m files (*buffer_data, EnergyFlux, press_calculation, redblue, and vel_calculation*), *EnergyFlux.fig, example_data.mat*, and *EnergyFlux.pdf*. All the files must remain in the folder, and this must be the current directory of Matlab to run the GUI,

To start the GUI, you can run the command `EnergyFlux` in the Command Window. Double clicking *EnergyFlux.fig* will open the GUI but it will NOT allow you to use it.

C.5.2 Simple analysis

1. With the GUI open, click the top "Browse" button in the "File Selection" section. This will open a browser for you to select the file *example_data.mat*.

2. Select *example_data.mat* and click "Open".

3. To perform the most basic analysis click the "Start" button.

4. After the plots are produced, toggle between different time instances by selecting the right and left arrows in the "Plot Scroll" section.

C.5.3 Manually set buoyancy frequency and time step

1. Perform the first two steps of the "Simple analysis" if the GUI has been closed.

2. Set the buoyancy frequency by changing the "N" to 0.8533, which is the value from the paper.

3. Set the time step by changing the "dt" to 1.

4. To perform the analysis click the "Start" button.

C.5.4 Selecting the mode range

1. Perform the first two steps of the "Simple analysis" if the GUI has been closed.

2. Change the "Start Mode" to 2.

3. Change the "Last Mode" to 30.

4. To perform the analysis click the "Start" button.

C.5.5 Using buffering

1. Perform the first two steps of the "Simple analysis" if the GUI has been closed.

2. Check the box next to "Use Buffer."

3. Set the vertical and horizontal percentages to "10" representing an extension of the domain by 10% in all four directions.

4. Select the "Diffusive" option.

5. To perform the analysis click the "Start" button.

Appendix D

Evaluation of the tanh profile Green's function

D.1 Cancellation of Legendre functions

The Green's function is given by

$$\tilde{G}(y,y') = \frac{-1}{D\,W} \begin{cases} \Big(\Phi_2 P_\nu^\mu(y') + \Pi_2 Q_\nu^\mu(y')\Big)\Big(\Phi_1 P_\nu^\mu(y) + \Pi_1 Q_\nu^\mu(y)\Big), & y < y' \\ \Big(\Phi_1 P_\nu^\mu(y') + \Pi_1 Q_\nu^\mu(y')\Big)\Big(\Phi_2 P_\nu^\mu(y) + \Pi_2 Q_\nu^\mu(y)\Big), & y > y', \end{cases} \tag{D.1}$$

where

$$\Pi_{1,2} = \frac{dP_\nu^\mu(y_{0,h})}{dy} - \frac{N_{1,2}^2}{2\,g\,(1-y_{0,h}^2)} P_\nu^\mu(y_{0,h}) \tag{D.2}$$

$$\Phi_{1,2} = -\frac{dQ_\nu^\mu(y_{0,h})}{dy} + \frac{N_{1,2}^2}{2\,g\,(1-y_{0,h}^2)} Q_\nu^\mu(y_{0,h}). \tag{D.3}$$

However, the Green's function in this form is unsuitable for direct numerical evaluation because of the factors $1-y_{0,h}^2$ in (D.2) and (D.3). Because y_0 and y_h are extremely close to -1 and 1, respectively, $1-y_0^2$ and $1-y_h^2$ are extremely close to 0. Thus we must somehow remove these factors from the expression. We note that we can use the following recurrence relation (Abramowitz & Stegun 8.5.4),

$$\frac{dP_\nu^\mu(y)}{dy} = \frac{(\nu+\mu)P_{\nu-1}^\mu(y) - \nu\,y\,P_\nu^\mu(y)}{(1-y^2)}, \tag{D.4}$$

which works for both P and Q, to remove the derivative and combine the terms in (D.2) and (D.3) to give

$$\Pi_{1,2} = \frac{(\nu+\mu)P^{\mu}_{\nu-1}(y_{0,h}) - (\nu\, y_{0,h} + N^2_{1,2}/2g)\, P^{\mu}_{\nu}(y_{0,h})}{(1-y^2_{0,h})}, \tag{D.5}$$

$$\Phi_{1,2} = \frac{-(\nu+\mu)Q^{\mu}_{\nu-1}(y_{0,h}) + (\nu\, y_{0,h} + N^2_{1,2}/2g)\, Q^{\mu}_{\nu}(y_{0,h})}{(1-y^2_{0,h})}. \tag{D.6}$$

We can then define the following to rescale our parameters,

$$\Pi_{1,2} = \frac{1}{(1-y^2_{0,h})}\pi_{1,2} \qquad \Phi_{1,2} = \frac{1}{(1-y^2_{0,h})}\varphi_{1,2}, \tag{D.7}$$

which means that then the denominator rescales like the following,

$$D = \begin{vmatrix} \Pi_1 & \Pi_2 \\ \Phi_1 & \Phi_2 \end{vmatrix} = \frac{1}{(1-y^2_0)(1-y^2_h)} \begin{vmatrix} \pi_1 & \pi_2 \\ \varphi_1 & \varphi_2 \end{vmatrix} = \frac{d}{(1-y^2_0)(1-y^2_h)}. \tag{D.8}$$

Then the near-zero factors $(1-y^2_0)(1-y^2_h)$ can be cancelled from the numerator and denominator of the Green's function (D.1) to give:

$$\tilde{G}(z,z') = \frac{-1}{dW} \begin{cases} \Big(\varphi_2 P^{\mu}_{\nu}(y') + \pi_2 Q^{\mu}_{\nu}(y')\Big)\Big(\varphi_1 P^{\mu}_{\nu}(y) + \pi_1 Q^{\mu}_{\nu}(y)\Big), & y < y' \\ \Big(\varphi_1 P^{\mu}_{\nu}(y') + \pi_1 Q^{\mu}_{\nu}(y')\Big)\Big(\varphi_2 P^{\mu}_{\nu}(y) + \pi_2 Q^{\mu}_{\nu}(y)\Big), & y > y'. \end{cases} \tag{D.9}$$

However, the expression is still not suited for numerical computation because P and Q are being evaluated at coordinates where the terms become really large. To this end, we will express Q in terms of P and cancel some terms in

$$\varphi_1 P^{\mu}_{\nu}(y) + \pi_1 Q^{\mu}_{\nu}(y). \tag{D.10}$$

Using Gradshteyn and Ryzhik 8.705,

$$Q_\nu^\mu(y) = \frac{\pi}{2\sin(\mu\pi)}\left[P_\nu^\mu(y)\cos(\mu\pi) - \frac{\Gamma(\nu+\mu+1)}{\Gamma(\nu-\mu+1)}P_\nu^{-\mu}(y)\right], \tag{D.11}$$

we can express (D.10) in terms of just P:

$$\begin{aligned}
&P_\nu^\mu(y)\varphi_1 + Q_\nu^\mu(y)\pi_1 \\
&\quad= P_\nu^\mu(y)\left[-(\nu+\mu)Q_{\nu-1}^\mu(y_0) + \left(\nu\, y_0 + \frac{N_1^2}{2g}\right) Q_\nu^\mu(y_0)\right] \\
&\qquad + Q_\nu^\mu(y)\left[(\nu+\mu)P_{\nu-1}^\mu(y_0) - \left(\nu\, y_0 + \frac{N_1^2}{2g}\right) P_\nu^\mu(y_0)\right] \qquad \text{(D.12)} \\
&\quad= -P_\nu^\mu(y)\frac{(\nu+\mu)\pi}{2\sin(\mu\pi)}\left[P_{\nu-1}^\mu(y_0)\cos(\mu\pi) - \frac{\Gamma(\nu+\mu)}{\Gamma(\nu-\mu)}P_{\nu-1}^{-\mu}(y_0)\right] \\
&\qquad + P_\nu^\mu(y)\frac{\left(\nu\, y_0 + \frac{N_1^2}{2g}\right)\pi}{2\sin(\mu\pi)}\left[P_\nu^\mu(y_0)\cos(\mu\pi) - \frac{\Gamma(\nu+\mu+1)}{\Gamma(\nu-\mu+1)}P_\nu^{-\mu}(y_0)\right] \\
&\qquad + \frac{(\nu+\mu)\pi}{2\sin(\mu\pi)}\left[P_\nu^\mu(y)\cos(\mu\pi) - \frac{\Gamma(\nu+\mu+1)}{\Gamma(\nu-\mu+1)}P_\nu^{-\mu}(y)\right] P_{\nu-1}^\mu(y_0) \\
&\qquad - \frac{\left(\nu\, y_0 + \frac{N_1^2}{2g}\right)\pi}{2\sin(\mu\pi)}\left[P_\nu^\mu(y)\cos(\mu\pi) - \frac{\Gamma(\nu+\mu+1)}{\Gamma(\nu-\mu+1)}P_\nu^{-\mu}(y)\right] P_\nu^\mu(y_0). \qquad \text{(D.13)}
\end{aligned}$$

In (D.13), the first and fifth, and the third and seventh terms cancel. Then it becomes

$$\begin{aligned}
&P_\nu^\mu(y)\varphi_1 + Q_\nu^\mu(y)\pi_1 \\
&\quad= \frac{(\nu+\mu)\pi}{2\sin(\mu\pi)}\left[\frac{\Gamma(\nu+\mu)}{\Gamma(\nu-\mu)}P_\nu^\mu(y)P_{\nu-1}^{-\mu}(y_0) - \frac{\Gamma(\nu+\mu+1)}{\Gamma(\nu-\mu+1)}P_{\nu-1}^\mu(y_0)P_\nu^{-\mu}(y)\right] \\
&\qquad + \frac{\left(\nu\, y_0 + \frac{N_1^2}{2g}\right)\pi}{2\sin(\mu\pi)}\frac{\Gamma(\nu+\mu+1)}{\Gamma(\nu-\mu+1)}\left[P_\nu^\mu(y_0)P_\nu^{-\mu}(y) - P_\nu^\mu(y)P_\nu^{-\mu}(y_0)\right]. \qquad \text{(D.14)}
\end{aligned}$$

The same cancellations occur for $P^{\mu}_{\nu}(y)\varphi_2 + Q^{\mu}_{\nu}(y)\pi_2$. However, there are still very large terms present in the expression.

D.2 Exponential expansion

We can see the exponential behavior if we do the appropriate transformations. We express the P's in terms of the Gauss hypergeometric function ${}_2F_1$ and get the explicit exponential behavior by undoing our coordinate transform,

$$y(z) = \tanh(\alpha(z - z_t)) = \frac{1 - e^{-2\alpha(z-z_t)}}{1 + e^{-2\alpha(z-z_t)}} = \frac{e^{2\alpha(z-z_t)} - 1}{e^{2\alpha(z-z_t)} + 1}. \tag{D.15}$$

If $z \sim h$, then we have

$$P^{\mu}_{\nu}(y) = \frac{1}{\Gamma(1-\mu)} \left(\frac{1+y}{1-y}\right)^{\mu/2} F\left(-\nu, \nu+1; 1-\mu; \frac{1-y}{2}\right), \tag{D.16}$$

$$P^{\mu}_{\nu}(y) = \frac{e^{\mu\alpha(z-z_t)}}{\Gamma(1-\mu)} F\left(-\nu, \nu+1; 1-\mu; f^{+}(z)\right), \tag{D.17}$$

where

$$f^{+}(z) = \frac{1}{1 + e^{2\alpha(z-z_t)}} \approx 0. \tag{D.18}$$

The hypergeometric function evaluated at this point converges to 1. However, if $z \sim 0$, the hypergeometric function tends to diverge and we need to use a linear transformation formula (Abramowitz & Stegun 15.3.6) to shift the argument and bring the divergent behavior out into an exponential factor.

This gives

$$P_\nu^\mu(y) = \frac{\left(\frac{1+y}{1-y}\right)^{\mu/2}}{\Gamma(1-\mu)} F\left(-\nu, \nu+1; 1-\mu; \frac{1-y}{2}\right) \tag{D.19}$$

$$= \frac{\left(\frac{1+y}{1-y}\right)^{\mu/2}}{\Gamma(1-\mu)} \left[\frac{\Gamma(1-\mu)\Gamma(-\mu)}{\Gamma(1-\mu+\nu)\Gamma(-\mu-\nu)} F\left(-\nu, \nu+1; 1+\mu; \frac{1+y}{2}\right) + \left(\frac{1+y}{2}\right)^{-\mu} \frac{\Gamma(1-\mu)\Gamma(\mu)}{\Gamma(-\nu)\Gamma(\nu+1)} F\left(1-\mu+\nu, -\mu-\nu; 1-\mu; \frac{1+y}{2}\right)\right] \tag{D.20}$$

$$P_\nu^\mu(y) = \frac{\Gamma(-\mu)e^{\mu\alpha(z-z_t)}}{\Gamma(1-\mu+\nu)\Gamma(-\mu-\nu)} F(-\nu, \nu+1; 1+\mu; f^-(z)) + \frac{\Gamma(\mu)(e^{\alpha(z-z_t)} + e^{-\alpha(z-z_t)})^\mu}{\Gamma(-\nu)\Gamma(\nu+1)} F(1-\mu+\nu, -\mu-\nu; 1-\mu; f^-(z)), \tag{D.21}$$

where

$$f^-(z) = \frac{1}{1+e^{-2\alpha(z-z_t)}} \approx 0. \tag{D.22}$$

Then, using all this, we can get the exact exponential behavior of our terms that look like $P_\nu^\mu(y)\varphi_{1,2} + Q_\nu^\mu(y)\pi_{1,2}$. For $z \approx h$ we have

$$P_\nu^\mu(y)\varphi_1 + Q_\nu^\mu(y)\pi_1 = a_1 e^{\alpha\mu z} + a_2(e^{-\alpha z} + e^{-\alpha(z-2z_t)})^{-\mu} + a_3 e^{-\alpha\mu z} + a_4(e^{-\alpha z} + e^{-\alpha(z-2z_t)})^\mu, \tag{D.23}$$

$$P_\nu^\mu(y)\varphi_2 + Q_\nu^\mu(y)\pi_2 = b_1 e^{-\alpha\mu(z-h)} + b_2 e^{\alpha\mu(z-h)}. \tag{D.24}$$

Here, the first terms are the largest, and the various factors like a_1 are comprised of gamma functions and hypergeometric functions. For $z \approx 0$ we

have

$$\begin{aligned} P_\nu^\mu(y)\varphi_1 + Q_\nu^\mu(y)\pi_1 =& c_1\,(e^{\alpha z} + e^{-\alpha(z-2z_t)})^\mu + c_2\,(e^{-\alpha z} + e^{-\alpha(z-2z_t)})^\mu \\ &+ c_3\left(\frac{e^{-\alpha z_t} + e^{\alpha z_t}}{e^{\alpha(z-z_t)} + e^{-\alpha(z-z_t)}}\right)^\mu + c_4\left(\frac{e^{\alpha(z-z_t)} + e^{-\alpha(z-z_t)}}{e^{-\alpha z_t} + e^{\alpha z_t}}\right)^\mu \\ &+ c_5\,e^{\alpha\mu z} + c_6\,e^{-\alpha\mu z} \\ &+ c_7\,(e^{-\alpha z} + e^{-\alpha(z-2z_t)})^{-\mu} + c_8\,(e^{\alpha z} + e^{-\alpha(z-2z_t)})^{-\mu}, \end{aligned} \tag{D.25}$$

$$\begin{aligned} P_\nu^\mu(y)\varphi_2 + Q_\nu^\mu(y)\pi_2 =& d_1\,e^{-\alpha\mu(z-h)} + d_2\,(e^{\alpha(z-h)} + e^{-\alpha(z+h-2z_t)})^{-\mu} \\ &+ d_3\,e^{\alpha\mu(z-h)} + d_4\,(e^{\alpha(z-h)} + e^{-\alpha(z+h-2z_t)})^{\mu}. \end{aligned} \tag{D.26}$$

For (D.25), the first two terms are extremely large, have opposite sign, and have almost the same magnitude, giving a result that is extremely small that produces errors because of the limit of machine precision. Thus for numerical evaluation we take c_1 and c_2 to be zero. The determinant looks like the following:

$$\begin{aligned} D =& m_1\,e^{\alpha\mu h} + m_2\,(e^{-\alpha h} + e^{-\alpha(h-2z_t)})^{-\mu} \\ &+ m_3\,e^{-\alpha\mu h} + m_4\,(e^{-\alpha(h)} + e^{-\alpha(h-2z_t)})^{\mu}. \end{aligned} \tag{D.27}$$

This means we can divide out $e^{\alpha\mu h}$ from both the numerator and denominator of the Green's function to reduce term sizes. Also, different combinations of (D.23) - (D.26) should be used depending on what values z and z' take. For instance, if $z \approx 0$ and $z' = z + \epsilon$, then we will multiply (D.26) evaluated at z' with (D.25) evaulated at z. However, if $z \approx h$ and $z' \approx 0$, then we will multiply (D.24) evaluated at z with (D.25) evaluated at z'. The following values for a_i, b_i, c_i, d_i, and m_i have been simplified using the following

expressions from Abramowitz & Stegun 6.1.15 and 6.1.17,

$$\Gamma(x+1) = x\,\Gamma(x), \tag{D.28}$$

$$\Gamma(x)\,\Gamma(1-x) = \frac{\pi}{\sin \pi x}. \tag{D.29}$$

Also, to save space we simplify the notation:

$$\gamma_{1,2} = \nu y_{0,h} + \frac{N_{1,2}^2}{2\,g}, \tag{D.30}$$

$$F(a,b;c;f^{\pm}(z)) = F^{a,b}_{c,\pm}(z), \tag{D.31}$$

$$\delta_{\pm} = \nu \pm \mu. \tag{D.32}$$

$$a_1 = \Gamma^2(\mu)\frac{\sin \delta_- \pi}{2\pi}\left[\delta_+ F^{1-\nu,\nu}_{1-\mu,-}(0) + \gamma_1 F^{-\nu,1+\nu}_{1-\mu,-}(0)\right] F^{-\nu,1+\nu}_{1-\mu,+}(z) \tag{D.33}$$

$$a_2 = \frac{\Gamma(\delta_+)}{\Gamma(\delta_-)}\frac{\sin \nu\pi}{2\sin \mu\pi}\delta_+ \left[\frac{-1}{\mu}F^{\delta+,1-\delta_-}_{1+\mu,-}(0) + \frac{\gamma_1}{\delta_-}F^{1+\delta_+,-\delta_-}_{1+\mu,-}(0)\right] F^{-\nu,1+\nu}_{1-\mu,+}(z) \tag{D.34}$$

$$a_3 = \frac{\Gamma^2(\delta_+)}{\Gamma^2(\delta_-)\Gamma^2(\mu)}\frac{\pi \sin \delta_+\pi}{2\sin^2 \mu\pi}\frac{\delta_+^2}{\mu^2\delta_-}\left[F^{1-\nu,\nu}_{1+\mu,-}(0) + \frac{\gamma_1}{\delta_-}F^{-\nu,1+\nu}_{1+\mu,-}(0)\right] F^{-\nu,1+\nu}_{1+\mu,+}(z) \tag{D.35}$$

$$a_4 = \frac{\Gamma(\delta_+)}{\Gamma(\delta_-)}\frac{\sin \nu\pi}{2\sin \mu\pi}\frac{\delta_+}{\mu\delta_-}\left[-\delta_+ F^{\delta_-,1-\delta_+}_{1-\mu,-}(0) - \gamma_1 F^{1+\delta_-,-\delta_+}_{1-\mu,-}(0)\right] F^{-\nu,1+\nu}_{1+\mu,+}(z) \tag{D.36}$$

$$b_1 = \frac{\Gamma(\delta_+)}{\Gamma(\delta_-)}\frac{\delta_+}{2\mu\delta_-}\left[-\delta_+ F^{1-\nu,\nu}_{1-\mu,+}(h) + \gamma_2 F^{-\nu,1+\nu}_{1-\mu,+}(h)\right] F^{-\nu,1+\nu}_{1+\mu,+}(z) \tag{D.37}$$

$$b_2 = \frac{\Gamma(\delta_+)}{\Gamma(\delta_-)}\frac{\delta_+}{2\mu}\left[F^{1-\nu,\nu}_{1+\mu,+}(h) - \frac{\gamma_2}{\delta_-}F^{-\nu,1+\nu}_{1+\mu,+}(h)\right]F^{-\nu,1+\nu}_{1-\mu,+}(z) \tag{D.38}$$

$$c_1 = \Gamma^2(\mu)\frac{\sin\delta_-\pi\sin\nu\pi}{2\pi\sin\mu\pi}\left[-\delta_+F^{1-\nu,\nu}_{1-\mu,-}(0) - \gamma_1F^{-\nu,1+\nu}_{1-\mu,-}(0)\right]F^{1+\delta_-,-\delta_+}_{1-\mu,-}(z) \tag{D.39}$$

$$c_2 = \Gamma^2(\mu)\frac{\sin\delta_-\pi\sin\nu\pi}{2\pi\sin\mu\pi}\left[\delta_+F^{\delta_-,1-\delta_+}_{1-\mu,-}(0) + \gamma_1F^{1+\delta_-,-\delta_+}_{1-\mu,-}(0)\right]F^{-\nu,1+\nu}_{1-\mu,-}(z) \tag{D.40}$$

$$c_3 = \frac{\Gamma(\delta_+)}{\Gamma(\delta_-)}\frac{\sin^2\nu\pi}{2\sin^2\mu\pi}\frac{\delta_+}{\mu\delta_-}\left[-\delta_+F^{\delta_-,1-\delta_+}_{1-\mu,-}(0) - \gamma_1F^{1+\delta_-,-\delta_+}_{1-\mu,-}(0)\right]F^{1+\delta_+,-\delta_-}_{1+\mu,-}(z) \tag{D.41}$$

$$c_4 = \frac{\Gamma(\delta_+)}{\Gamma(\delta_-)}\frac{\sin^2\nu\pi}{2\sin^2\mu\pi}\frac{\delta_+}{\mu}\left[F^{\delta_+,1-\delta_-}_{1+\mu,-}(0) + \frac{\gamma_1}{\delta_-}F^{1+\delta_+,-\delta_-}_{1+\mu,-}(0)\right]F^{1+\delta_-,-\delta_+}_{1-\mu,-}(z) \tag{D.42}$$

$$c_5 = \frac{\Gamma(\delta_+)}{\Gamma(\delta_-)}\frac{\sin\delta_-\pi\sin\delta_+\pi}{2\sin^2\mu\pi}\frac{\delta_+}{\mu\delta_-}\left[\delta_+F^{1-\nu,\nu}_{1-\mu,-}(0) + \gamma_1F^{-\nu,1+\nu}_{1-\mu,-}(0)\right]F^{-\nu,1+\nu}_{1+\mu,-}(z) \tag{D.43}$$

$$c_6 = \frac{\Gamma(\delta_+)}{\Gamma(\delta_-)}\frac{\sin\delta_-\pi\sin\delta_+\pi}{2\sin^2\mu\pi}\frac{\delta_+}{\mu}\left[-F^{1-\nu,\nu}_{1+\mu,-}(0) - \frac{\gamma_1}{\delta_-}F^{-\nu,1+\nu}_{1+\mu,-}(0)\right]F^{-\nu,1+\nu}_{1-\mu,-}(z) \tag{D.44}$$

$$c_7 = \frac{\Gamma^2(\delta_+)}{\Gamma^2(\delta_-)\Gamma^2(\mu)}\frac{\pi\sin\delta_+\pi\sin\nu\pi}{2\sin^3\mu\pi}\frac{\delta_+^2}{\mu^2\delta_-} \times\left[-F^{\delta_+,1-\delta_-}_{1+\mu,-}(0) - \frac{\gamma_1}{\delta_-}F^{1+\delta_+,-\delta_-}_{1+\mu,-}(0)\right]F^{-\nu,1+\nu}_{1+\mu,-}(z) \tag{D.45}$$

$$c_8 = \frac{\Gamma^2(\delta_+)}{\Gamma^2(\delta_-)\Gamma^2(\mu)}\frac{\pi\sin\delta_+\pi\sin\nu\pi}{2\sin^3\mu\pi}\frac{\delta_+^2}{\mu^2\delta_-} \times\left[F^{1-\nu,\nu}_{1+\mu,-}(0) + \frac{\gamma_1}{\delta_-}F^{-\nu,1+\nu}_{1+\mu,-}(0)\right]F^{1+\delta_+,-\delta_-}_{1+\mu,-}(z) \tag{D.46}$$

$$d_1 = \Gamma^2(\mu)\frac{\sin\delta_-\pi}{2\pi}\left[\delta_+ F^{1-\nu,\nu}_{1-\mu,+}(h) - \gamma_2 F^{-\nu,1+\nu}_{1-\mu,+}(h)\right] F^{-\nu,1+\nu}_{1-\mu,-}(z) \tag{D.47}$$

$$d_2 = \frac{\Gamma(\delta_+)}{\Gamma(\delta_-)}\frac{\sin\nu\pi}{2\sin\mu\pi}\frac{\delta_+}{\mu\delta_-}\left[-\delta_+ F^{1-\nu,\nu}_{1-\mu,+}(h) + \gamma_2 F^{-\nu,1+\nu}_{1-\mu,+}(h)\right] F^{1+\delta_+,-\delta_-}_{1+\mu,-}(z) \tag{D.48}$$

$$d_3 = \frac{\Gamma^2(\delta_+)}{\Gamma^2(\delta_-)\Gamma^2(\mu)}\frac{\pi\sin\delta_+\pi}{2\sin^2\mu\pi}\frac{\delta_+^2}{\mu^2\delta_-}\left[F^{1-\nu,\nu}_{1+\mu,+}(h) - \frac{\gamma_2}{\delta_-}F^{-\nu,1+\nu}_{1-\mu,+}(h)\right] F^{-\nu,1+\nu}_{1+\mu,-}(z) \tag{D.49}$$

$$d_4 = \frac{\Gamma(\delta_+)}{\Gamma(\delta_-)}\frac{\sin\nu\pi}{2\sin\mu\pi}\frac{\delta_+}{\mu}\left[-F^{1-\nu,\nu}_{1+\mu,+}(h) + \frac{\gamma_2}{\delta_-}F^{-\nu,1+\nu}_{1-\mu,+}(h)\right] F^{1+\delta_-,-\delta_+}_{1-\mu,-}(z) \tag{D.50}$$

$$\begin{aligned} m_1 = \Gamma^2(\mu)\frac{\sin\delta_-\pi}{2\pi}\delta_+\Bigg[&\frac{\Gamma(\delta_+)}{\Gamma(\delta_-)}\delta_+ F^{1-\nu,\nu}_{1-\mu,-}(0)\, F^{1-\nu,\nu}_{1-\mu,+}(h) - \gamma_2 F^{1-\nu,\nu}_{1-\mu,-}(0)\, F^{-\nu,1+\nu}_{1-\mu,+}(h) \\ &+\gamma_1 F^{-\nu,1+\nu}_{1-\mu,-}(0)\, F^{1-\nu,\nu}_{1-\mu,+}(h) + \frac{\Gamma(\delta_+)}{\Gamma(\delta_-)}\frac{\mu\gamma_1\gamma_2}{\delta_-}F^{-\nu,1+\nu}_{1-\mu,-}(0)\, F^{-\nu,1+\nu}_{1-\mu,+}(h)\Bigg] \end{aligned} \tag{D.51}$$

$$\begin{aligned} m_2 = \frac{\Gamma(\delta_+)}{\Gamma(\delta_-)}\frac{\sin\nu\pi}{2\sin\mu\pi}\frac{\delta_+}{\mu}\Bigg[&-\delta_+ F^{\delta_+,1-\delta_-}_{1+\mu,-}(0)\, F^{1-\nu,\nu}_{1-\mu,+}(h) + \gamma_2 F^{\delta_+,1-\delta_-}_{1+\mu,-}(0)\, F^{-\nu,1+\nu}_{1-\mu,+}(h) \\ &-\frac{\delta_+\gamma_1}{\delta_-}F^{1+\delta_+,-\delta_-}_{1+\mu,-}(0)\, F^{1-\nu,\nu}_{1-\mu,+}(h) + \frac{\gamma_1\gamma_2}{\delta_-}F^{1+\delta_+,-\delta_-}_{1+\mu,-}(0)\, F^{-\nu,1+\nu}_{1-\mu,+}(h)\Bigg] \end{aligned} \tag{D.52}$$

$$\begin{aligned} m_3 = \frac{\Gamma^2(\delta_+)}{\Gamma^2(\delta_-)\Gamma^2(\mu)}\frac{\pi\sin\delta_+\pi}{2\sin^2\mu\pi}\frac{\delta_+^2}{\mu^2}\Bigg[&F^{1-\nu,\nu}_{1+\mu,-}(0)\, F^{1-\nu,\nu}_{1+\mu,+}(h) + \frac{\gamma_1}{\delta_-}F^{-\nu,1+\nu}_{1+\mu,-}(0)\, F^{1-\nu,\nu}_{1+\mu,+}(h) \\ &-\frac{\gamma_2}{\delta_-}F^{1-\nu,\nu}_{1+\mu,-}(0)\, F^{-\nu,1+\nu}_{1+\mu,+}(h) - \frac{\gamma_1\gamma_2}{\delta_-^2}F^{-\nu,1+\nu}_{1+\mu,-}(0)\, F^{-\nu,1+\nu}_{1+\mu,+}(h)\Bigg] \end{aligned} \tag{D.53}$$

$$\begin{aligned} m_4 = \frac{\Gamma(\delta_+)}{\Gamma(\delta_-)}\frac{\sin\nu\pi}{2\sin\mu\pi}\frac{\delta_+}{\mu}\Bigg[&-\delta_+ F^{\delta_-,1-\delta_+}_{1-\mu,-}(0)F^{1-\nu,\nu}_{1+\mu,+}(h) - \gamma_1 F^{1+\delta_+,-\delta_+}_{1-\mu,-}(0)F^{1-\nu,\nu}_{1+\mu,+}(h) \\ &+\frac{\delta_+\gamma_2}{\delta_-}F^{\delta_-,1-\delta_+}_{1-\mu,-}(0)F^{-\nu,1+\nu}_{1+\mu,+}(h) + \frac{\gamma_1\gamma_2}{\delta_-}F^{1+\delta_-,-\delta_+}_{1-\mu,-}(0)F^{-\nu,1+\nu}_{1+\mu,+}(h)\Bigg] \end{aligned} \tag{D.54}$$

Bibliography

[1] R. J. Adrian. Particle-imaging techniques for experimental fluid-mechanics. *Ann. Rev. Fluid Mech.*, 23:261–304, 1991.

[2] D. A. Aguilar, B. R. Sutherland, and D. J. Muraki. Laboratory generation of internal waves from sinusoidal topography. *Deep Sea Res. II: Topical Studies in Oceanog.*, 53:96–115, 2006.

[3] M. H. et al. Alford. The formation and fate of internal waves in the south china sea. *Nature*, 521:65–69, 2015.

[4] M. R. Allshouse, F. M. Lee, P. J. Morrison, and H. L. Swinney. Internal wave pressure, velocity, and energy flux from density perturbations. *Phys. Rev. Fluids*, 1:014301, 2016.

[5] P. G. Baines. The generation of internal tides by flat-bump topography. *Deep Sea Res. Oceanog. Abstracts*, 20:179–205, 1973.

[6] P. G. Baines. The Generation of Internal Tides over Steep Continental Slopes. *Royal Soc. London Phil. Trans. Series A*, 277:27–58, 1974.

[7] N. J. Balmforth and T. Peacock. Tidal conversion by supercritical topography. *J. Phys. Oceanogr.*, 39:1965–1974, 2009.

[8] N. J. Balmforth, G. R. Ierley, and W. R. Young. Tidal conversion by subcritical topography. *J. Phys. Oceanogr.*, 32:2900–2914, 2002.

[9] T. H. Bell, Jr. Topographically generated internal waves in the open ocean. *J. Geophys. Res.*, 80:320–327, 1975.

[10] H. A. Clark and B. R. Sutherland. Generation, propagation, and breaking of an internal wave beam. *Phys. Fluids*, 22:076601, 2010.

[11] S. B. Dalziel. DigiFlow: Advanced image processing for fluid mechanics. http://www.damtp.cam.ac.uk/user/fdl/digiflow/index.htm, 2015.

[12] S. B. Dalziel, Hughes G. O., and B. R. Sutherland. Whole-field density measurements by 'synthetic schlieren'. *Exp. Fluids*, 28:322–335, 2000.

[13] A. Dettner, M. S. Paooletti, and H. L. Swinney. Internal tide and boundary current generation by tidal flow over topography. *Phys. Fluids*, 25: 116601, 2013.

[14] E. di Lorenzo, W. R. Young, and S. G. Llewellyn Smith. Numerical and Analytical Estimates of M2 Tidal Conversion at Steep Oceanic Ridges. *J. Phys. Oceanog.*, 36:1072–1084, 2006.

[15] P. Echeverri and T. Peacock. Internal tide generation by arbitrary two-dimensional topography. *J. Fluid Mech.*, 659:247–266, 2010.

[16] P. Echeverri, M. R. Flynn, K. B. Winters, and T. Peacock. Low-mode internal tide generation by topography: an experimental and numerical investigation. *J. Fluid Mech.*, 636:91–108, 2009.

[17] P. S. Epstein. Reflection of waves in an inhomogeneous absorbing medium. *Proc. Natl. Acad. Sci. U.S.A.*, 16:627637, 1930.

[18] S. B. Dalziel et al. Simultaneous synthetic schlieren and PIV measurements for internal solitary waves. *Measurement Science and Technology*, 18:533, 2007.

[19] A. Fincham and G. Delerce. Advanced optimization of correlation imaging velocimetry algorithms. *Exp. Fluids*, 29:13–22, 2000.

[20] Scott V. Franklin and Mark D. Shattuck, editors. *Handbook of Granular Materials*. CRC Press, New York, 2015.

[21] C. Garrett and E. Kunze. Internal Tide Generation in the Deep Ocean. *Ann. Rev. Fluid Mech.*, 39:57–87, 2007.

[22] B. Gayen and S. Sarkar. Turbulence during the generation of internal tide on a critical slope. *Phys. Rev. Lett.*, 104:218502, 2010.

[23] B. Gayen and S. Sarkar. Boundary mixing by density overturns in an internal tidal beam. *Geophys. Res. Lett.*, 38:L14608, 2011.

[24] B. Gayen and S. Sarkar. Direct and large-eddy simulations of internal tide generation at a near-critical slope. *J. Fluid Mech.*, 681:48–79, 2011.

[25] L. Gostiaux and T. Dauxois. Laboratory experiments on the generation of internal tidal beams over steep slopes. *Phys. Fluids*, 19:028102, 2007.

[26] S. D. Griffiths and R. H. J. Grimshaw. Internal Tide Generation at the Continental Shelf Modeled Using a Modal Decomposition: Two-Dimensional Results. *J. Phys. Oceanog.*, 37:428–451, 2007.

[27] Y. Guo and P. A. Davies. Laboratory modelling experiments on the flow generated by the tidal motion of a stratified ocean over a continental shelf. *Continental Shelf Res.*, 23:193–212, 2003.

[28] F. Ham and G. Iaccarino. Internal Waves in Laboratory Experiments. In *Annual Research Briefs*, pages 3–14. Stanford University, 2004.

[29] F. Ham, K. Mattsson, and G. Iaccarino. Accurate and stable finite volume operators for unstructured flow solvers. In *Annual Research Briefs (Center for Turbulence Research, Stanford, CA)*, pages 243–261. Stanford University, 2006.

[30] J. Hazewinkel, N. Grisouard, and S. B. Dalziel. Comparison of labratory and numerically observed scalar fields of an internal wave attractor. *Eur J Mech B-Fluid*, 30:51–56, 2011.

[31] D. F. Hill. General density gradients in general domains: The "Two-tank" method revisited. *Exp. Fluids*, 32:434–440, 2002.

[32] P. E. Holloway and Merrifield M. A. Internal tide generation by seamounts, ridges, and islands. *J. Geophys. Res.*, 104:25937–25952, 1999.

[33] X. Jia, X. Chen, Q. Li, and Q. Li. Study on Internal Waves Generated by Tidal Flow over Critical Topography. *J. Ocean Univ. China*, 13:728–732, 2014.

[34] S. Khatiwala. Generation of internal tides in an ocean of finite depth: analytical and numerical calculations. *Deep Sea Res. I: Oceanog. Res.*, 50:3–21, 2003.

[35] B. King, H. P. Zhang, and H. L. Swinney. Tidal flow over three-dimensional topography in a stratified fluid. *Phys. Fluids*, 21:116601, 2009.

[36] B. King, H. P. Zhang, and H. L. Swinney. Tidal flow over three-dimensional topography generates out-of-forcing-plane harmonics. *Geophys. Res. Lett.*, 37:L14606, 2010.

[37] B. King, M. Stone, H. P. Zhang, T. Gerkema, M. Marder, R. B. Scott, and H. L. Swinney. Buoyancy frequency profiles and internal semidiurnal tide turning depths in the oceans. *J. Geophys. Res. (Oceans)*, 117:C04008, 2012.

[38] Y. V. Kistovich and Y. D. Chashechkin. Linear theory of the propagation of internal wave beams in an arbitrarily stratifed liquid. *J. App. Mech. Tech. Phys.*, 39:729–737, 1998.

[39] K. G. Lamb. Nonlinear interaction among internal wave beams gener-

ated by tidal flow over supercritical topography. *Geophys. Res. Lett.*, 31: L09313, 2004.

[40] F. M. Lee, M. S. Paoletti, H. L. Swinney, and P. J. Morrison. Experimental determination of radiated internal wave power without pressure field data. *Phys. Fluids*, 26:046606, 2014.

[41] F. M. Lee, M. R. Allshouse, H. L. Swinney, and P. J. Morrison. Internal wave energy flux from density perturbations in nonlinear stratifications. *arXiv*, page 1711.06773, 2017.

[42] S. Legg. Internal Tides Generated on a Corrugated Continental Slope. Part I: Cross-Slope Barotropic Forcing. *J. Phys. Oceanog.*, 34:156–173, 2004.

[43] S. Legg. Internal Tides Generated on a Corrugated Continental Slope. Part II: Along-Slope Barotropic Forcing. *J. Phys. Oceanog.*, 34:1824–1838, 2004.

[44] J. Lekner. Reflectionless eigenstates of the sech^2 potential. *Am. J. Phys.*, 75:1151–1157, 2007.

[45] S. G. Llewellyn Smith and W. R. Young. Conversion of the Barotropic Tide. *J. Phys. Oceanog.*, 32:1554–1566, 2002.

[46] S. G. Llewellyn Smith and W. R. Young. Tidal conversion at a very steep ridge. *J. Fluid Mech.*, 495:175–191, 2003.

[47] K. Mahesh, G. Constantinescu, and P. Moin. A numerical method for large-eddy simulation in complex geometries. *J. Comput. Phys.*, 197:215–240, 2004.

[48] M. J. Mercier, D. Martinand, M. Mathur, L. Gostiaux, T. Peacock, and T. Dauxois. New wave generation. *J. Fluid Mech.*, 657:308–334, 2010.

[49] W. Munk and C. Wunsch. Abyssal recipes II: Energetics of tidal and wind mixing. *Deep Sea Res., Part I*, 45:1977–2010, 1998.

[50] J. R. Munroe and K. G. Lamb. Topographic amplitude dependence of internal wave generation by tidal forcing over idealized three-dimensional topography. *J. Geophys. Res. (Oceans)*, 110:C02001, 2005.

[51] J. D. Nash, M. H. Alford, and E. Kunze. Estimating Internal Wave Energy Fluxes in the Ocean. *J. Atmos. Oceanic Technol.*, 22:1551–1570, 2005.

[52] Y. Niwa and T. Hibiya. Three-dimensional numerical simulation of M_2 internal tides in the East China Sea. *J. Geophys. Res. [Oceans]*, 109: C04027, 2004.

[53] J. Nycander. Tidal generation of internal waves from a periodic array of steep ridges. *J. Fluid Mech.*, 567:415–432, 2006.

[54] M. S. Paoletti and H. L. Swinney. Propagating and evanescent internal waves in a deep ocean model. *J. Fluid Mech.*, 706:571–583, 2012.

[55] M. S. Paoletti, M. Drake, and H. L. Swinney. Internal tide generation in nonuniformly stratified deep oceans. *J. Geophys. Res. Oceans*, 119: 19431956, 2014.

[56] M. S. Paoletti, M. Drake, and H. L. Swinney. Internal tide generation in nonuniformly stratified deep oceans. *J. Geophys. Res*, 119:1943–1956, 2014.

[57] F. Petrelis, S. G. Llewllyn Smith, and W. R. Young. Tidal conversion at a submarine ridge. *J. Phys. Oceanogr.*, 36:1053–1071, 2006.

[58] G. Pöshl and E. Teller. Bemerkungen zur Quantenmechanik des anharmonischen Osziltators. *Z. Phys*, 83:143–151, 1933.

[59] H. Qian, P. T. Shaw, and D. S. Ko. Generation of internal waves by barotropic tidal flow over a steep ridge. *Deep Sea Res. I: Oceanog. Res.*, 57:1521–1531, 2010.

[60] N. R. Rapaka, B. Gayen, and S. Sarkar. Tidal conversion and turbulence at a model ridge: direct and large eddy simulations. *J. Fluid Mech.*, 715: 181–209, 2013.

[61] R. M. Robinson. The effects of a vertical barrier on internal waves. *Deep Sea Res. Oceanog. Abstracts*, 16:421–429, 1969.

[62] D. L. et al. Rudnick. From Tides to Mixing Along the Hawaiian Ridge. *Science*, 301:355–357, 2003.

[63] L. St Laurent, S. Stringer, C. Garrett, and D. Perraultjoncas. The generation of internal tides at abrupt topography. *Deep Sea Res. I: Oceanogr. Res.*, 50:987–1003, 2003.

[64] B. R. Sutherland. *Internal Gravity Waves*. Cambridge University Press, Cambridge, 2010.

[65] B. R. Sutherland, S. B. Dalziel, G. O. Hughes, and P. F. Linden. Visualization and measurement of internal waves by 'synthetic schlieren.' Part 1. Vertically oscillating cylinder. *J. Fluid Mech.*, 390:93–126, 1999.

[66] B. R. Sutherland, T. Dauxois, and T. Peacock. Internal Waves in Laboratory Experiments. In T. von Larcher and P. D. Williams, editors, *Modeling Atmospheric and Oceanic Flows: Insights from Laboratory Experiments*, pages 193–212. American Geophysical Union, 2014.

[67] C. Wunsch and R. Ferrari. Vertical mixing, energy and the general circulation of the oceans. *Annu. Rev. Fluid Mech*, 36:281–314, 2004.

[68] K.-Y. Yick, R. Stocker, and T. Peacock. Microscale synthetic schlieren. *Experiments in fluids*, 42:41–48, 2007.

[69] M. Zarroug, J. Nycander, and K. Döös. Energetics of tidally generated internal waves for nonuniform stratification. *Tellus Ser. A*, 62:71–79, 2010.

[70] H. P. Zhang, B. King, and H. L. Swinney. Experimental study of internal gravity waves generated by supercritical topography. *Phys. Fluids*, 19: 096602, 2007.

[71] H. P. Zhang, B. King, and H. L. Swinney. Resonant Generation of Internal Waves on a Model Continental Slope. *Phys. Rev. Lett.*, 100:244504, 2008.

[72] L Zhang and H. L. Swinney. Virtual Seafloor Reduces Internal Wave Generation by Tidal Flow. *Phys. Rev. Lett.*, 112:104502, 2014.

[73] N. V. Zilberman, J. M. Becker, M. A. Merrifield, and G. S. Carter. Model estimates of M2 internal tide generation over mid-atlantic ridge topography. *J. Phys. Oceanogr.*, 39:2635–2651, 2009.

Vita

Frank Moonyoung Lee was born in Chang-Won, South Korea on 4 October 1985, the son of Jong-Keun Lee and Sung-Huy Park. He received his Bachelor of Science degree in Physics and also in Mathematics at the University of Nebraska-Lincoln in 2010. In the same year, he was admitted to the physics Ph.D. program at the University of Texas at Austin.

Email address: sltfenix@utexas.edu

This dissertation was typeset with LaTeX[†] by the author.

[†]LaTeX is a document preparation system developed by Leslie Lamport as a special version of Donald Knuth's TeX Program.